

## ABSTRACT

Title of Dissertation:

WAVE CHAOS STUDIES FOR TWO-DIMENSIONAL CAVITIES USING THE RANDOM COUPLING MODEL (RCM) AND OTHER HIGH FREQUENCY METHODS

Farasatul Adnan  
Doctor of Philosophy, 2021

Dissertation directed by:

Professor Thomas Antonsen  
Department of Electrical and Computer  
Engineering

Wave coupling within systems with irregular boundaries is a common phenomenon in many branches of science such as acoustics, vibrations, electromagnetics, and others. If the wavelength of the incident wave is small compared with the structure size, and the dynamics of the ray trajectories within the scattering region are chaotic, the scattering properties of the cavity will be extremely sensitive to small perturbations. These structures are then termed *wave chaotic*. Exact solutions of such systems are not feasible and various alternative methods are sought.

In the first part of this dissertation, such alternative methods are used to calculate the power delivered to a port in a two-dimensional wave chaotic enclosure. These methods are the ray tracing (RT), the Dynamical Energy Analysis (DEA) and the Power Balance

methods (PWB). Particularly, the RT and DEA are used to calculate power received at an aperture and are compared with the established PWB. These results indicate that the RT and DEA are equivalent methods. Additionally, RT is compared with direct numerical simulations of the wave fields and found to be accurate if the wavelength is sufficiently small.

The Random Coupling Model (RCM) gives a statistical description of coupling of radiation in and out of large enclosures through localized and/or distributed ports. The RCM, in contrast to DEA, PWB, and standard RT, includes both amplitude and phase information. It combines both deterministic and statistical information and makes use of wave chaos theory to extend the classical modal description of the cavity fields in the presence of boundaries that lead to chaotic ray trajectories. In the second part of this dissertation, a correction to the RCM termed the Short Orbit Formulation (SOF) is used to calculate successfully the impedance of a two-port wave chaotic enclosure in two dimensions using RT. Also, a directed beam approach was used to launch energy in a wave chaotic enclosure to break the so called 'random plane wave hypothesis', a fundamental basis of the RCM formulations. Results show that launching of such directed beams lead to enhanced short orbit effects which make the RCM inapplicable.

**WAVE CHAOS STUDIES FOR TWO-DIMENSIONAL CAVITIES USING THE  
RANDOM COUPLING MODEL (RCM) AND OTHER HIGH FREQUENCY  
METHODS**

by

Farasatul Adnan

Dissertation submitted to the Faculty of the Graduate School of the  
University of Maryland, College Park, in partial fulfillment  
of the requirements for the degree of  
Doctor of Philosophy  
2021

**Advisory Committee:**

Professor Thomas Antonsen, Chair/Advisor  
Professor Edward Ott  
Professor Steven Anlage  
Professor Edo Waks  
Professor Neil Goldsman

© Copyright by  
Farasatul Adnan  
2021

## Dedication

To my mother Nazneen Sultana for making me who I am today. To my brother Arman Islam Sunny- I miss you every day. And to my wife Tarmim Monjur for supporting me during this PhD journey every step of the way.

## Acknowledgements

The work in this dissertation was funded by the AFOSR/AFRL under FA9550-15-1-0171, ONR under N000141512134 and ONR under N629091612115. I would like to thank both organizations for their generous support.

I would like to sincerely thank my advisor Professor Antonsen for his support, encouragement and guidance throughout my PhD program. I have learned an immense amount from him throughout this journey and could not have done this without his knowledge and foresight. I would also like to thank Professor Anlage and Professor Ott for providing constant feedback and useful suggestions throughout my PhD. I thank all my fellow graduate students not just at the Wave Chaos group but at the UMD as well-too many to mention. Thank you for your friendship and support.

Finally, I thank Professor Waks and Professor Goldsman for agreeing to serve on my dissertation defense committee.

# Table of Contents

Dedication	ii
Acknowledgements	iii
Table of Contents	iv
Chapter 1: Introduction .....	1
(A) Power delivery calculations in a chaotic cavity.....	2
(B) Calculate the impedance of a chaotic cavity using short orbit formalism .....	5
Chapter 2: Development of Ray Tracing, Cavity Impedance and Power Delivery Equations.....	9
(A) Motivation and general problem description .....	9
(B) The Ray Tracing Approach.....	11
(C) The Dynamical Energy Analysis: A Brief Overview.....	13
(D) The Power Balance Method (PWB): A Brief Summary.....	18
(E) The Random Coupling Model (RCM): A Brief Review.....	25
(F) The Short Orbit Formulation for Chaotic Cavities.....	29
Chapter 3: Results for Power Delivery Calculations.....	36
(A) Problem Setup.....	38
(B) Discussion of results for power delivery.....	40
(C) Results for power delivery using incident angle dependent reflection coefficient.....	46
Chapter 4: Results for cavity impedance calculations.....	55
(A) Problem Setup.....	59
Chapter 5: Breaking the RCM predictions with a directed beam.....	66
(A) Problem Setup.....	67
(B) Results.....	68
Chapter 6: Conclusions and future work.....	97
Conclusions.....	97
Future Work.....	99
Bibliography .....	102



# Chapter 1: Introduction

Electromagnetic (EM) coupling within systems of enclosures that are connected by apertures or ports is an important problem for the EM community that regularly appears in various forms. Examples include EM compatibility studies for electronic components under high-power microwave exposure [1, 2], wireless-signal propagation inside rooms or buildings [3] and even coupled quantum mechanical systems modeled with superconducting microwave billiards [4].

But for most irregular geometries, an analytical solution does not exist. In these cases, one can numerically solve the governing Maxwell's equations using methods such as the Finite Element Method (FEM) [5] or Finite Difference Time Domain (FDTD) [6] method. But, although these numerical approaches are powerful, they are difficult and time-consuming to implement in the case of high frequency applications due to the problem of large meshes or grids. In the small wavelength limit, where the ratio of the enclosure dimensions to the wavelength is large, the numerical solver must mesh the geometry covering it with a very large number of grid points. The amount of memory and computational power required to numerically solve these problems thus can become impractical. Furthermore, such deterministic solutions of these complicated geometries often depend sensitively on details of the system that may not be known. Even if it is known, the nature of the waves in the complex enclosures is such that small

change to the boundary conditions or the frequency dramatically changes the wave dynamics, thereby changing the solution substantially [7-9].

Consequently, researchers frequently resort to approximate solutions of the governing equations that are simpler to implement. The first part of the work presented in this thesis compares several of these lower order descriptions in sample problems and finds circumstances for which they agree and differ with respect to predictions. Specifically, we look at two methods which uses ray tracing (RT) but for different applications. One application is (A) RT used for power delivery calculations in a chaotic two cavity system and then compared with various other methods. Other is (B) the Short Orbit Formalism (SOF) which was used to calculate the impedance of a chaotic cavity. Then in continuation of the short orbit study we show (C) a directed beam study for a quasi 2D chaotic cavity. A brief description of these two applications of (A) and (B) is given here. A detailed description of these methods will follow in Chapter 2.

#### *(A) Power delivery calculations in a chaotic cavity*

For the power delivery calculations, the main complication that arises in the case of direct solution of high frequency excitation of a structure is the disparity in the size of the system and the wavelength of the excitation. As mentioned, this is what leads to the large density of mesh points or elements required for the modeling. Thus, the reduced models attempt to describe the distribution of energy throughout the system

without describing the details of the field distribution on the scale of a wavelength and without describing the associated phenomenon of interference. The three models that will be compared here are the Statistical Energy Analysis (SEA) [10], the Dynamical Energy Analysis (DEA) [11], and ray tracing (RT) [12].

The simplest of these models is the SEA, which is essentially a power balance method (PWB) [13-15]. In this method one solves for the energy (or energy density) in each subsystem. The energy is assumed to be uniformly distributed in each subsystem and its value is determined by balancing the input of energy from a source against coupling of energy out of the subsystem through ports or apertures, or through losses in the walls of the subsystem. In this model the description of the systems reduces to specifying effective quality factors for each process: wall losses or coupling through apertures. The solution of the problem then involves inverting a small matrix whose size is the number of cavities and whose elements contain the information about the various quality factors.

The second and third methods, RT and DEA, seek a more detailed level of description of the problem than does SEA. This level of description is the same in RT and DEA, but they differ in their numerical implementation. RT is a familiar approach in which the fields are represented as packets of energy that follow essentially classical trajectories through the system. The idea of wave energy travelling along rays is a well-established principle in wave propagation problems in many fields such as acoustics [16], seismology [17], wireless communication [18], plasma physics [19], and others.

For RT in enclosed regions, the trajectories reflect from walls, and refract if the medium is inhomogeneous. When a packet reflects from a wall, energy is deposited in the wall depending on the wall's material properties and the angle of incidence and polarization of the packet. The geometry of the system needs to be specified to implement RT; in particular, the location of the bounding walls must be specified. In cases where the supporting medium is inhomogeneous, its spatial variation must be prescribed as well. A numerical grid need not be constructed within each volume. However, a grid can be of use for tabulating local energy densities and for simplifying the calculation of trajectories. Since the field is being represented by a discrete set of packets, the solution invariably requires solving for a large number of trajectories to achieve a smooth distribution of energy density. In principle, phase information can also be included in the ray trajectories, and interference thus described. However, that was not pursued in this thesis.

The DEA can be thought of as an Eulerian description of the processes described by the Lagrangian approach of RT. In the DEA, the volume is gridded much as it would be in a full wave solution. However, since the wavelength is not being resolved the grid needed is much coarser than would be needed in the full wave case. The quantity that is solved for is essentially the phase space energy density flux on each surface (in 3D, line in 2D) separating cells. Thus, in 3D for monochromatic radiation one tabulates the power per unit area and per unit solid angle on the surface of each cell. This quantity is then propagated across the cell and re-tabulated on the facing surfaces. This process is repeated until a steady state is achieved.

What is shown in Chapter 3 of this thesis is that these three methods can produce, in some cases, equivalent results for the power delivery in a complicated multi-cavity system at high frequencies. But we also show there are some cases where the three are not equivalent. In this chapter for power delivery calculation first we discuss the problem geometry that we will use to compare the methods. After that we discuss the results obtained by the three methods and note some discrepancies. We also describe some results for the full wave solutions of the cavity using the commercial software HFSS [20] and compare it with RT results where the incident angles of rays were considered for the power delivery calculations.

*(B) Calculate the impedance of a chaotic cavity using short orbit formalism*

The other topic of work in this thesis in Chapter 4 is concerned with solving for the impedance of a chaotic bow-tie cavity. The method used for it is the Short Orbit Formalism (SOF) [21-22]. The SOF was introduced as a correction for the Random Coupling Model (RCM) [23-25] which is based on Random Matrix Theory (RMT) [26]. RMT predicts the statistical properties of a *single* wave chaotic system evaluated at different frequencies. This technique applies to a wide range of systems and has been studied theoretically and experimentally. It is shown in [21] that the average impedance matrix can be calculated directly using the classical ray trajectories of the system. However, there were modifications to the impedance calculations of the system due to the so-called ‘short orbits’. These orbits in turn can be used to calculate the impedance of the cavity. In Chapter 4, a more detailed description of short orbits is given. Also, it

is shown that the total summation of these short orbits can be used to calculate the impedance matrix of the system using rays to calculate said trajectories. A brief review of the previous work is shown here. A more mathematical description will be given in Chapter 2. In the same chapter a more detailed discussion of RCM will also be provided.

When we have a scenario of energy entering and leaving a cavity, we want to know how much power gets coupled into the system versus how much power is reflected back. Such information can be characterized by the Scattering Matrix,  $S$ . This matrix can also be expressed in terms of an Impedance Matrix  $Z$  such that

$$Z = Z_0^{1/2}(1 + S)(1 - S)^{-1}Z_0^{1/2} \quad (1.1)$$

where  $Z_0$  is an  $M \times M$  diagonal matrix, whose  $i$ th diagonal element is determined by the detailed properties of the  $i$ th scattering channel. One can use random matrix theory to model the scattering behavior of an ensemble of wave chaotic systems coupled to the outside world through  $M$  discrete scattering channels. Impedance is a meaningful concept for all scattering wave systems. In linear electromagnetic systems, it is defined via the phasor generalization of Ohm's law as

$$\hat{V} = Z\hat{I} \quad (1.2)$$

where the  $M$ -dimensional vector  $\hat{V}$  represents the voltage differences across the attached transmission lines (the systems port) and the  $M$ -dimensional vector  $\hat{I}$  denotes

the currents flowing through the transmission lines. What is shown in [21] is that we can define an 'average' impedance matrix  $Z_{avg}$  such that

$$Z_{avg} = Z_0^{1/2}(1 + S)(1 - S)^{-1}Z_0^{1/2} \quad (1.3)$$

Here  $Z_{avg}$  is the window average over a range of frequencies that is narrow enough to capture the time of flight of the short orbits. The window is smaller than  $1/T$  where T is the travel time between ports but is bigger than the spacing between adjacent modes. According to the SOF,  $Z_{avg}$  can be evaluated directly in the semiclassical limit as a sum over contributions from the prompt reflection and short classical trajectories. Furthermore

$$Z_{avg} = Z_{rad} + R_{rad}^{1/2} \zeta R_{rad}^{1/2} \quad (1.4)$$

where  $Z_{rad}$  is the radiation impedance matrix,  $R_{rad}$  is its real part and  $\zeta$  is an  $M \times M$  dimensionless matrix whose  $(m,n)$ th element describes the effects of wave propagation from port  $m$  to port  $n$ . A more explicit definition of  $\zeta$  is developed and discussed in Chapter 4.

In this dissertation work, these short trajectories were calculated by using a Ray Tracing (RT) code and shown that these assumptions are valid in the sense that ray optical trajectories can be used to calculate the impedance of the cavity. Short orbits were used in RT for a chaotic cavity to calculate  $\zeta$  and then these results were compared to full wave solutions using the commercial software HFSS.

In summary, this impedance calculation in Chapter 4 is organized as follows: first we discuss the problem geometry that we will use to solve for  $\zeta$ . After that we discuss the

results obtained by the SOF and note some discrepancies with HFSS. Finally, we draw the conclusions and talk about work that we can do in the future.

In the continuation of the study of short orbits in Chapter 4, a further investigation is carried out using a chaotic cavity with a circular scatterer in Chapter 5. A directed beam is used to launch EM energy into the cavity and shown that the directivity of the beam causes short orbits which leads to deviations from the RCM predictions.

The thesis is organized as follows: in Chapter 2 we discuss in detail the various methods used to study wave chaotic cavities namely the RT, the DEA, the PWB, the RCM and the SOF. In Chapter 3 we discuss the results obtained by using the RT, the DEA, the PWB and also include results for power calculations using incident angle dependent reflection coefficient. In chapter 4 we show results for a wave chaotic cavity using the SOF. In Chapter 5 we extend the short orbit study to a wave chaotic system where an electromagnetic beam was launched to break the ergodicity of the fields inside the cavity. In Chapter 6 we draw our conclusions and discuss future work.

## Chapter 2: Development of Ray Tracing, Cavity Impedance and Power Delivery Equations

### *(A) Motivation and general problem description*

In this thesis, the major interest is developing models that can describe the scattering and distribution of electromagnetic (EM) energy in complicated enclosures. We are interested in scattering of waves where, in the geometric optics approximation, the ray orbits within the structure are chaotic. These enclosures are labeled wave chaotic (or ray chaotic) cavities. Examples of such structures include optical, acoustic, microwave or electronic cavities.

For simplicity we concentrate on the case of a two-dimensional cavity. This situation is realized in a three-dimensional electromagnetic cavity enclosed by a conducting boundary when one of the dimensions is much smaller than the other two. In this case, the lowest frequency modes are polarized with the electric field directed in the short dimension and the magnetic has components in the other two dimensions. These modes have field components that are uniform in the short dimension and are thus separated in frequency from higher order modes whose components vary in the short dimension. The electric field component in the short dimension then satisfies a two-dimensional scalar wave equation with boundary conditions applied at the perimeter of the cavity. In the small wavelength limit the ray equations are same as those for the trajectory of a point particle: straight lines with specular reflection (i.e., angle of incidence equals angle of reflection) at the lateral boundaries. Such systems are called ‘billiards’ because

the trajectories of the rays are similar to those of the balls in the familiar parlor game [27].

Examples of chaotic billiards are shown in Fig. 2.1. The fundamental characteristic of such systems is that if we choose starting conditions for two trajectories that are the same speed but slightly different in location or angle, then the trajectories typically separate from each other, on average, exponentially with time due to the shape of the boundaries.

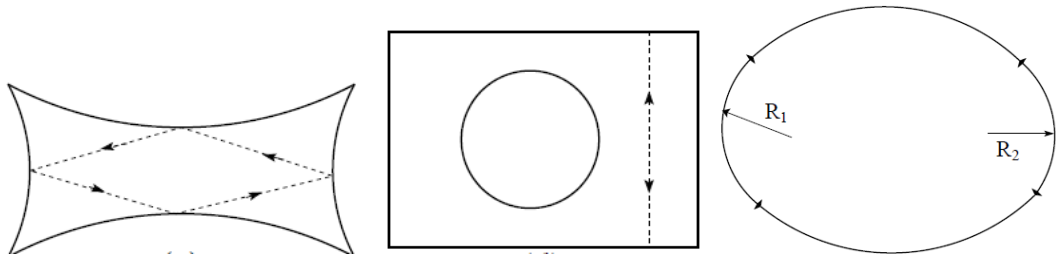


Fig. 2.1: Examples of billiard shapes. From the left: the bow-tie billiard, the Sinai billiard, the stadium billiard. Figure from [23].

Because of this property, these billiards show extreme sensitivity to initial conditions. Even a small perturbation in the initial condition will result in two nearby trajectories diverging exponentially.

A consequence of the extreme sensitivity of the trajectories in the ray approximation is that it can be very difficult to predict the EM (or wave) response of such a system exactly. This is referred to as “wave chaos”. As discussed in Chapter 1, numerically

solving these systems at high frequencies is computationally very demanding. Therefore, we discuss here alternative methods that can describe wave transport in geometries exhibiting wave chaos. These methods are ray tracing (RT), the Dynamical Energy Analysis (DEA), the Power Balance (PWB) and the Short Orbit Formulation (SOF). The first three are used for power delivery calculations: they do not include wave phase information. The third method (SOF) is an adjunct to the Random Coupling Model and is used to include information about direct paths between ports in the otherwise statistical RCM description. The RCM with the SOF corrections does include phase information that is omitted from the other three descriptions. We will present comparisons of the RT, DEA, PWB results for a Sinai billiard type system. The SOF will be used to calculate the impedance for a multi-port system for a quarter bowtie cavity.

### *(B) The Ray Tracing Approach*

The RT method is a popular method for describing wave systems where the wavelength is much smaller than the characteristic length of the scattering enclosure. In this high frequency regime, the 'ray approximation' is satisfied and rays can be followed as they bounce inside the enclosure [12]. For the two-dimensional geometries considered here Maxwell's equations reduce to a scalar Helmholtz wave equation. In the high frequency regime, it can be shown that wave energy follows trajectories similar to particle trajectories. For systems in which the wave speed is inhomogeneous in space, the trajectories bend due to refraction. However, in the systems considered here the

properties of the medium are homogeneous and the rays travel in straight lines except when they encounter a boundary and specularly reflect. In principle it is possible to retain wave phase information by computing the time of flight along a trajectory and accumulating the phase change that occurs with each reflection. This will be done when RT is used to compute the short orbit corrections to the RCM. However, phase information is not needed to track power delivery. In this thesis we use an RT algorithm to solve for the power delivery and for the short orbit formulation. We basically follow one of the approaches discussed in [28]. Specifically, we use the ‘Reflected and Transmitted Rays’ approach as discussed in ([28], Section III. B) and the power calculation is done using the ‘Shooting and Bouncing Ray (SBR) Method’ as discussed in ([28], Section IV. C).

For power delivery, at a port we launch rays in one of two ways. If the port is modeling an aperture in the side wall of the cavity we launch rays normal to the boundary and rays are uniformly distributed over the port. If the port is modeling an antenna consisting of a cylindrical conductor inserted through the top plate of the cavity and connected to coaxial transmission line, then rays are launched uniformly in all directions emanating from the port. In both cases each ray contains initially the same amount of power. The rays follow straight trajectories until they encounter a wall or scatterer at which point they are specularly reflected and their power is reduced according to  $P_{n+1} = |R|^2 P_n$ , where  $n$  refers to the bounce number,  $P_n$  is the power contained in the ray after the  $n$ -th bounce and  $R$  is the power reflectivity So, after each

bounce the ray loses ( $P_n - P_{n+1}$ ) amount of power. Further discussions and results are carried out in Chapter 3.

For the short orbit calculations, we follow the ray trajectories and calculate the distance traveled by the ray and the amount of spreading observed in adjacent rays as they pass by the receiving port. This is shown in more detail later in this chapter and results are shown in Chapter 4.

### *(C) The Dynamical Energy Analysis: A Brief Overview*

Recently, a mesh-based ray tracing solver called Dynamical Energy Analysis (DEA) [11] has been developed. It approximates wave energy transport using energy flow equations that compute power fluxes through the interfaces of a finite element mesh. In three dimensions the mesh elements are tetrahedra and the interfaces are triangles. In two dimensions the mesh elements are triangles and the interfaces are line segments. The quantity stored on an interface is the power density per unit area (length) and per unit solid angle (angle) for three (two) dimensional cases. These power densities are iterated by applying transfer operators that relate the power density of one interface of a mesh element to the power densities on the other interfaces shared by that element. The size of the DEA mesh is independent of frequency and allows for large variations in cell size. [29-32].

The DEA provides an efficient numerical approximation to wave energy transport that is, in principle, equivalent to RT. The advantages compared with standard ray-tracing are that the complexity of the environment (due to complex boundaries) is fully modelled as part of the mesh. Transport from one interface to another is simply described as the interfaces share a common mesh element. In contrast tracing rays over large distances can involve solving implicitly for bounce points on boundaries. The DEA also produces as a matter of course the spatial distribution of the wave energy density on the FE mesh. A disadvantage of DEA is that accurate time of flight information, which is easily retained in RT, is lost in DEA. It can be approximately recovered by counting the number of iterations of the transfer operator to reach a level of convergence. However, this has not been studied in detail. Finally, the introduction of a mesh introduces an artificial scattering of the wave energy as it propagates, and convergence of results with respect to grid size becomes limited if many grid cells are traversed.

DEA was initially introduced as a mesh-based high frequency method for modelling structure borne sound in complex built-up structures. In this method, vibro-acoustic simulations are performed directly on FE meshes. DEA provides detailed spatial information about the vibrational energy distribution within a complex structure in the mid-to-high frequency range. However, one can solve for any general wave system by solving a wave equation of the form

$$(\hat{H} + \omega^2)u(r) = -f(r) \quad (2.1)$$

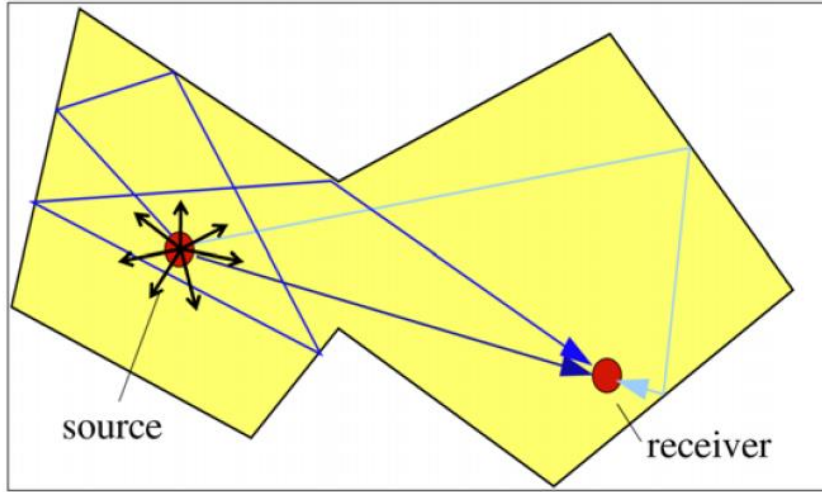
Here,  $\hat{H}$  corresponds to a linear operator describing the dynamics of the system (including dissipation), and  $f$  represents an excitation driving the system. In the DEA, the total system is defined on a domain  $\Omega$ , which is divided into a set of sub-domains  $\Omega_j, j = 1, \dots, N_\Omega$ , such as the elements of a mesh grid. Appropriate boundary conditions apply at the outer boundaries and at the interfaces between sub-domains. The wave energy density  $\varepsilon$  at a point  $r$  is then proportional to the square of the wave amplitude  $|u|$ , that is,

$$\varepsilon(r, \omega) \propto |u(r, \omega)|^2 \quad (2.2)$$

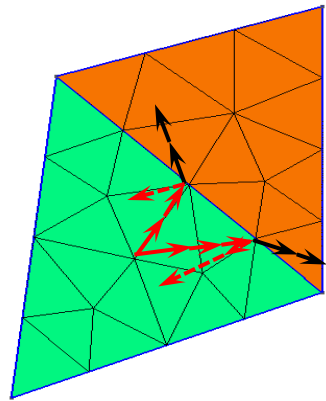
Now, (2.1) can be associated with the ray dynamics via the Eikonal approximation expressing the wave function  $u$  in terms of ray contributions [11] with associated amplitude  $A_j$  and phase  $\psi_j, j = 1, 2, \dots$ . This leads to a double sum over ray trajectories for the wave energy density of the form

$$\varepsilon(r, \omega) \propto \sum_{j, j'} A_j A_{j'} \cos \omega (\psi_j(r) - \psi_{j'}(r)) \quad (2.3)$$

In this summation, for  $j \neq j'$  it can be shown that taking the average over a frequency band centered on  $\omega_0$  the summation becomes negligibly small. For  $j = j'$  the summation terms can be written as  $\sum_j A_j(r, \omega)^2$ . Then the mean wave energy density is well approximated by the density of rays  $\rho(r, p, \omega_0)$  passing through a point  $r$ .



(a)



(b)

Fig. 2.1: (a) Ray tracing picture including reflection at boundaries. Figure from [32],  
(b) Schematic view of the energy flow in an FE grid for the DEA

Hence, we can write

$$\begin{aligned}\varepsilon(r, \omega) &\propto \sum_j A_j(r, \omega)^2 \\ &= \int \rho(r, p, \omega_0) dp\end{aligned}\quad (2.4)$$

where  $p$  is the direction (or momentum) vector. The system is excited by one or more point sources from which rays emerge uniformly and undergo reflections at boundaries as well as absorption processes, see Fig. 2.1. It is therefore possible to relate wave energy densities to classical flow equations and thus thermodynamical concepts, which is the essence of the DEA treatment.

DEA is based on the observation that these flow equations for ray densities can also be described using linear partial differential equations. In order to solve the stationary flow problem, these equations are written in boundary integral form; the boundary can be the physical boundary of the system and/or the union of interfaces between the sub-domains. Then sophisticated operators and algorithms are used to propagate this energy density across the grid (Fig 2.1(b)).

A more detailed description of the power flow calculation in DEA is shown in [33]. But it is important to note that the methodology sketched here for the DEA is formally equivalent to ray tracing.

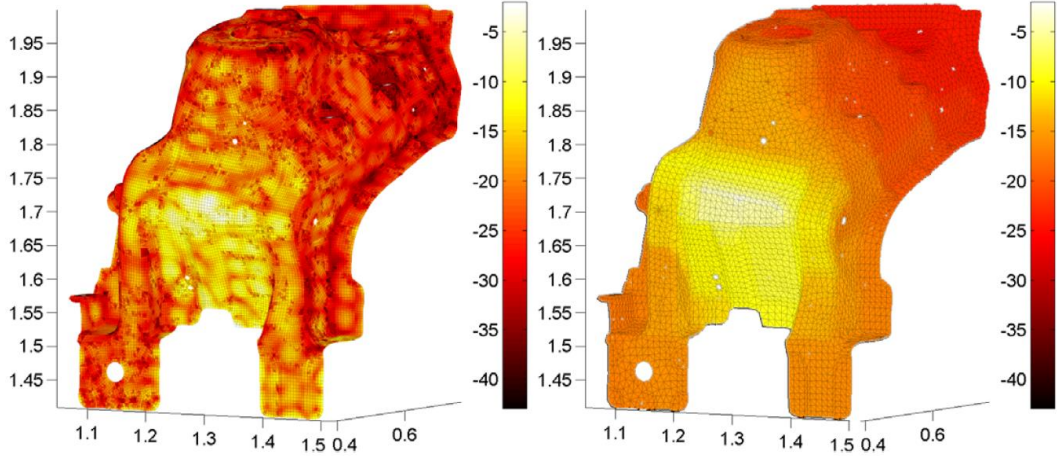


Fig. 2.2. Energy density on a thin aluminum shell (Range Rover shock tower) estimated using an averaged full wave finite element model (left) and a DEA model (right). Figure from [32].

Using an FE grid, the DEA has been successful in calculating energy densities for complicated geometries. One such geometry is shown in Fig 2.2. The right-hand side of Fig. 2.2 shows the response of a thin molded aluminum car component (shock tower of a Range Rover) to a point force applied perpendicular to the surface using DEA. The results are compared against a finite element simulation for the full wave model.

#### *(D) The Power Balance Method (PWB): A Brief Summary*

The power balance (PWB) model [13-15] predicts the averaged power flow in a system. This method yields predictions of the steady-state averaged energy density inside a system and it does so by equating the incoming and outgoing power in each connected subvolume. The PWB method can be used to determine mean values of EM power flow and energy in systems of coupled cavities. It characterizes the flow of high frequency

EM waves inside a complex interconnected system based on the physical dimensions of the cavities, the cavity quality factors  $Q$ , and the coupling cross sections  $\sigma$ , as well as the incident power  $P_{in}$  driving the system. A brief description of the PWB is given here.

For a chaotic cavity such as a reverberation chamber (RC), we can quantify the electric field by the total electromagnetic energy  $U$  (or energy density  $W = U/V$  where  $V$  is the volume of the cavity) of the reverberant field. The total EM energy can be written [34] as

$$U = \int_V \epsilon |E_T|^2 dV \quad (2.5)$$

Where the total magnitude of the electric field strength is  $E_T$  and  $\epsilon$  is the permittivity of the medium. For a statistically uniform electric field in a reverberation chamber, it has been shown [34] that the power balance principle applies as

$$P_{in} = P_{diss} = \omega \eta U = \omega U / Q \quad (2.6)$$

which simply states that the power input from an external source  $P_{in}$  must be balanced by the total power dissipated by all losses  $P_{diss}$ . Here,  $Q$  is cavity quality factor and  $\eta$  is the corresponding damping loss factor  $\eta = 1/Q$ . For multiple connected reverberant subsystems, one can calculate a power balance equation for each that will include

energy transmitted to connected systems. An example of such a system is shown in Fig. 2.3.

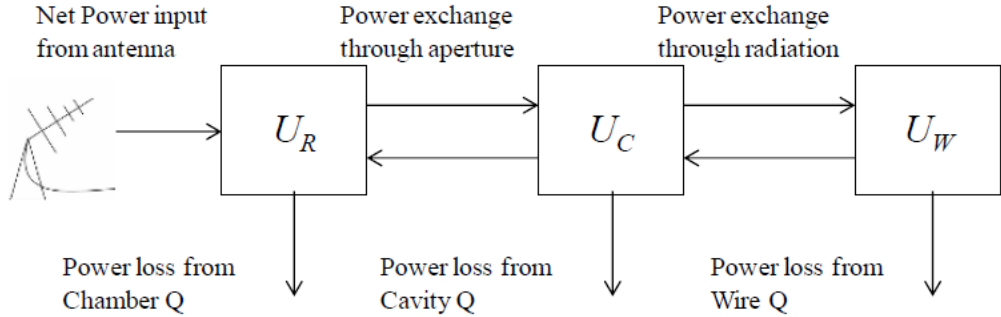


Fig 2.3: Power balance schematic for a multiple connected cavity.  $U_R$ ,  $U_C$ ,  $U_W$  refer to the energy  $U$  in respective enclosures. Figure from [35]

In this example, a geometry was considered for the exchange of energy through apertures and through radiation. Input was shown from an antenna. But one can consider any incoming wave from an external source which couples into the leftmost enclosure. In this thesis, energy exchange between subsystems via aperture is considered similar to this example.

[34], It has been shown that the net power flow  $\langle P_{ij} \rangle$  between any two reverberant energy subsystems ( $i, j$ ) – averaged over an ensemble of uncertain parameters - is proportional to the difference in their modal energy levels as

$$\langle P_{ij} \rangle = \omega n_i \eta_{ij} \left\{ \left\langle \frac{U_i}{\eta_i} \right\rangle - \left\langle \frac{U_j}{\eta_j} \right\rangle \right\} \quad (2.7)$$

where  $n_i$  is the modal density and  $\eta_{ij}$  is a coupling loss factor. Writing the power balance equations for each of the three subsystems in Fig. 2.3 yields a power balance matrix which can be solved for the average reverberant energy levels  $\langle U_R \rangle$ ,  $\langle U_C \rangle$ ,  $\langle U_W \rangle$  as

$$\begin{Bmatrix} P_R^{in} \\ 0 \\ 0 \end{Bmatrix} = \omega \begin{bmatrix} \eta_R + \eta_{RC} & -\eta_{CR} & 0 \\ -\eta_{RC} & \eta_C + \eta_{CR} + \eta_{CW} & -\eta_{CW} \\ 0 & -\eta_{CW} & \eta_W + \eta_{WC} \end{bmatrix} \begin{Bmatrix} U_R \\ U_C \\ U_W \end{Bmatrix} \quad (2.8)$$

To calculate the energy flow predicted by PWB in this thesis, we define the quantities used to implement the PWB. The type of geometry we consider is shown in Fig. 2.4. It is discussed in more detail in Chapter 3. Here we include it for our illustrations for the PWB formulation. In this picture we see a 2D cavity with scatterers. The black bars labeled  $P_{1,2}$  are aperture like ports where external energy may enter the system. Energy then can bounce around, incur losses and leave through either  $P_1$  or  $P_2$ . Therefore, it is a similar system to the one described above. The cavities on the left and right are cavities 1 and 2 respectively.

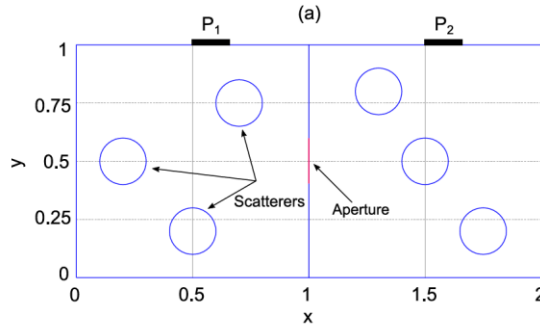


Fig. 2.4: A schematic showing a multi cavity system connected by an aperture.

Here, the widths of Ports 1 and 2, which connect the cavities to the exterior, and of the aperture that couples the two cavities are respectively denoted ( $w_1$ ,  $w_2$ ,  $w_A$ ). The perimeters of Cavities 1 and 2, including the scatterers, are denoted ( $l_1$ ,  $l_2$ ). Then

$$\sigma_i^{wall} = \alpha(l_i - (w_i + w_A)) \quad (2.9)$$

where  $i=1, 2$  labels the cavities, defines an effective absorption cross sections of cavity  $i$ , which captures the power absorbed by the wall and scatterer boundaries. The quantity  $\alpha$  is the local fraction of incident power absorbed by the boundary. In our 2D system, the absorption cross section in (2.9) represents an effective physical length. The power absorbed is proportional to the product of this length and the energy per unit area in the cavity under consideration. The constant of proportionality scales with the wave speed. In addition, the power lost by escaping through the cavity walls is proportional to the fraction of power incident  $\alpha$ , which in practice is determined by the electrical characteristics of the wall material. Here, we have not focused on specific/prescribed wall materials. We rather perform a study by varying  $\alpha$  across the full range, from 0 (the incident power is entirely reflected) to 1 (the incident power is entirely absorbed).

The total loss for each cavity, including radiation through apertures and ports, is then

$$\sigma_i^{tot} = \sigma_i^{wall} + w_i + w_A \quad (2.10)$$

$\sigma_i^{tot}$  here refers to the total length through which the power escapes the cavity. Let  $P_i^{tot}$  represent total power entering cavity  $i$ , which includes both the power  $P_i^{inj}$  directly injected into the cavity and the power  $P_{ij}^{back}$  passing through the aperture from the other cavity, labelled  $j$ . In detailed calculations to follow, we assume injection of power only into cavity 1, so  $P_2^{inj} = 0$ . We also denote by  $P_i^{port}$  the power leaving through Port  $i$  and by  $P_i^{wall}$  the power absorbed by the walls of Cavity  $i$  (including those of the scatterers).

Under power balance assumptions, the total power and the powers leaving Cavity  $i$  through Port  $i$ , through the aperture to the other cavity, and being absorbed by its walls are related by

$$\frac{P_i^{tot}}{\sigma_i^{tot}} = \frac{P_i^{port}}{w_i} = \frac{P_{ji}^{back}}{w_A} = \frac{P_i^{wall}}{\sigma_i^{wall}} \quad (2.11)$$

where  $j=1$  if  $i=2$  and  $j=2$  if  $i=1$ . The weighted powers in these equalities provide a coarse grained analogue of the flux density  $\rho$  that is central to DEA. They are equal if  $\rho$  is a constant, which amounts to an assumption of ergodicity and low loss. If  $\rho$  deviates strongly from uniformity, the power balance assumptions fail.

In the special case  $P_2^{inj} = 0$ , we can show from these balance conditions that the total power entering cavity 1 is

$$P_1^{tot} = \frac{P_1^{inj}}{1 - w_A^2 / (\sigma_1^{tot} \sigma_2^{tot})} \quad (2.12)$$

We can then also easily find the fractions of power lost by each of the mechanisms of wall loss or radiation through ports and apertures. For example, in the absence of wall loss ( $\alpha = 0$ ) the fraction of injected power leaving cavity 1 through Port 1 is

$$\frac{P_1^{port}}{P_1^{inj}} = \frac{w_1(w_2 + w_A)}{w_1 w_2 + w_A(w_1 + w_2)} \quad (2.13)$$

For the quoted parameters, we find  $P_1^{port}/P_1^{inj} = 0.641$ . On the other hand, with maximum wall loss ( $\alpha = 1$ ), we find

$$\frac{P_1^{port}}{P_1^{inj}} = \frac{w_1/\sigma_1^{tot}}{1 - w_A^2 / (\sigma_1^{tot} \sigma_2^{tot})} \quad (2.14)$$

For the quoted parameters,  $\sigma_1^{tot} = 5.995$ , and thus  $P_1^{port}/P_1^{inj} = 0.0267$ . Note that in the high loss case the fraction of power leaving through Port 1 is a finite number.

In summary of the PWB, for a multi cavity system, the PWB method solves for the mean power density in each enclosure by balancing the powers entering and leaving each cavity. These power transfer rates are characterized in terms of area cross sections  $\sigma$ . Various losses, such as aperture-port leakage, cavity wall absorption, and lossy

objects inside the enclosure are characterized through the corresponding cross sections. Constant power is injected into the coupled systems through sources in some or all of the enclosures. PWB finds a steady-state solution when the inputs and losses are made equal for each individual cavity in the system reaching a power balanced state.

#### *(E) The Random Coupling Model (RCM): A Brief Review*

The RCM is rooted in the original work done by Eugene P. Wigner [36]. Wigner was interested in the statistics of the energy levels of large nuclei. He posited that the probability distribution of the spacing between energy levels is the same as the spacing between the eigenvalues of a random matrix with particular properties. Two of the random matrices Wigner discusses are important for the RCM, the Gaussian Orthogonal Ensemble (GOE) and the Gaussian Unitary Ensemble (GUE). The elements for both types of matrices are independent Gaussian random variables with zero mean. But the GOE and GUE are applicable to different systems. The GOE is used to model wave systems that have time reversal symmetry (TRS). As a simple example of the GOE type of systems, one can consider a charged particle in a scalar potential. By reversing the direction of the momentum of the particle, the classical particle will retrace its own path. The corresponding GOE of this system consists of real random symmetric matrices.

On the other hand, if a magnetic field is applied, the time reversal symmetry is broken. A classical charged particle will no longer retrace its own path when the direction of

its momentum is reversed. The GUE case is used for modelling such systems for which time reversal symmetry is broken (TRSB). The GUE matrices are Hermitian. In this case, the off-diagonal elements are complex. The distributions of their real and imaginary parts are independent and Gaussian. The width of these Gaussians is one half the width of the real diagonal elements. This GUE case can also apply in electromagnetics if a nonreciprocal element such as a magnetized ferrite or a cold magnetized plasma is added to the system.

In this thesis, eigenvalues of a random matrix of the Gaussian Orthogonal Ensemble (GOE) with Gaussian distributed elements have been used since the time-reversal invariance is assumed.

The elements of the GOE matrices are real with different variances for the diagonal and off-diagonal elements. The main property of GOE matrices is invariance under orthogonal transformation. That is, the probability distribution of an ensemble of matrices has the property that  $P(H) = P(OHO^T)$  where  $O$  is an arbitrary orthogonal matrix and the  $O^T$  is its transpose. On the other hand, the GUE matrices have elements of complex numbers, and the matrices are invariant under unitary transformation such that  $P(H) = P(UHU^\dagger)$  where  $U$  is arbitrary unitary matrix and  $U^\dagger$  is its conjugate transpose.

A key finding in Wigner's work is the spacing between nearest neighbor frequencies of resonant modes (or energies in the case of nuclei). The distribution of the spacing has

universal properties that we exploit to statistically characterize our systems. In the case of electromagnetic enclosures, we focus on spacing between the resonant wavenumbers squared,  $k_n^2$ , where  $\omega_n = k_n c$  is the resonant frequency. The mean mode spacing ( $\Delta k^2 = \langle k_{n+1}^2 - k_n^2 \rangle$ ) can be approximated by Weyl's formula. For 3D electromagnetic enclosures, it is given by  $\Delta k^2 = 2\pi^2/kV$ , where  $k = \omega/c$  and  $V$  is the volume of the enclosure [37]. Thus, we consider the distribution of

$$s = \frac{k_{n+1}^2 - k_n^2}{\Delta k^2} \quad (2.15)$$

In the case where the system has time reversal symmetry, the probability distribution of  $s$  takes the form [38]

$$P_{GOE}(s) \cong \frac{\pi}{2} e^{-\pi s^2/4} \quad (2.16)$$

If time reversal symmetry is broken, for example if a magnetized ferrite is present, the probability distribution has the form

$$P_{GUE}(s) \cong \frac{32}{\pi} s^2 e^{-4s^2/\pi} \quad (2.17)$$

The probability distributions apply to the eigenvalues of matrices that are from the Gaussian Orthogonal Ensemble (GOE) or Gaussian Unitary Ensemble (GUE). These have been shown to be applicable in enclosures that are "ray chaotic". That is, in the limit where the incident wave propagates like a point particle, the ray trajectories are chaotic.

The eigenfunctions of GOE and GUE also have universal properties. In the GOE case the components of the eigenfunctions are real Gaussian random variables which are, for large matrices, independent with zero mean and common variance. In the GUE

case the eigenfunction components are complex Gaussian random variables with independent real and imaginary parts, zero means, and common variances.

The RCM is a statistical model used to characterize the impedance matrix of a multi-port, complex, overmoded electromagnetic cavity [23-25]. It is based on a combination of the random plane wave approximation, in which the fields at any point in the enclosure consist of the random superposition of isotropically propagating plane waves with random phases, and the random matrix theory which provides the statistical distributions. The main result from the RCM is that the random impedance,  $Z$ , at a single port in a wave chaotic cavity is given in terms of system specific deterministic quantities and a universally distributed random quantity expressed in the following formula

$$Z = jX_{rad} + \xi R_{rad} \quad (2.18)$$

where  $R_{rad}$  and  $X_{rad}$  are the real and imaginary part of the radiation impedance  $Z_{rad}$ , which is the impedance of the port excluding contributions from the cavity. In other words, it is the impedance that would be measured if the cavity walls were moved out to infinity. The quantity  $\xi$  is a complex random variable whose probability distribution is fully characterized by a single loss parameter  $\alpha$ . It is defined as

$$\xi = -\frac{j}{\pi} \sum_n \frac{\Delta k^2 \phi_n \phi_n^T}{k^2 - k_n^2 + j\alpha \Delta k^2} \quad (2.19)$$

where  $\phi_n$  is a vector of independent and identically distributed, zero mean, unit variance Gaussian random variables.  $k_n^2$  is also a random vector of the eigenmodes of the system whose normalized distribution is described by random matrix theory.  $\alpha$  is

the loss parameter.  $\Delta k^2 = \langle k_{n+1}^2 - k_n^2 \rangle$  is the mean mode spacing. According to Weyl's formula [39] for a two-dimensional cavity of area  $A$ , the mean spacing between two adjacent eigenvalues is given by  $\Delta k^2 = 4\pi/A$ .

A method to generate an ensemble of  $k_n^2$  is described in Appendix of Ref. [40]. The loss parameter  $\alpha$  characterizes the loss in the enclosure. The loss parameter is essentially the average  $Q$ -width of resonant modes in the cavity normalized to the average spacing between modes. This result can be extended to a multi-port cavity as

$$Z = jX_{rad} + R_{rad}^{1/2}\xi R_{rad}^{1/2} \quad (2.20)$$

where all the variables are now matrices. Therefore, the  $Z_{rad}$  and  $\alpha$  are the two system specific parameters necessary to apply the RCM which allows us to predict the statistics of the impedance of a chaotic cavity. Furthermore, the loss parameter  $\alpha$  can be calculated as  $\alpha = k^2/(Q\Delta k_n^2)$ , where  $k$  is the wave vector of interest and  $Q$  is the quality factor.

#### *(F) The Short Orbit Formulation for Chaotic Cavities*

Although the RCM was found to be an accurate description if an ensemble of cavities was sampled, or a large range of frequency was sampled for a single cavity, it was

found to have deviations from computed solutions if a single cavity or a narrow range of frequencies were sampled. Deviation was traced to the influence of paths between ports that were only weakly defocusing, or short orbits. As shown by Hart et al.[21], the statistical characterization of the cavity impedance is possible by including ray trajectories that are these so called 'short orbits'. These are trajectories travel from one port to another in a short time  $T$ . They induce correlations in the frequency dependence over a range of frequencies  $T^1$ . In [21] a detailed derivation of the 'Short Orbit Formulation' (SOF) is given. Here only a summary of the theory leading to the SOF is given. A more detailed discussion of short orbits is given in Chapter 4.

For the development of SOF, we consider a quasi 2D bowtie cavity (Fig. 2.5). It is a simulated EM cavity filled with a uniform lossless dielectric and is coupled to the outside world through coaxial cables (the ports) inserted into holes on the top of the cavity. The cavity has a uniform height  $h$  in the  $z$  direction, which is much smaller than the wavelength of the incident microwaves. So, Maxwell's equations become effectively two dimensional with the electric and magnetic fields uniform in the  $z$  direction.

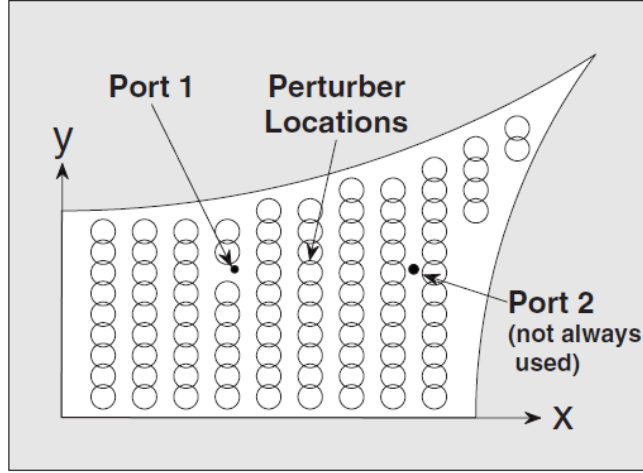


Fig. 2.5: A schematic of the 2D quarter-bowtie cavity. Figure from [21]

For the electromagnetic system described, it was previously derived [23] the following inhomogeneous wave equation for the case where the ports are modeled by vertical  $z$  direction, externally imposed, and localized current densities flowing from the bottom to the top plates

$$(\nabla^2 + k^2) \hat{V}_T(\vec{r}) = ikh\eta \sum_{p=1}^M u_p(\vec{r}) I_p \quad (2.21)$$

where  $\nabla^2$  is the 2D Laplacian in the  $(x, y)$  plane,  $\hat{V}_T$  represents the voltage difference between the two plates,  $I_p$  represents the total current injected into the cavity through port  $p$ ,  $u_p(\vec{r})$  represents the profile of the current injected onto the top plate at port  $p$  and has the property  $\int u_p(\vec{r}') d\vec{r}' = 1$ ,  $\eta = \sqrt{\mu/\epsilon}$  is the wave impedance of propagation within the medium inside the cavity and  $k = 2\pi/\lambda$  is the wave number of the external driving frequency.

In order to solve this equation, we can turn it into an integral equation by introducing the outgoing Green's function  $G_0$  which satisfies

$$(\nabla^2 + k^2)G_0(\vec{r}, \vec{r}', k) = \delta(\vec{r} - \vec{r}') \quad (2.22)$$

Then by following various steps outlined in [21], we can find the impedance between ports  $m$  and  $n$  as

$$Z_{n,m} = ikh\eta \int d^2\vec{r} u_n(\vec{r}) (\mathbf{V}_-(1 - \mathbf{K})^{-1} \mathbf{V}_+ + G_0) u_m(\vec{r}) \quad (2.23)$$

where  $G_0$  is the two-dimensional outgoing Green's function in empty space (as before); it finds the voltage at some position  $\vec{r}$  caused by a delta-function current distribution at point  $\vec{r}'$ . The operator  $\mathbf{V}_+$  finds the current induced in the wall by a delta-function current in the volume. The operator  $\mathbf{K}$  represents the current induced in one part of the wall by the current in another part of the wall. The operator  $\mathbf{V}_-$  on the other hand, gives the voltage inside the volume, which results from the currents in the walls.

The second term in the integral on the right-hand side of (2.23) represents the impedance the system would have if the walls were moved to infinity and outgoing boundary conditions were imposed but impedance due to direct orbits between the ports were still included. Therefore, we define an  $M \times M$  matrix  $\tilde{\mathbf{Z}}_R$ , which has the elements

$$\tilde{Z}_{R,n.m} = ikh\eta \int d^2\vec{r} u_n(\vec{r}) G_0 u_m(\vec{r}) \quad (2.24)$$

The diagonal elements of  $\tilde{\mathbf{Z}}_R$  are equal to the diagonal elements of the radiation impedance  $Z_{rad}$  and the off-diagonal elements represent contributions to the impedance from direct orbits between the ports.

Now (2.24) is an exact solution to (2.21) explicitly in terms of the boundaries. Analytically, it is intractable. But an approximation can be made via the SOF. It was shown in [21] that one can calculate the off-diagonal terms of (2.24) as

$$Z_{R,n,m} = \sqrt{R_{R,n} R_{R,m}} C_{(0,n,m)} e^{iS_{(0,m,n)} - i\pi/4}, \quad n \neq m \quad (2.25)$$

where  $C_{0,m,n}$  and  $S_{0,m,n}$  are the corresponding prefactor and action for a direct orbit from port  $m$  to port  $n$ .  $R_R$  is the real part of the radiation impedance  $Z_{rad}$ . This equation is what is referred to as the SOF.

Now according to the RCM, the cavity impedance takes the form

$$\tilde{Z}_{ab}(\omega) = i\bar{X}_{ab}(\omega) + i(\bar{R}^{1/2} \xi \bar{R}^{1/2})_{ab} \quad (2.26)$$

where  $\bar{Z}_{ab}$  is as described below

$$\bar{Z}_{ab}(\omega) = \bar{\bar{Z}}_{ab}(\omega) + i(\bar{\bar{R}}^{1/2} \zeta \bar{\bar{R}}^{1/2})_{ab} = i\bar{X}_{ab} + \bar{R}_{ab} \quad (2.27)$$

$\bar{Z}_{ab}$  is the average impedance matrix  $Z_{avg}$ ,  $\zeta$  is the universal fluctuating RMT matrix,  $\bar{\bar{Z}}_{ab}$  is the radiation impedance matrix  $Z_{rad}$  and we assume the ray travels from point  $a$  to point  $b$ .

$$\zeta_{ab} = \sum_{\substack{\text{orbits} \\ a \rightarrow b}} C_{ab} \exp[i\omega T_{ab} + i\phi_{ab}] \quad (2.28)$$

describes the effects of the short orbits.  $C_{ab}$  accounts for the defocusing and spreading of rays along the path from  $a$  to  $b$ .  $\phi_{ab}$  is a phase that accounts for the number of reflections from conductors and the number of caustics grazed.

This term  $\zeta$  can be used to write the average impedance as

$$\bar{Z}_{ab}(\omega) = \bar{\bar{Z}}_{ab}(\omega) + i(\bar{\bar{R}}^{1/2}\zeta\bar{\bar{R}}^{1/2})_{ab} \quad (2.29)$$

and one can also write the impedance between port 1 and 2 in terms of  $\zeta$  as

$$Z_{12} = \zeta_{12}(R_{rad1}R_{rad2}G_1G_2)^{1/2} \quad (2.30)$$

where  $R_{rad}$  is the radiation resistance of the two ports and  $G_1$  and  $G_2$  refer to the gain of the port (antenna). For our case, we have a point source radiating in all directions equally and so the gain is unity.

A similar formulation for the  $Z_{12}$  has been developed in [21] in terms of  $\zeta$ . For this work, we write

$$\zeta_{12} = \sum \left( \frac{2j\Delta\theta}{\pi k_0 \Delta} \right)^{1/2} (-1)^m e^{-jr_{12}k_0} \quad (2.31)$$

Here  $\Delta\theta$  is the initial separation angle between rays as they are launched (from port 1 the source), and  $\Delta$  is the separation distance between rays straddling the target point (which is port 2 the receiver) originating from a given short orbit (Fig 2.6),  $k_0$  is the wavenumber for free space,  $r_{12}$  is the distance the ray travels from port 1 to 2.



Fig. 2.6: On the left we see two rays launched from a point with separation  $\Delta\theta$ . The other picture shows the distance  $\Delta$  between the two same rays as they are passing the target

For further clarification, the first term under the square root in the equation for  $\zeta$  is the prefactor term,  $m$  refers to the bounce number. So, the term  $(-1)^m$  accounts for the

phase change of the ray every time it encounters a bounce. Therefore, if we can calculate the distance  $r_{12}$  and the  $\Delta$  for each bounce, we can calculate the  $\zeta$  and consequently the  $Z_{avg}$  of the cavity.

In summary of this chapter, we have discussed the various tools needed to analyze chaotic cavities of our interest. Short descriptions of the DEA, RT, PWB and the SOF was provided. In the next chapter we show numerical results where DEA, RT and PWB were applied to a two dimensional chaotic cavity to calculate the power delivered to a port.

## Chapter 3: Results for Power Delivery Calculations

In this chapter we calculate power delivery at a port in a chaotic cavity using three different approximation methods. The three methods are the Power Balance Method (PWB), Ray Tracing (RT) and Dynamical Energy Analysis (DEA).

Wave energy distributions in complex systems are often modelled well by using a thermodynamical approach. For such methods, it is often suggested to partition the full system into subsystems and to assume that each subsystem is internally in ‘thermal’ equilibrium. Interactions between directly coupled subsystems can then be described in terms of coupling constants. These constants can be determined by the properties of the wave dynamics at the interfaces between subsystems. These ideas form the basis of *Statistical Energy Analysis* (SEA) [10]. For applications in electromagnetism, this approach is known as *PoWer Balance method* (PWB) [13-15,34].

This method computes the mean power flow between adjacent subsystems assuming (just as in SEA) that the power is proportional to the difference in the energy density of the two subsystems. This constant of proportionality (also referred to as the coupling loss factor) depends on the details of the coupling such as the size of the aperture. The energy density in each subsystem is assumed to be constant. This leads to a simple linear system of equations with dimension equal to the number of subsystems.

A method similar in spirit but very different in applications is the so-called *Ray Tracing technique* (RT). The wave intensity distribution at a specific point  $r$  is determined here by summing over contributions from all ray paths starting at a source point  $r_0$  and reaching the receiver point  $r$ . It thus considers the full flow of ray trajectories. The RT is based on ray optics which solve the Maxwell's equations in high frequency regime [12]. Thus, the RT method is a general propagation modeling tool that can provide estimates of path loss, angle of arrival/departure, and time delays. It is a computer program and is a numerical method solving Maxwell's equations. RT algorithms, which keep information about the lengths of individual rays, can predict interference effects and thus recreate the fluctuations in a typical wave signal unlike PWB methods.

Dynamical energy analysis (DEA) can be interpreted as an Eulerian description of RT. In DEA, the volume is gridded much as it would be for methods to obtain a full-wave solution. However, since resolution on wavelength scales is not required in a ray-tracing simulation, the mesh can be much coarser than would be necessary for solving the underlying wave problem. The quantity of interest in DEA is an energy density, computed as a phase-space flux on the faces of a mesh cell. For example, in a three-dimensional (3D) problem and for monochromatic radiation, one records the power per unit area and per unit solid angle on the mesh boundary of each cell. This quantity is then propagated across the cell and re-tabulated on the facing surfaces. This process is iterated until a steady state is achieved. The method has been introduced first in 2009 [11] and has been refined over the years, mainly for applications in vibro-acoustics. It is now able to run on grids of several million elements in 2D [29-30] and has been

extended to 3D [31]. DEA interpolates between PWB and a full RT analysis when increasing the basis size. It thus delivers a refined picture of the energy distribution compared to PWB.

The RT code is developed in MATLAB [41] as a part of this dissertation work. The DEA and PWB methods are conducted by a group at the University of Nottingham. Results from this joint work are published in an article and can be found in [33]. What is shown is that the three methods produce very similar results for the chaotic coupled cavity system that was considered. Then we show results for an RT formulation where incident angle dependent reflection coefficients were used and comparisons were made to full wave solutions.

#### *(A) Problem Setup*

In this section, we talk about the model for wave chaotic cavities with scatterers. We consider a 2D coupled cavity as shown in Fig. 3.1. The two cavities are coupled by an aperture in the middle. Each cavity is  $1 \times 1$  units and the aperture is 0.2 units. Both cavities are filled with circular scatterers each with a radius of 0.1 units. In addition, there are two port-like apertures on the top part of the two cavities each with an opening size of 0.1571 units (labeled  $P_1$  and  $P_2$ ).

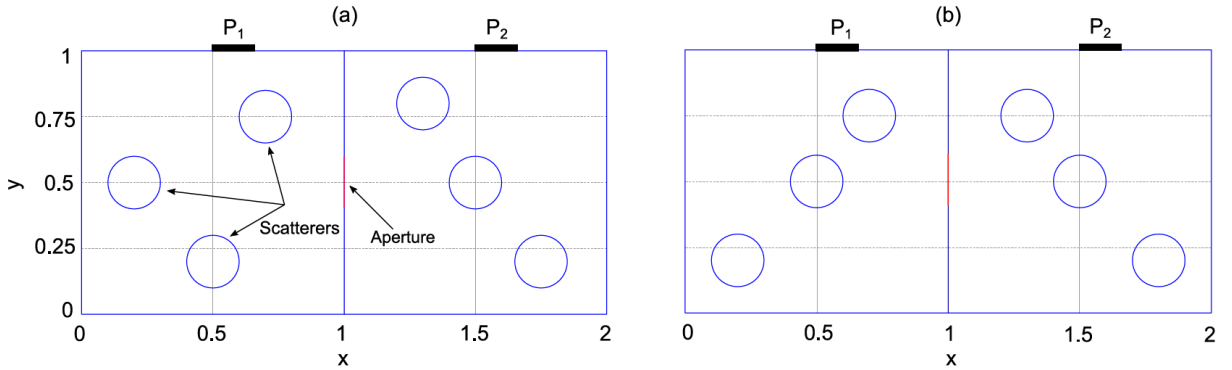


Fig. 3.1: Geometries considered for the comparison between the three high-frequency methods. It consists of two cavities of unit size side-length connected through an aperture of 0.2 unit length. Each cavity is equipped with a port connected to an external environment which is considered as an infinite-acting reservoir. The embedded circles are made of the same partially reflected material as the wall and can be considered as scatterers. All circles have the same radius of 0.1 units. Both ports have an opening size of 0.1571 unit length.

We assume that the boundary of the cavity and the scatterers are made of some material, whose loss is captured by a lossy reflection coefficient - related to the loss factor  $\alpha$  of the cavity. This loss factor  $\alpha$  for this chapter is defined as  $\alpha = I - R$ , where  $R$  is the power reflectivity of the materials of the walls and the scatterers. We further assume that scatterers and walls are made of the same material, thus leading to the same value of the reflection coefficient throughout. We have, here, treated the loss in an approximate way by making it independent of angle of incidence. We inject wave energy in Port 1. Then the waves propagate through the cavities and reflect from the walls and the scatterers. After some cavity dwell time, the energy will leave the system either through Port 1, Port 2 or be absorbed by a wall. Our goal is to calculate how much power is delivered either to Port 1 or 2 while we vary the loss of wall and object boundaries. We will compare the predictions of RT and the DEA to those of the PWB. To quantify the energy flow predicted by these methods we define energy fluxes across

apertures or ports connecting the two cavities and connecting each cavity to the exterior.

### *(B) Discussion of results for power delivery*

In Fig. 3.2(a) we show the computed spatial distribution of wave energy density using DEA, and in Fig. 3.2(b) we show a sample RT trajectory for the geometry of Fig. 3.1. The incident power is launched normal to the boundary through Port 1. In the DEA calculation shown in Fig. 4(a), the colour scale indicates the level of wave energy density. In the corresponding RT calculation, a total of 8002 rays were launched normal to the boundary of Port 1.

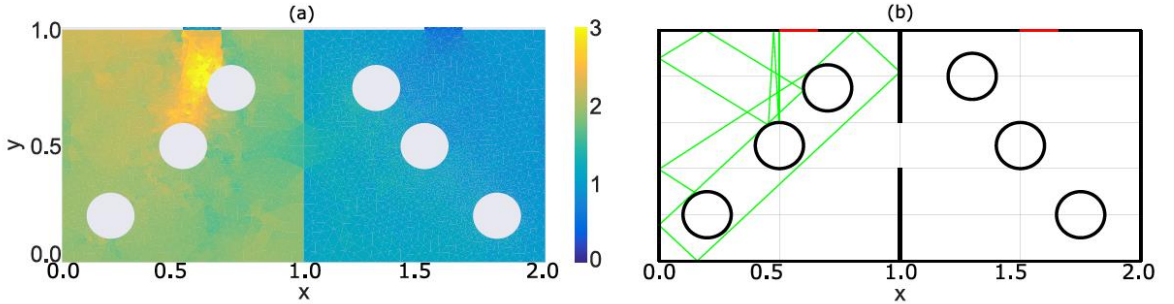


Fig. 3.2: Implementation of the cavity shown in Fig. 3.1(a) by the (a) DEA and (b) RT approach. Subplot (a) the energy density by means of DEA and (b) typical example of ray trajectory computed by the RT method. In both cases incident ray is directed normal from Port 1.

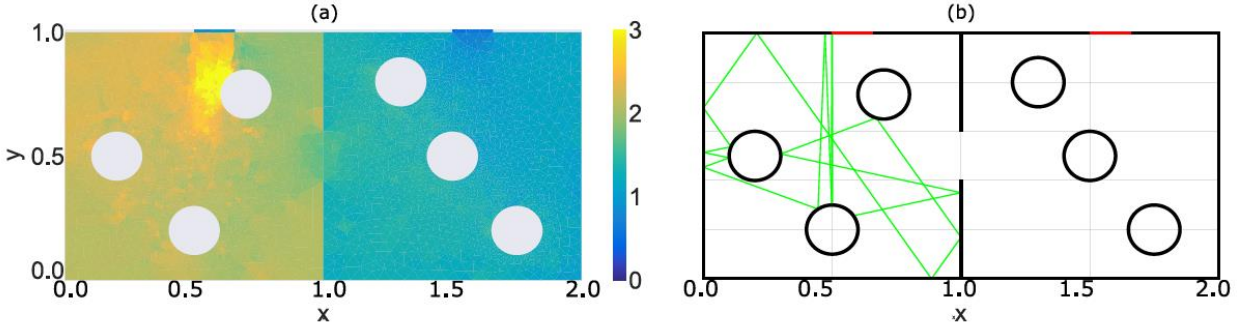


Fig. 3.3: We show the implementation of DEA and RT for a cavity for which we moved the scatterers. In particular, (a) the computation of wave energy density by means of DEA and (b) RT implementation with one sample ray trajectory. Both of these can be compared with the images in Fig. 4.

We vary the absorption parameter  $\alpha$  (equivalent to the power reflectivity  $R = 1 - \alpha$ ) of both the walls and the scatterers. The calculated powers at Port 1 and Port 2 versus the absorption coefficient  $\alpha$  are shown in Fig. 3.4 for the three methods. The quantities  $P_1^{port}$  and  $P_2^{port}$  refer to power leaving through Port 1 and Port 2, respectively. As shown in Fig. 6, DEA and RT follow closely the power balance results in the regime of low and intermediate losses. There is, however, a substantial deviation between DEA and RT on the one hand and PWB on the other hand in the high loss limit. The deviation at high losses can be understood in the following way. Both DEA and RT treat the propagation of energy through the cavities in full. For the given configuration, wave energy entering Port 1 must be reflected by at least one wall or scatterer section before it leaves through Port 1 or Port 2. At high losses, this means a substantially larger fraction of injected power will be lost to the walls than would be predicted based simply on the relative sizes of the ports and the wall. PWB assumes that the power is uniformly distributed within each cavity and thus there is a larger proportion of the energy near ports than in the actual energy flow calculations using RT or DEA.

We note that the DEA and RT results match very well for all  $\alpha$  except for  $P_1^{port}$  at high loss. This is due to numerical diffusion present in DEA calculations having a larger effect on direct processes, ie, energy leaving through Port 1 again after one or two reflections. Note also, that in the regime of low losses one finds a small deviation between RT/DEA and PWB. This is due to the fact that different positions of the scatterers lead to slightly different results for DEA/RT, whereas, the exact locations of the scatterers has no bearing on the PWB results. This is illustrated by calculations for the geometry depicted in Figs. 3.3 (a) and (b) where we have moved the scatterers of the left cavity to new positions. This leads to slightly different curves as shown in Fig. 3.5.

To understand this, we decrease the size of the apertures and the ports by a factor of 10 (Fig. 3.7(b)) and look at only the left cavity. We launch as a point source (i.e. equally in all directions) from various (x,y) co-ordinates in this cavity (given in Table 3.1). We calculate the power leaving the top and middle aperture. These results are seen in Fig. 3.6. This has no effect on the value obtained by PWB, but it reduces the variations for calculations based on RT and DEA. This can be understood by considering that PWB assumes a uniform distribution of wave energy across the cavities. For RT and DEA cases this holds in the limit  $\alpha = 0$  and small apertures, that is the wave energy has sufficient time to visit all of the available phase space. In the case shown in Fig. 3.2-3.3 energy is more likely to escape from the cavity before exploring the whole phase-space and thus leading to the deviation from PWB.

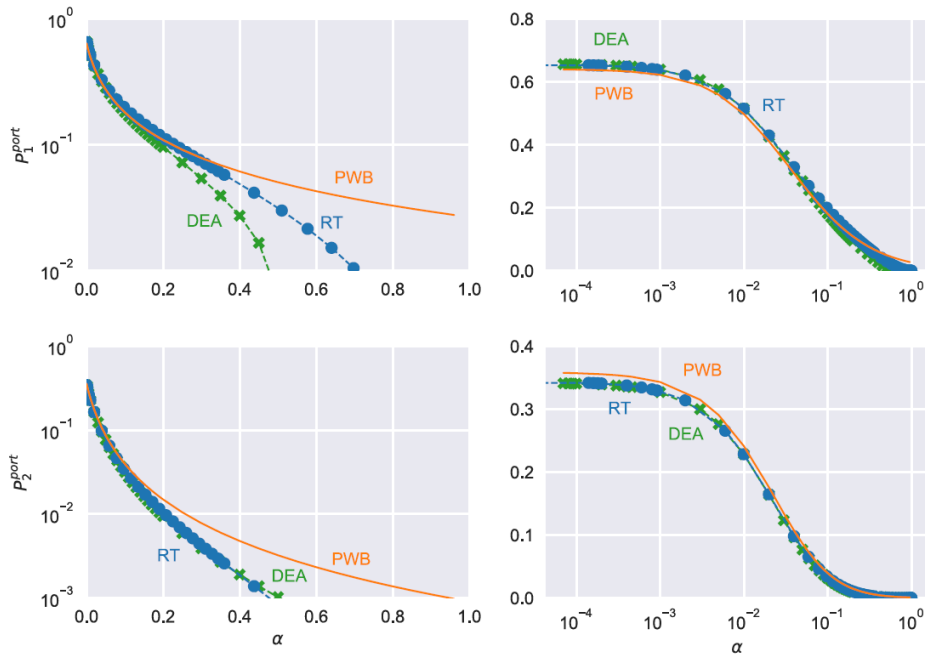


Fig. 3.4: The left column shows plots of power on log scale versus loss factor  $\alpha$ . The right column shows the same data except  $\alpha$  is on a log scale and power on a linear scale.  $P_1^{\text{port}}$  and  $P_2^{\text{port}}$  refer to power escaping through Port 1 and 2, respectively.

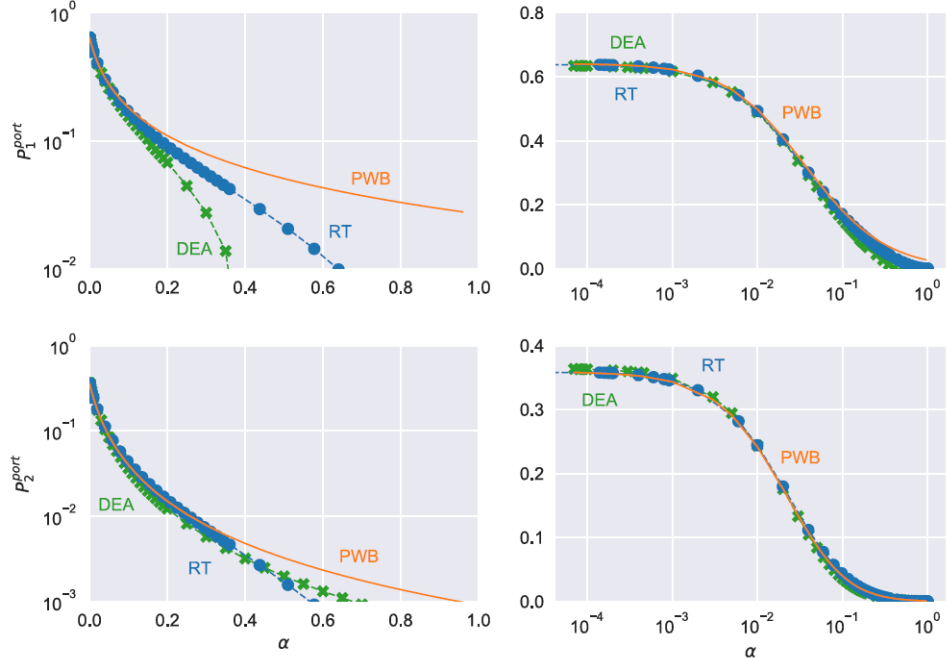


Fig. 3.5: The left column shows plots of power on log scale versus loss factor  $\alpha$ . The right column shows the same data except  $\alpha$  is on a log scale and power on a linear scale.  $P_1^{\text{port}}$  and  $P_2^{\text{port}}$  refer to power escaping through Port 1 and 2, respectively.

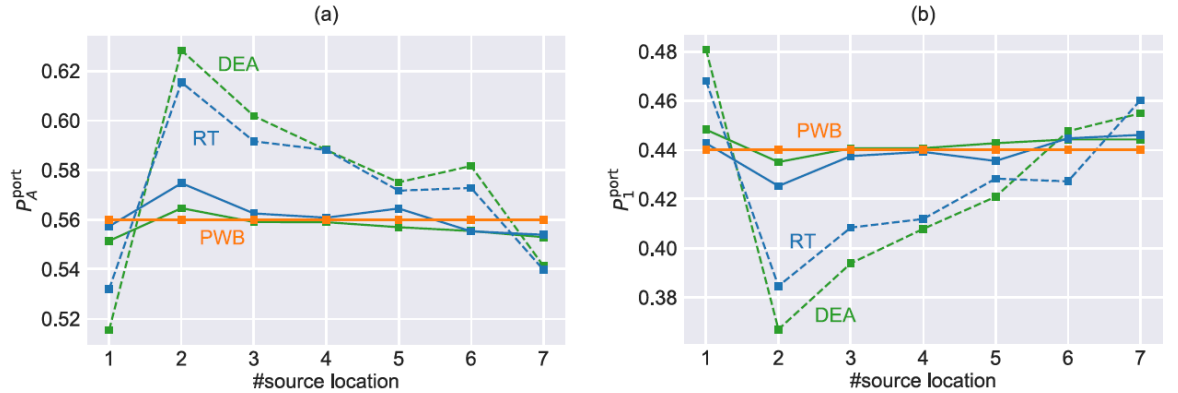


Fig. 3.6: Power flux versus point source locations (see Table 3.1) for the geometry shown in Figs 3.7 (a)- (b) and calculated using the three high-frequency methods at  $\alpha = 0$  (no wall damping). Power flux exiting from (a) the side Port  $P_A^{\text{port}}$  and (b) the top Port  $P_1^{\text{port}}$ . In (a)-(b), the dotted lines are for the structure in Fig. 3.7(a) and solid lines are for the structure in Fig 3.7(b).

**Table 3.1**

Source #	1	2	3	4	5	6	7
(x,y)	(0.1,0.9)	(0.9,0.1)	(0.5,0.4)	(0.4,0.1)	(0.25,0.2)	(0.9,0.9)	(0.1,0.5)

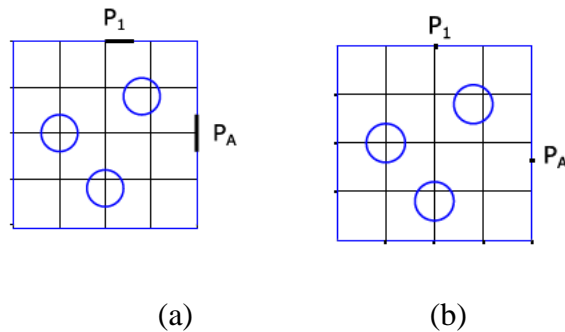


Fig. 3.7: On (a) we see the two cavity system reduced to only the left cavity while we consider power leaving only the top and the middle/side aperture when we launch power from inside the cavity as point source. On (b) we have the same system but the aperture sizes have been reduced by a factor of 10.

Thus, by inspecting the results in Fig. 3.6, we can conclude that a smaller aperture size leads to better agreement between the three methods.

In conclusion we have compared under controlled conditions three different approximate methods of computing wireless power distribution in multi-cavity systems in this chapter. These are the power balance method (PWB), equivalently the statistical energy analysis (SEA), ray tracing (RT) and the dynamic energy analysis (DEA). All three methods apply to situations in which the wavelength of the radiation is much smaller than the typical length scales in the problem. As such these approximate methods are computationally more efficient than full wave computations.

Of the three methods RT and DEA both include propagation effects and account for details of the geometry of the region being modelled. In principle, these two methods are mathematically equivalent, although different in implementation. A subsection in [11] shows a mathematical derivation analytically showing that DEA and RT are equivalent. This has been proven here in this chapter numerically from the similarity of the graphs of power deliveries between the DEA and RT at various losses. Also, we find that the three methods generally make the same predictions for gross quantities such as the power leaving through ports or dissipated in walls. There are discrepancies between PWB and the other two methods in the prediction of these gross quantities in cases where the assumptions needed for PWB are not met. Specifically, when the energy decay time is too short to allow energy to become uniformly distributed

throughout phase space. Examples of this are cases where the wall absorption coefficient is close to unity. A similar situation occurs in configurations where ports are so large that EM wave randomization is incomplete. We have found some small deviations between DEA and RT which we attribute to numerical diffusion in the DEA method.

In continuation of these results, in the next section we show results where an incident angle dependent reflection coefficient was introduced and compared with HFSS simulations.

*(C) Results for power delivery using incident angle dependent reflection coefficient*

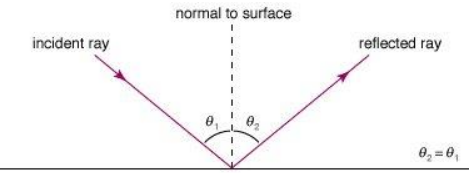
Up to now, all the results shown in this chapter were based on the assumption that the reflection coefficient for calculating power is independent of incident angle. Since this is not generally the case, we now show results where the power absorbed by walls and scatterers depends on incident angle. Our motivation for doing this is that our previous comparisons of RT, DEA, and PWB involved approximate solutions of the wave equations only. In this section we will compare the approximate solutions with full format solutions (HFSS). In order to make valid comparisons it is necessary to treat wall absorption consistently in all methods.

When a wave with incident angle  $\theta$  strikes a surface with surface impedance  $R_s$ , a wave with electric field reflection coefficient  $R$  is reflected with the same angle of reflection  $\theta$  (Fig. 3.8(a)), where

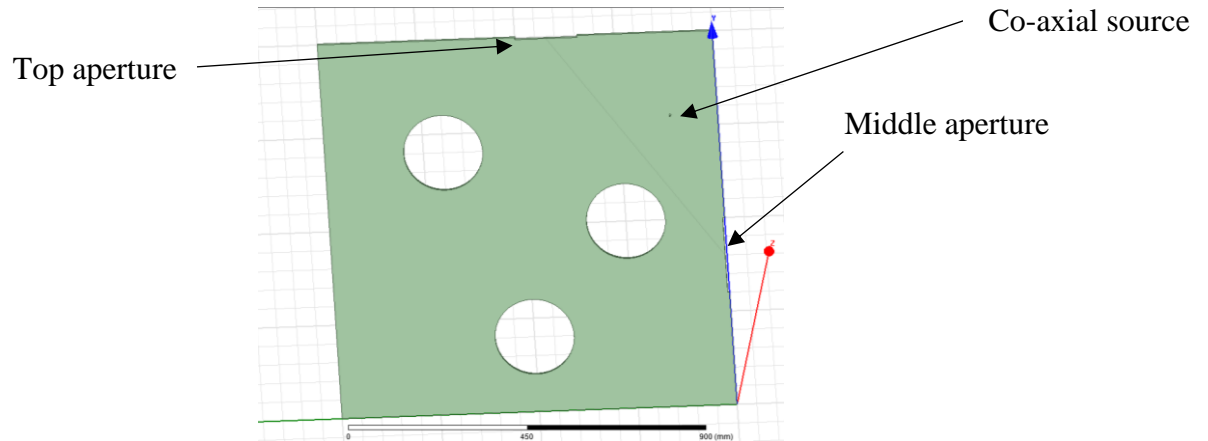
$$R = \frac{R_s - Z_0 / \cos\theta}{R_s + Z_0 / \cos\theta} = \frac{\eta \cos\theta - 1}{\eta \cos\theta + 1} \quad (3.1)$$

where  $\eta = R_s / Z_0$  and  $Z_0 = 377 \Omega$  is the impedance of free space. This is then used to calculate power in the same way as in Chapter 2, Section B using the formula  $P_{n+1} = |R|^2 P_n$ , where  $n$  refers to the bounce number,  $P_n$  is the power contained in the ray after the  $n$ -th bounce and  $R$  is the power reflectivity shown in (3.1). So, after each bounce the ray loses  $(P_n - P_{n+1})$  amount of power, as before.

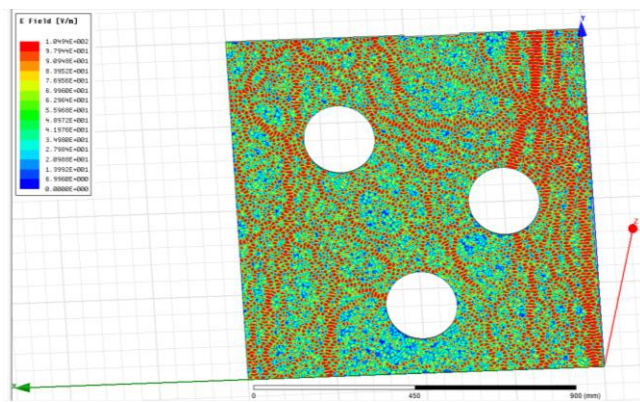
The geometry we investigate is the same as in Fig. 3.7(a). This geometry was designed in HFSS as shown in Fig. 3.8 (b). This was then also created using the RT code.



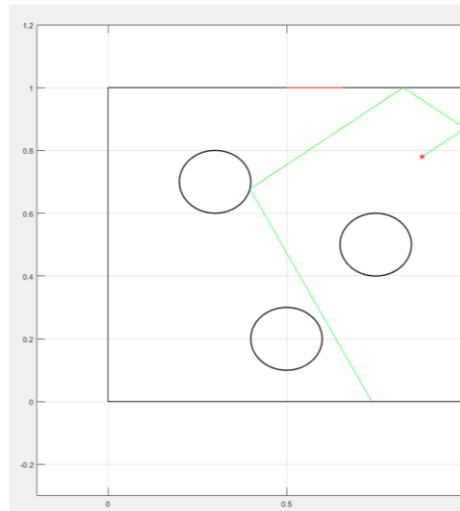
(a)



(b)



(c)

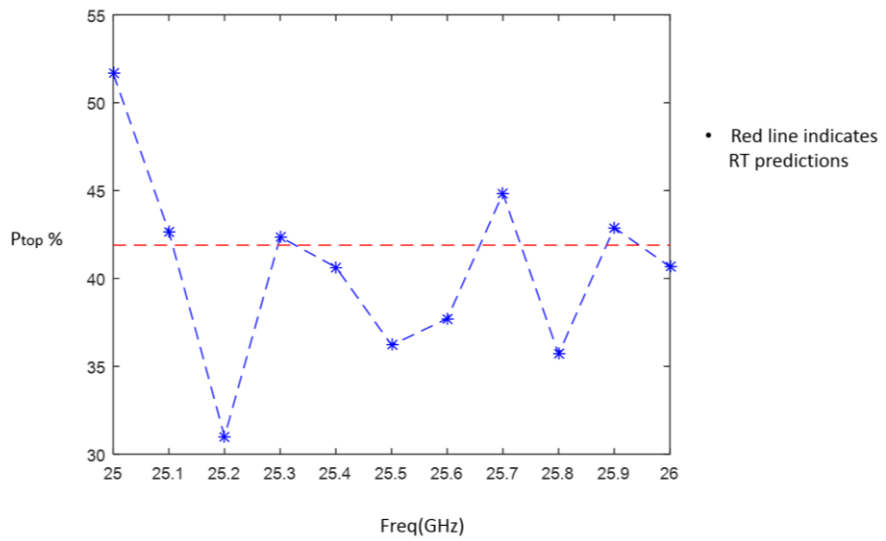


(d)

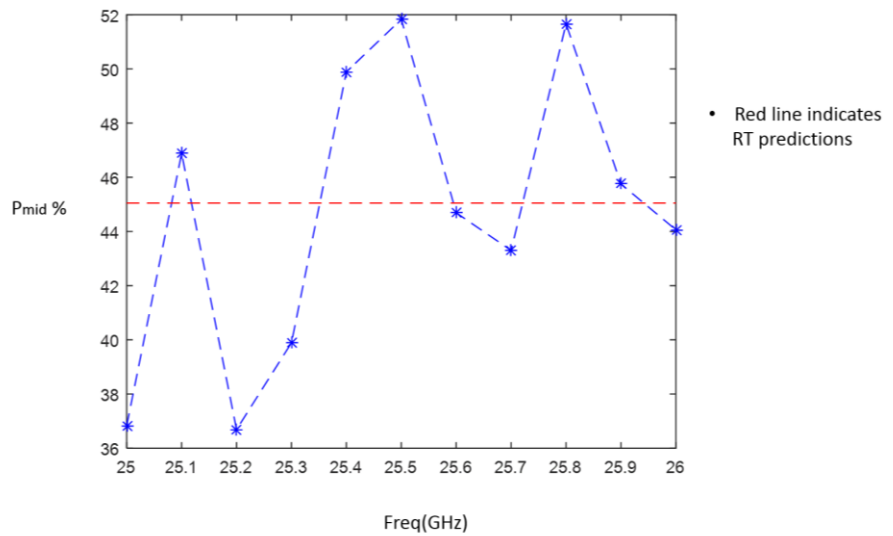
Fig. 3.8: (a) Schematic diagram showing incident and reflected rays. Figure from. (b) HFSS model of a single cavity with scatterers and two aperture-like ports and a co-axial cable as source. These apertures have a loss of 377 Ohms while the straight walls have a loss of 1 Ohm. The circular scatterers were fully reflective. (c) E-field plots in the cavity of (b) at 25.3 GHz. (d) RT model of the cavity of (b) showing one sample ray trajectory.

We use a co-axial cable to launch EM energy in the cavity as shown in Fig. 3.8(c). The circular scatterer had no loss while the straight boundaries had a loss of 1 Ohm. We also add a loss of 377 Ohms to the two aperture-like segments to simulate, in a controlled way, loss of power through the apertures. In principle, power escaping at an aperture requires solution of the wave equation subject to some form of outgoing wave boundary condition. However, this often is done approximately. So, to ensure that the aperture is treated the same way in the HFSS computations as well as in the approximate methods, DEA, RT, and PWB, we applied an impedance boundary condition.

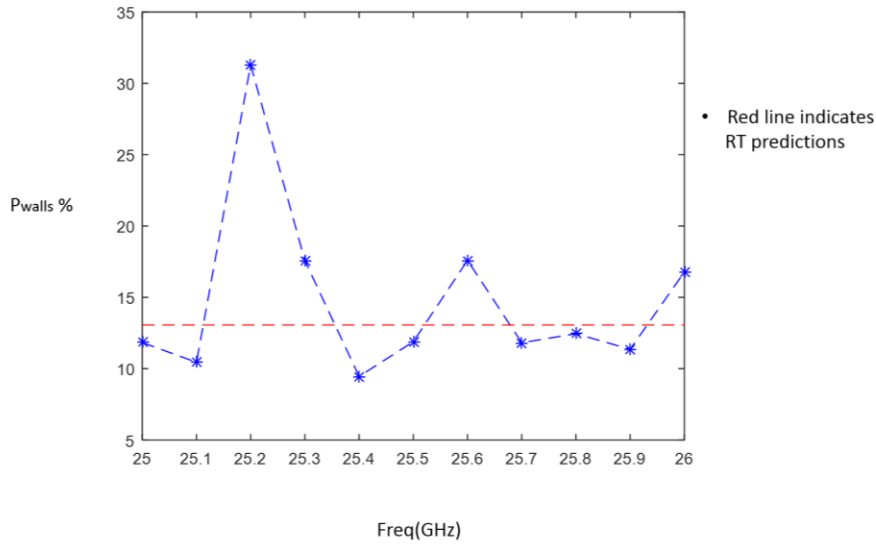
The co-axial port is centered at location  $x=0.88$  cm,  $y=0.78$  cm. This had an inner radius of 0.635 mm, but had an outer radius of 2.29 mm. We launch 8002 rays as a point source in our RT code and simulate the same cavity and the same boundary conditions in MATLAB. For HFSS simulations, we do frequency sweeps at 5-6 GHz, 15-16 GHz and 25-26 GHz and calculate the power absorbed at the top and middle aperture and the straight walls. Results for a sample range of 25-26 GHz are shown in below.



(a)



(b)



(c)

Fig. 3.9: HFSS results for power absorptions calculated at the boundary for frequency of 25-26 GHz shown as a percentage. The blue curves in (a), (b), (c) shows power absorbed at the top and middle aperture and the straight walls, respectively. The red line shows RT calculations which is independent of frequency.

What we see in Fig. 3.9 is that at various frequencies, we have calculations in HFSS of power absorbed at the two apertures and walls which are close to the RT calculations. Even though the blue and red curves here are not exact, the values at different frequencies for the blue curve oscillate around the red line. If we take a mean of these losses in HFSS, we get results as tabulated in Table 3.2. This table shows that the mean values get closer to the RT calculations as we go higher in excitation frequency. This is expected. At the higher frequencies we expect the full wave results to be close to the ray approximation.

**Table 3.2**

<b>Freq Range (GHz)</b>	<b>Ptop (%)</b>	<b>Pmid (%)</b>	<b>Pwalls (%)</b>
25-26	40.5755	44.6791	14.7718
15-16	45.39	42.5627	9.6545
5-6	38.08	50.7027	11.3345
RT results	41.89	45.05	13.06

Also, we look at the standard deviations of the full wave results in Fig. 3.9. What we find is that these deviations also become smaller as we increase the excitation frequencies. This is shown in Table 3.3. This also suggests that at even higher frequencies we would get closer match with our RT results.

**Table 3.3**

<b>Freq Range (GHz)</b>	<b>Ptop (%)</b>	<b>Pmid (%)</b>	<b>Pwalls (%)</b>
25-26	5.4477	5.3260	6.1850
15-16	9.2449	7.5019	1.6981
5-6	14.6426	13.8744	5.3529

But such higher frequencies cannot be pursued here as the computation power required for it is beyond the scope of the resources at our disposal.

In summary, we see that the angle dependent reflection coefficient measurements of power absorbed in our chaotic cavity using RT is closely matched by our full wave simulations.

In the next chapter the same RT code was applied to calculate the impedance for a two-port system in a chaotic cavity using the so called 'Short Orbit Formulation' (SOF).

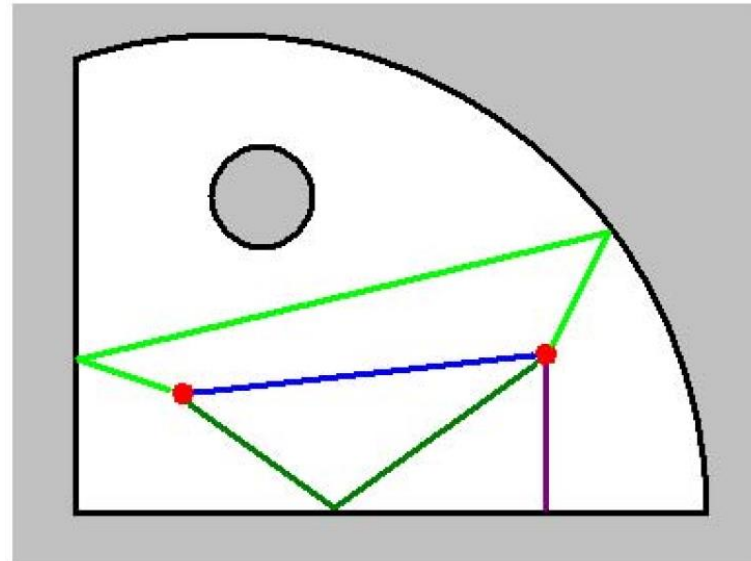
## Chapter 4: Results for cavity impedance calculations

In this chapter, results are shown for the Short Orbit Formulation (SOF) as discussed in Chapter 2, Section D. A chaotic geometry was chosen for the ray tracing (RT) calculations. The same RT code was used for the calculations of Chapter 3. But this time the calculations are for a single chaotic cavity and not multiple connected cavities. Rays were launched inside this cavity at the sending port and tracked to the receiving port to calculate the real and imaginary parts of the impedance  $\langle \mathbf{Z}_{12} \rangle$  according to Eq. (2.28) at various frequencies. A 5 to 7 GHz frequency range was chosen because the previous work by Hart et al [21] and Yeh et al [22] employed this same frequency range. Their work was concerning the so called 'Short Orbit Corrections' to the RCM. Using these corrections Hart et al [21] arrived at the equations for the impedance of a cavity  $\mathbf{Z}_{R,n,m}$  as shown in Eq. (2.25). But first a more detailed discussion of short orbits is carried out here.

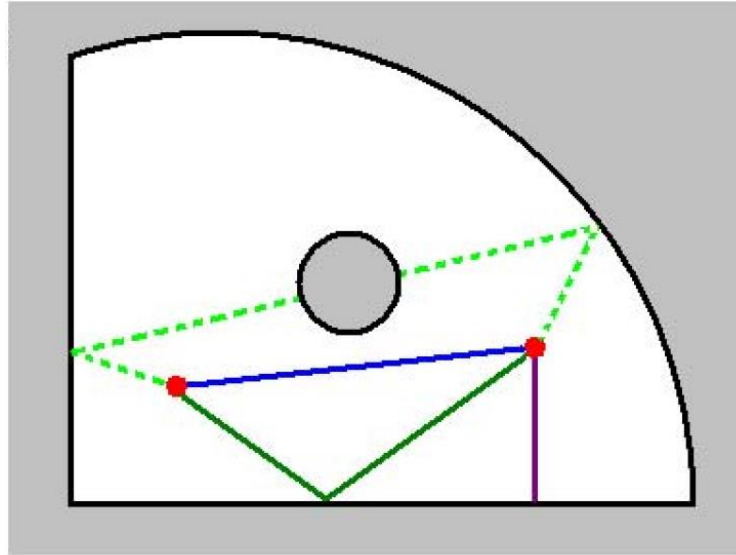
A 'short orbit' refers to a ray trajectory whose length is not much longer than several times the characteristic size of the EM enclosure. Generally, the length of the orbits that are of interest is determined by the range of frequencies over which the window average of the impedance is desired. For example, if the window average is made with a Lorenzian kernel of width  $D\omega$ , the average is equivalent to evaluating the exact impedance at a complex frequency,  $\omega + iD\omega$ . From expression (2.28) it can be seen

that the contributions from orbits of duration  $DWT_{ab} > 1$  will become exponentially small.

This type of trajectory is shown in a two-dimensional cavity in Fig. 4.1 as a cartoon diagram taken from [42]. The circular scatterer is a movable object for creating different boundary realizations and is used to create an ensemble.



(a)



(b)

Fig 4.1: Illustrations of short orbits in a 2D cavity with a circular scatterer. The red dots are the ports and colored lines are examples of short orbits. The blue lines are direct orbits. The two-bounce orbit (light green) in (a) is blocked in (b) due to the shift of the scatterer. Figure taken from [42].

In such a system short orbits can also leave and return to the same port, such as the one-bounce orbit in purple in Fig 4.1.

In measuring the statistics of wave scattering properties, one needs an ensemble measurement of many different realizations. To do that one can vary the geometrical configuration of the cavity or take measurements at different frequencies. These ensembles aim to create a set of systems in which none of the non-universal system details are reproduced from one realization to another (except for the effects of the port details). Thus, by suitably accounting for the port details as the radiation impedance

matrix in the RCM, it is expected that only the universal RMT properties would remain in the ensemble data and non-universal effects will be removed.

But this approach does not work well enough for various reasons. Firstly, in the case of geometrical configuration variation, researchers move perturbing objects inside a ray-chaotic enclosure or move one wall of that enclosure, to create an ensemble of systems with varying details. But the problem is that certain walls or other scattering objects of the enclosure remain fixed throughout the ensemble. Therefore, there may exist relevant ray trajectories that remain unchanged in many or all realizations of the ensemble. Thus, some short orbits remain.

Secondly, similar problems can arise for frequency variations. Within a limited frequency range, the variation of the phase accumulated by a wave following that short orbit may not be large enough to be considered random. In such a case the effect of specific (i.e., nonuniversal) short orbits will survive the ensemble averaging processes. Such short orbits have been studied in the context of quantum scattering theory [43-45]. Short orbit effects have been noted in microwave billiards [46-48] or for quantum transport in chaotic cavities [49]. The short-orbit effect on wave scattering properties of chaotic systems has been explicitly calculated in the case of quantum graphs [50] and for two-dimensional billiards [21]. Such short orbit effects had previously produced inaccurate results for the RCM and 'short orbit corrections' were introduced by Hart [21].

But the Hart et al. and Yeh et al. approaches for calculating the short orbit correction matrix  $\zeta$  were based on semiclassical approaches and were different from the RT approach applied in this chapter. The RT approach was explained in Chapter 2, Section D leading to Eq. (2.31). But for the semiclassical approach, an  $N$ -port system, the  $(n,m)$  element of the  $N \times N$  matrix is described as

$$\zeta_{n,m} = \sum_{b(n,m)} -p_{b(n,m)} \sqrt{D_{b(n,m)}} \exp(-(ik + \kappa)L_{b(n,m)} - ikL_{\text{port}(n,m)} - i\beta_{b(n,m)}\pi) \quad (4.1)$$

where  $b(n,m)$  is an index over all classical trajectories which leave the  $n$ th port, bounce  $\beta(n,m)$  times, and return to the  $m$ th port. The quantity  $p_{b(n,m)}$  is the survival probability of the trajectory due to the positions of the perturbing objects in the ensemble. The orbit stability factor  $D_{b(n,m)}$  is a geometrical factor of the trajectory,  $k$  is the wave number, and  $\kappa$  is the effective attenuation parameter taking account of wave propagation loss.  $L_{b(n,m)}$  is the length of the trajectory  $b(n,m)$ , and  $L_{\text{port}(n,m)}$  is the port-dependent constant length between the  $n$ th port and the  $m$ th port.

However, in this chapter the RT approach is employed and it is shown that  $\zeta$  can be calculated via the short orbits found by launching rays from a point source instead of following the algorithm in the Appendix of [42].

#### (A) Problem setup

A quasi 2D quarter bowtie cavity as shown in Fig. 4.2 is considered for the  $Z_{12}$  calculations. Rays are launched from a point source inside the cavity representing sending port. The rays can then bounce around inside the cavity and pass by the

receiving port. Various boundary conditions for the cavity is considered. First, full absorbing boundaries is considered where after the launch the rays all get absorbed as soon as it hits a boundary. Then various other combinations of boundary conditions are considered. For example, in some cases one of the boundaries is made perfectly reflective (PEC) where rays would just bounce off without losing any energy. But the other boundaries remained fully absorbing. This gives the ray more than one path to arrive at the receiving port i.e. even if a ray does not directly travel to the receiving port after launch it can arrive there after one bounce. This is shown in Fig. 4.4 which also shows the model of the receiving at the target port. We look at any two adjacent rays which started off next to each other but after one or more bounces ended up on either side of the target port. Taking the mean distance traveled by these rays gives us an approximation of the ray that would have ended up hitting the target port had we launched at an angle in between. In this way we can calculate the short orbits.

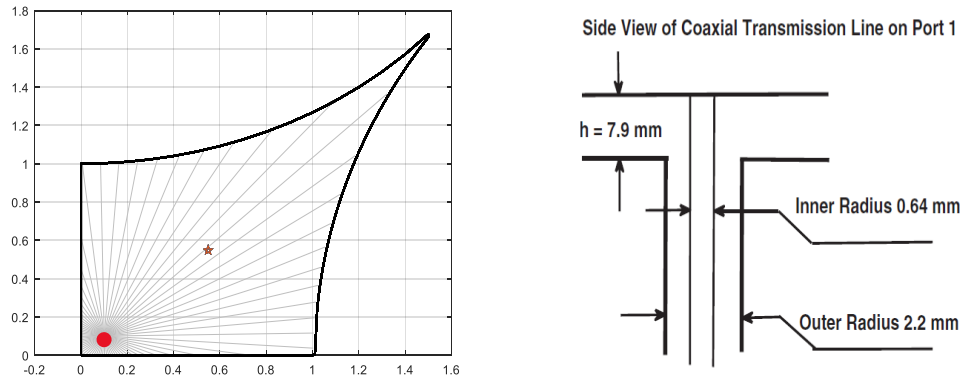


Fig. 4.2: On the left, a of a quasi 2D quarter bow-tie cavity is shown generated by the RT code. A bundle of rays is launched from a point in the cavity. This is the transmitting point shown with a red circle. The star indicates a receiving port. On the right, we see

side view of a port of the bowtie cavity. This figure on the right is taken from [21] and is used to illustrate the geometry of the cavity

These works are then compared with previous works done theoretically by Hart et al. [21] and experimentally validated by Yeh et al. [22]. The same geometry was also recreated in this work using HFSS as shown in Fig. 4.3. Two coaxial cables are used to bring energy into the cavity. These are our two ports similar to the point sources in Fig. 4.2.

The dimensions for HFSS modeling are thus: the lower and left straight sides of the cavity have lengths  $L_1=43.18$  cm and  $L_2=21.59$  cm, respectively, and the upper and right sides have radii of curvature  $R_1=103$  cm and  $R_2=63.9$  cm, respectively. Port 1 is centered at location  $x=18.03$  cm,  $y=10$  cm and port 2 is at  $x=32.43$  cm,  $y=10$  cm. Distance between ports is 14.4 cm. Thickness of the bowtie is 7.9 mm. Both ports have an inner radius of 0.635 mm, but port 1 has an outer radius of 2.29 mm and port 2 has an outer radius of 3.05 mm.

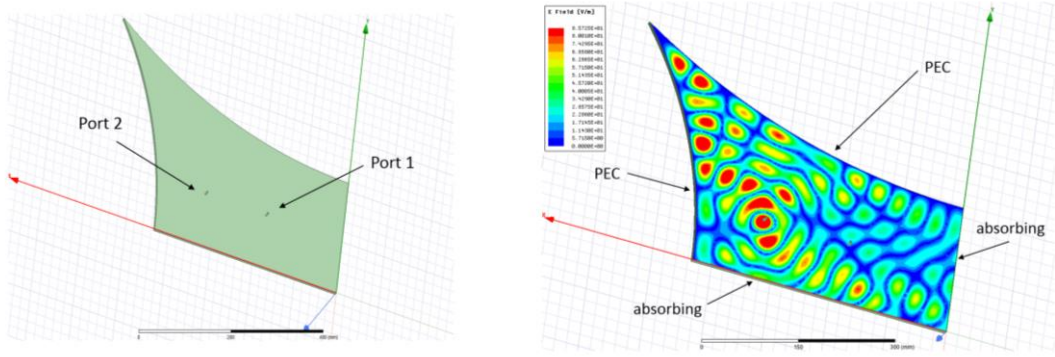


Fig 4.3: On the left, we see the bowtie cavity created in HFSS. On the right we see the same cavity but the E-field oscillations were shown. Various boundary conditions are done. But here we see a sample boundary condition.

These dimensions were made similar to the work by Hart and Yeh. The same geometry was recreated in MATLAB using the RT code. In Fig. 4.4 a pair of sample rays were shown which started adjacent to each other and ended up straddling the target port on either side. The equation that was used to calculate the  $\zeta$  is repeated here for convenience

$$\zeta_{12} = \sum \left( \frac{2j\Delta\theta}{\pi k_0 \Delta} \right)^{1/2} (-1)^m e^{-jr_{12}k_0} \quad (4.2)$$

This equation can in turn give us  $Z_{12}$  using the equation as described before

$$Z_{12} = \zeta_{12} (R_{rad1} R_{rad2} G_1 G_2)^{1/2} \quad (4.3)$$

The  $R_{rad}$  is found from HFSS simulation using all absorbing boundary conditions. In the next few figures, the comparison between HFSS results and RT results for the described cavity geometry is shown in Fig. 4.5. In the first figure we see the real and

imaginary parts of the  $\mathbf{Z}_{12}$  for all absorbing boundary conditions. As can be seen, they are agreeing well. Similarly, the next few graphs show various boundary conditions and each time we compare the real and imaginary parts of  $\mathbf{Z}_{12}$ .

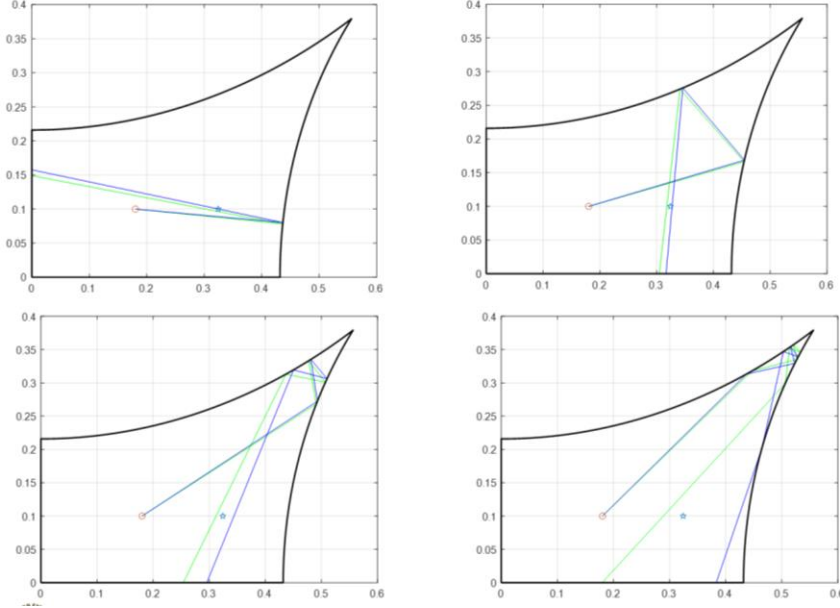


Fig. 4.4: The 2D cavity created in MATLAB using the RT code showing a pair of adjacent rays straddling the target port after few bounces. All straight walls are absorbing, curved walls are PEC in this figure. The red and blue ports indicate the transmitting and receiving ports, respectively.

As can be seen, we have good agreement between the full wave solution and the SOF in each of these graphs. However, there can be a phase difference seen in all these curves between SOF and HFSS results. This is explained in the next paragraph.

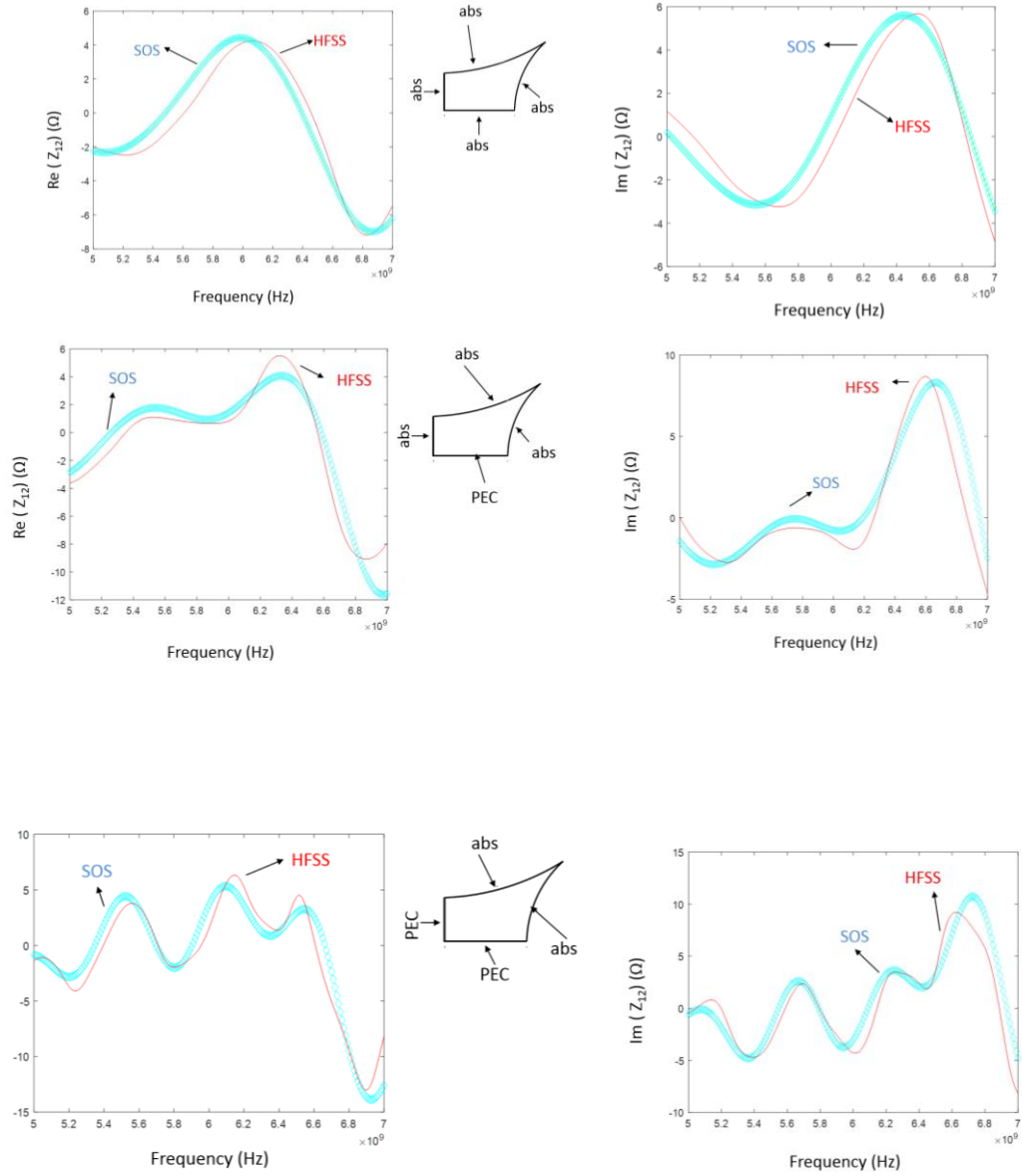


Fig. 4.5: Various graphs showing comparison between the SOF, here referred to as SOS (short for Short Orbit Summation) and HFSS. The red curves are for HFSS, blue ones for SOS. In the small cartoon of the bowtie various boundary conditions are illustrated.

This phase shift exists due to the fact that in the HFSS simulations, we model the port in detail as a circular cross section coaxial transmission line in which the outer

conductor contacts the upper plate and the inner conductor extends the short way across the cavity and contacts the lower plate. This shape and dimensions of port 1 are shown in Fig. 4.2. Port 2 has the same geometry as port 1, but with an outer radius of 3.0 mm. This more detailed port model results in an additional phase shift that is not treated in this simple model of Eq. (2.35), where we add a fixed current source to the wave equation. But as we see a close agreement between the two methods except the phase difference, it is concluded that the SOF is producing the results as expected.

Thus, it was shown in this chapter that the SOF is accurate enough to model various boundary conditions for a quasi 2D bowtie cavity using RT. This conclusion was reached after comparing the RT results with the full wave solutions in HFSS. In the next chapter we further investigate the effect of short orbits in the same bowtie cavity. But this time a directed beam is used to launch energy into the cavity and a circular scatterer is also placed inside the cavity to create different realizations. This leads to short orbits that creates deviations from the RCM predictions.

## Chapter 5: Breaking the RCM predictions with a directed beam

In this chapter, we report an investigation of whether the RCM is applicable if a highly directed beam is used to launch energy into a chaotic cavity. All the previous RCM studies in 2D have utilized a source which radiates isotropically. Here we consider the effect of a source with a directed beam.

The basis for much of the previous work on RCM is ‘the random plane wave hypothesis’ [51-53, 14]. In short, this hypothesis states that the fields within the cavity behave like a random superposition of isotropically propagating plane waves. Therefore, the eigenfunctions  $\phi(\mathbf{X})$  of the Helmholtz equation can be approximated by a superposition of the plane waves with wavenumber  $k_n$  such that

$$\phi(\mathbf{X}) = \sum_{j=1}^N a_j \cos(ik_n \hat{\mathbf{e}}_j \cdot \mathbf{X} + i\theta_j) \quad (5.1)$$

where  $a_j$  is an independent and identically distributed random variable,  $\hat{\mathbf{e}}_j$  is independent isotropically distributed random vector,  $\theta_j$  is an independent and uniformly distributed random variable in  $[0, 2\pi]$ .

The eigenfunctions can be thought of as a superposition of a large number,  $N$  of plane waves. A simple estimate of  $N$  is as follows. One way to calculate the eigenfunctions is to represent them as a superposition of  $N$  plane waves, with amplitude coefficients that are determined by the cavity shape through the application of the boundary

condition that the eigenfunction vanishes on the boundary. To determine the  $N$  amplitudes one should evaluate the superposition at  $N$  points on the boundary, thus turning the problem into an  $N$  by  $N$  linear matrix equation. The actual wave function varies spatially on the scale of a wavelength. Therefore, it is expected that the number of independent points on the boundary needed to determine the eigenfunction would be the ratio of the perimeter to half the wavelength,  $N = 2 \cdot \text{Perimeter} / \lambda$ . The coupling coefficients in the RCM are proportional to the port directivity averaged over the  $N$  plane waves. For large  $N$  this becomes the average of the port directivity. However, there are fluctuations that scale as  $N^{-1/2}$ . If the port is highly directive these fluctuations are enhanced. Furthermore, it is expected that such a directed beam would lead to enhanced short orbit effects (short orbit effects were discussed in chapter 4, section A). Evidence for that prediction is also presented in this chapter.

#### *(A) Problem setup*

We designed a bowtie cavity as shown in Fig. 5.1 in HFSS. The dimensions of the bowtie are the same as discussed in Chapter 4, Section A. But here the energy is injected as waves launched from the boundaries of the bowtie as a wave port. This is done to simulate apertures to increase the directivity of the EM energy that is injected. Both the apertures are 110 mm wide and will act as Ports 1 & 2. We also put a circular scatterer in the cavity which has a radius of 40 mm. This will be placed in various positions inside the cavity to create a number of realizations. Table 5.1 shows the (x,y) coordinates of the center of the scatterer for various positions.

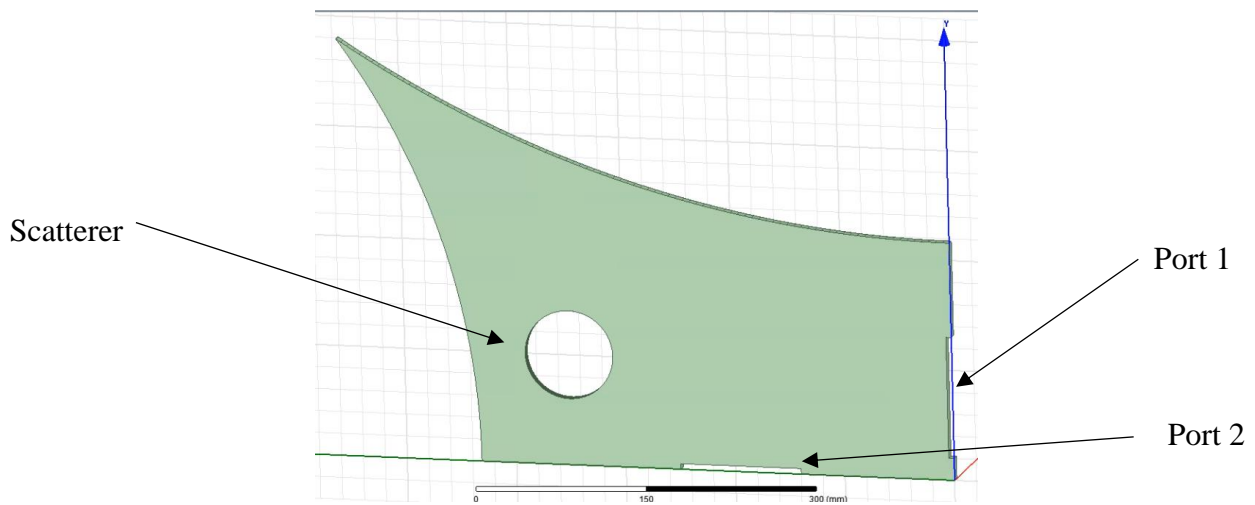


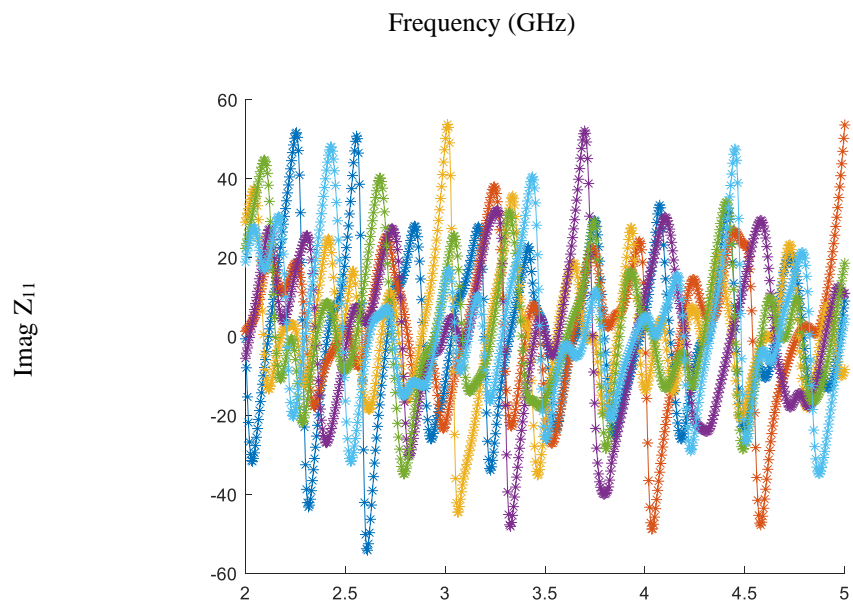
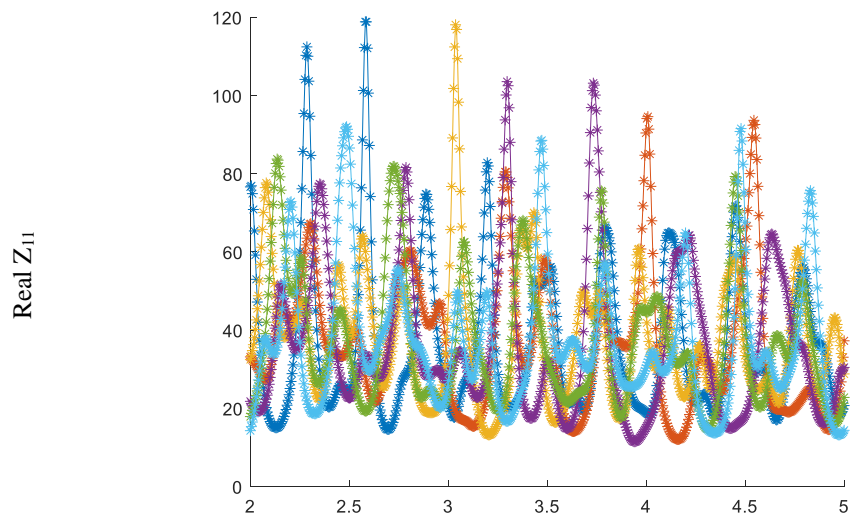
Fig. 5.1: View of the quasi 2D bowtie cavity with a circular scatterer created in HFSS

### *(B) Results*

We did a frequency sweep in HFSS and plotted the real and imaginary values of the Z matrix versus frequency for various positions of the scatterer for a frequency range of 2-5 GHz as shown in Fig. 5.2. The walls of the bowtie had a surface resistance of 80 Ohms while the scatterer was perfectly reflective. The apertures were treated as wave ports. Results for each of the six scatterer positions are indicated with different colors. What can be seen is that various scatterer positions show distinctly different curves. These results in Fig. 5.2 are unnormalized. We then normalize these datasets using the formulas described in the next paragraph.

**Table 5.1**

Scatterer Position	1 (blue)	2 (red)	3 (orange)	4 (purple)	5 (green)	6 (cayan)
(x,y) m	(0.4,0.25)	(0.3,0.05)	(0.35,0.2)	(0.35,0.1)	(0.27,0.195)	(0.17,0.17)



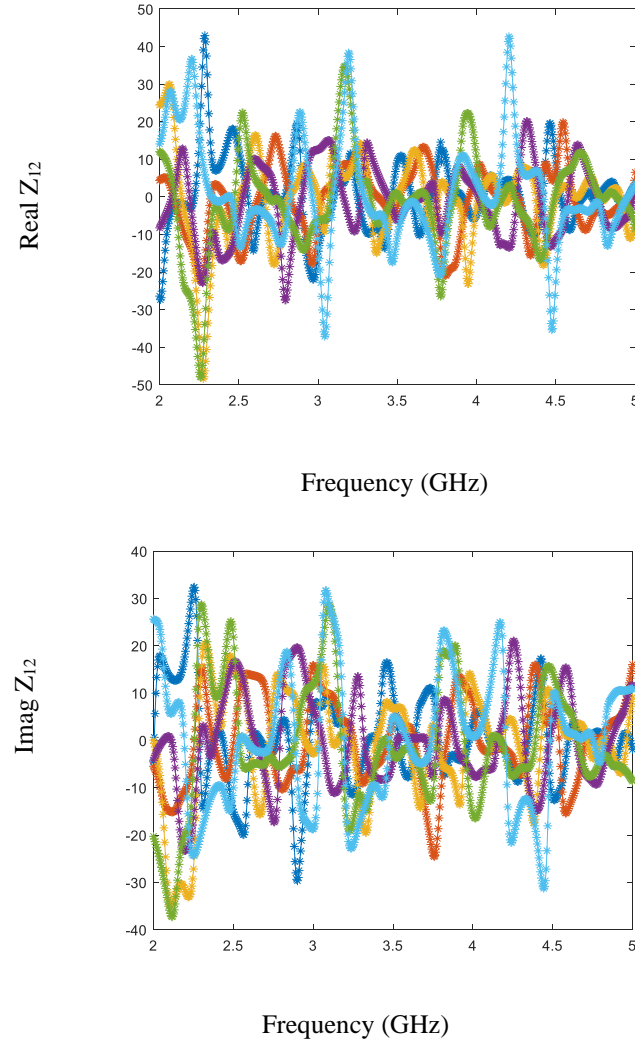
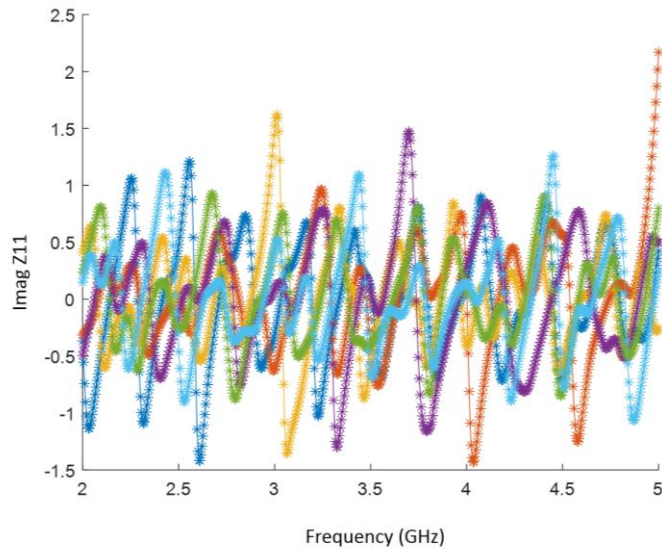
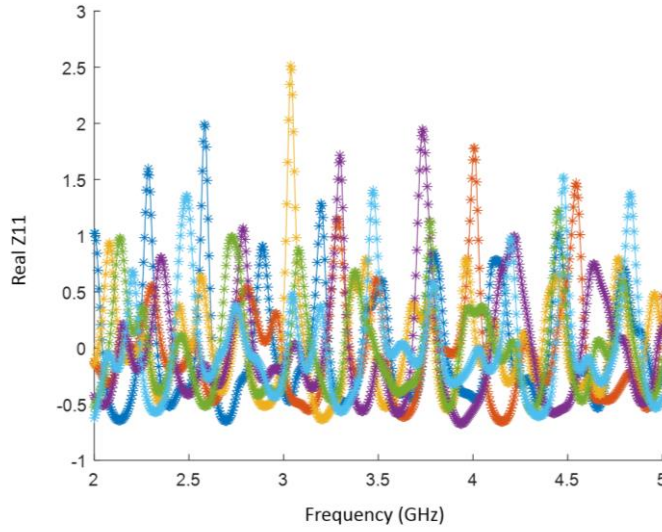


Fig. 5.2: Top to bottom: real and imaginary parts of various components of the  $Z$  matrix vs frequency for an aperture-like port. Different colors represent different scatterer positions as described in Table 5.1. These results are unnormalized.

We normalize these data using the formula

$$\begin{bmatrix} \xi_{11} & \xi_{12} \\ \xi_{21} & \xi_{22} \end{bmatrix} = \begin{bmatrix} \frac{Z_{11} - \bar{Z}_{11}(\omega)}{\bar{R}_{1,\text{rad}}} & \frac{Z_{12} - \bar{Z}_{12}(\omega)}{\sqrt{\bar{R}_{1,\text{rad}} \bar{R}_{2,\text{rad}}}} \\ \frac{Z_{21} - \bar{Z}_{21}(\omega)}{\sqrt{\bar{R}_{1,\text{rad}} \bar{R}_{2,\text{rad}}}} & \frac{Z_{22} - \bar{Z}_{22}(\omega)}{\bar{R}_{2,\text{rad}}} \end{bmatrix} \quad (5.2)$$

where  $\xi_{nn}$  represents the normalized impedance. The quantity  $\bar{Z}_{nn}(\omega)$  represents the average impedance which is a mean taken over all the scatterer positions. The  $R_{rad}$  quantities are generated as  $\bar{R}_{1,rad} = \text{Re}\{\bar{Z}_{11}(\omega)\}$ ,  $\bar{R}_{2,rad} = \text{Re}\{\bar{Z}_{22}(\omega)\}$ . These normalized data are shown below in Fig. 5.3.



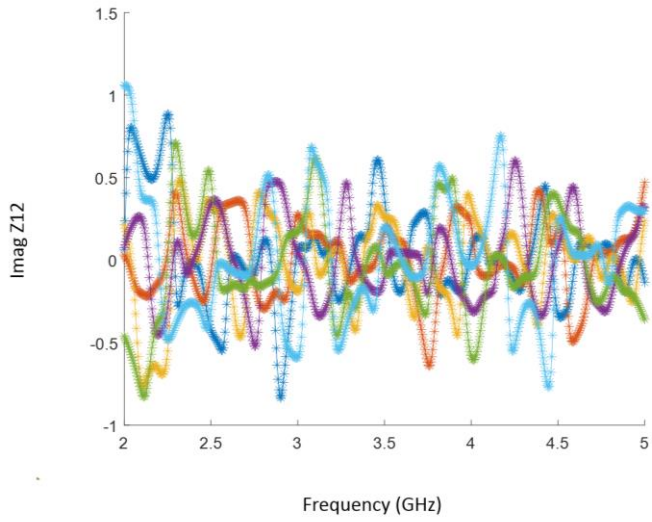
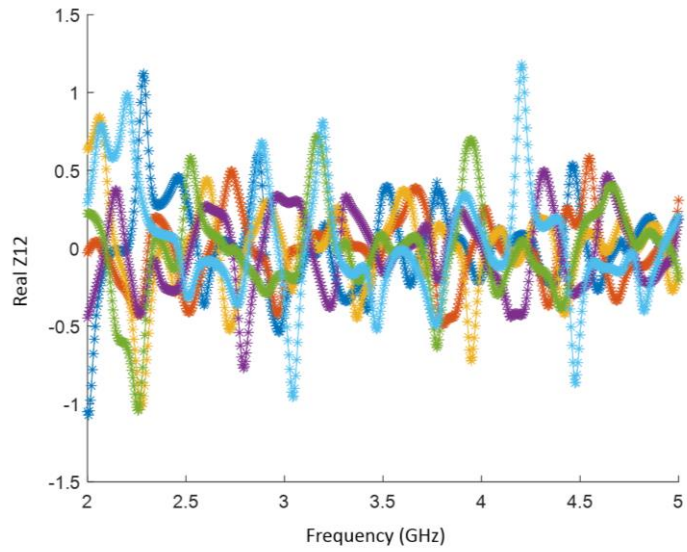


Fig. 5.3: Top to bottom: real and imaginary parts of various components of the Z matrix vs frequency for aperture-like ports. Different colors represent different scatterer positions as described in Table 5.1. These results are normalized.

As can be seen from Fig. 5.2-5.3, different scatterer position produces graphs that are distinct. This is not expected for a chaotic cavity such as the bowtie with a scatterer. If

the cavity is truly ergodic, different scatterer positions should show very similar results for  $Z_{nm}$  vs frequency. In order to show that the graphs would look more similar for different scatterer positions, we repeat the same simulation but this time use two co-axial cables as the sources instead of apertures. These results are shown in Fig. 5.4-5.5 where the co-axial cable dimensions are same as the ones discussed in Chapter 4, Section A. The walls of the bowtie had a resistance of 80 Ohms while the scatterer was perfectly reflective.

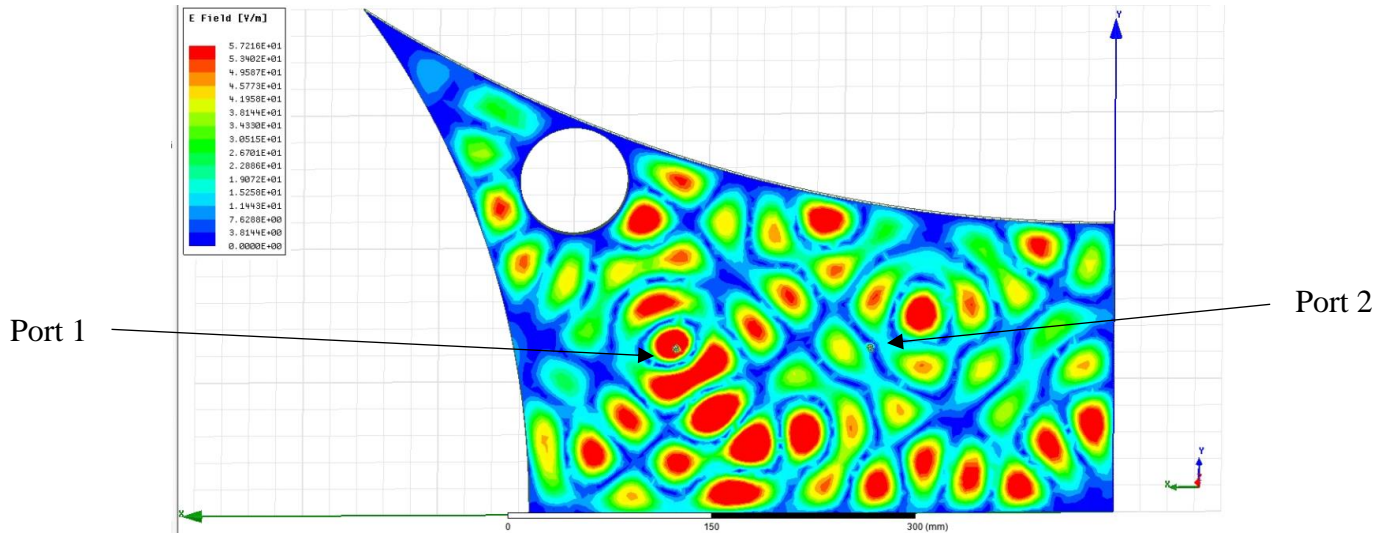


Fig. 5.4: Sample E-field for the co-axial cable sources for the first scatterer position where the source injects an EM wave at 5 GHz.

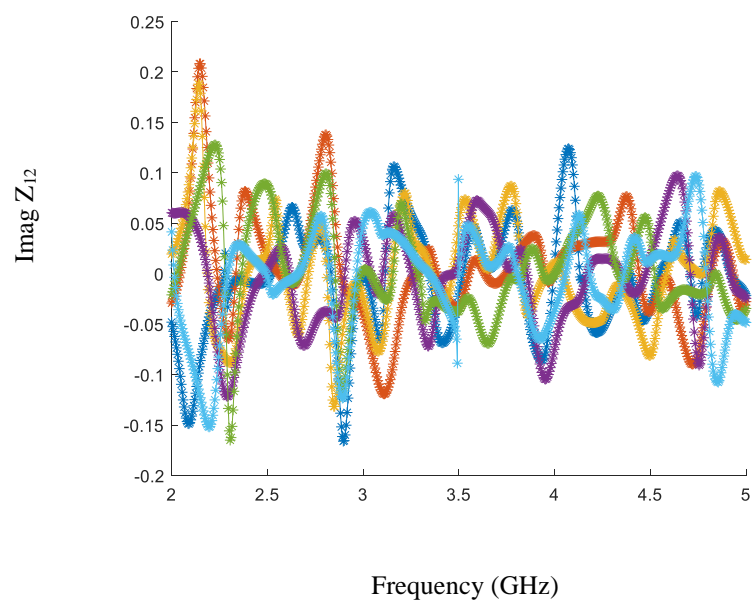
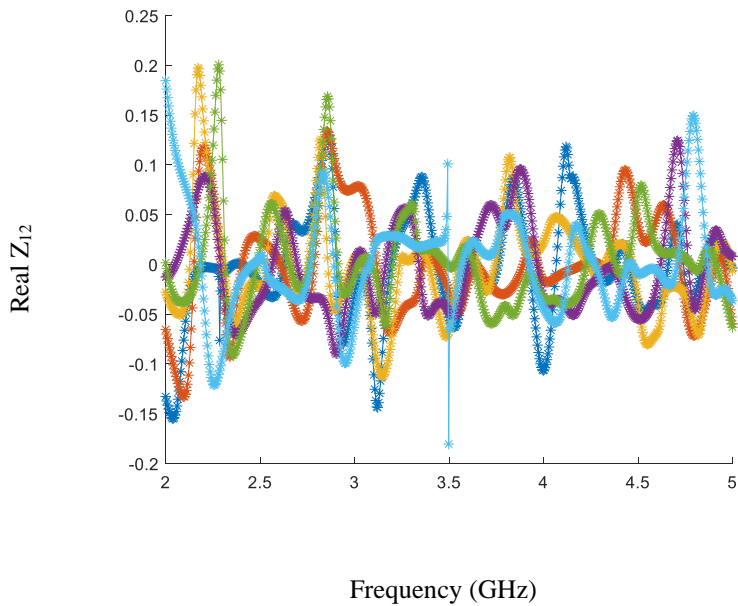
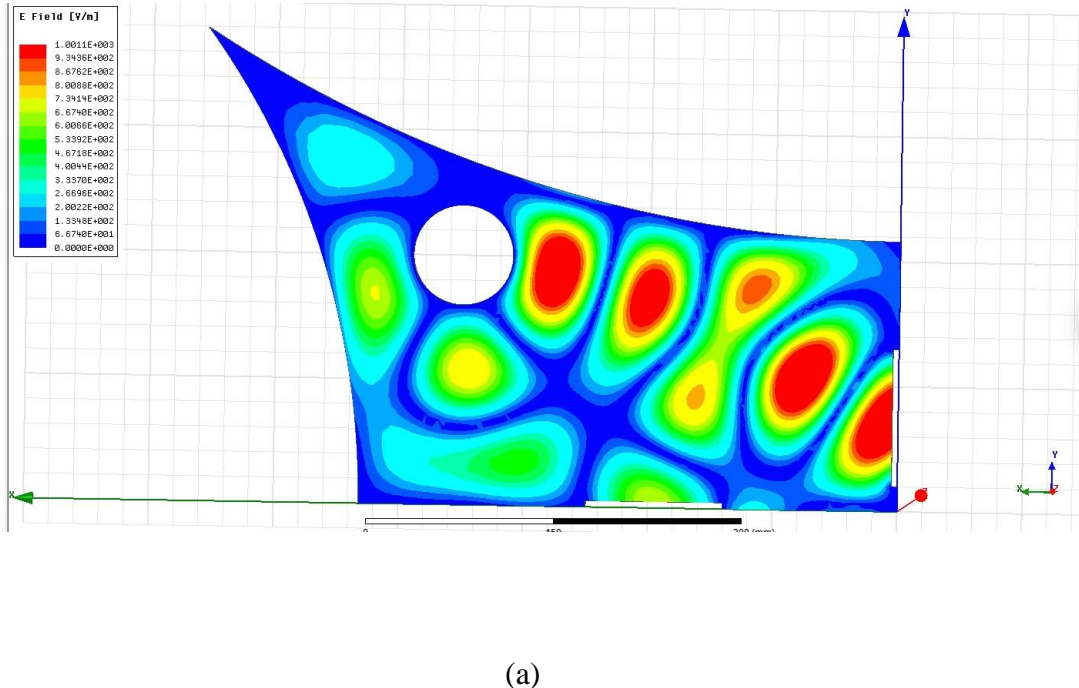
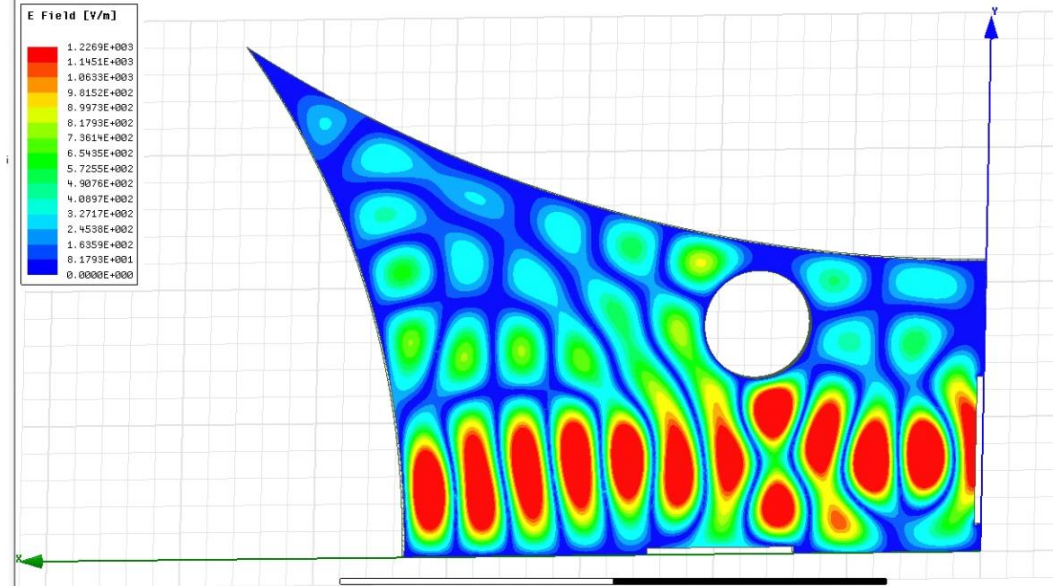


Fig. 5.5: Top to bottom: real and imaginary parts of various components of the  $Z$  matrix vs frequency for co-axial ports. Different colors represent different scatterer positions as described in Table 5.1. These results are normalized.

To investigate this non-ergodic behavior for the aperture like sources, we excite the source port exactly at the lowest (most negative) points of  $\text{Re}(Z_{12})$  graphs from Fig. 5.3 at 2.27 GHz (for the orange curve i.e. position 3). The resulting field patterns are shown in Fig. 5.6 (a). This picture clearly shows a short orbit forming between the launch port and the scatterer. We regularly find these short orbits at some of the other peaks of the  $\text{Re}(Z_{12})$  curves. Fig. 5.4(b) shows another scatterer position (position 5, cyan) where we excited the E-field at 4.204 GHz and found another strong short orbit.





(b)

Fig. 5.6: Figures showing different scatterer positions and the corresponding E-fields which exhibit short orbits forming. This is caused by the highly directive nature of the energy launch from the aperture-like ports. In (a) and (b) the source ports were excited at 2.27 GHz and 4.204 GHz, respectively.

We also present histogram plots of the  $\text{Re}(Z_{12})$  for various scatterer positions in Fig. 5.7. We see that different scatterer positions show different histogram plots. This is not expected for a wave chaotic cavity. In contrast, we present histogram plots of  $\text{Re}(Z_{12})$  for various scatterer positions in Fig. 5.8 for a co-axial source. What can be seen in this figure is that different scatterer positions produce histogram plots very similar to the ensemble.

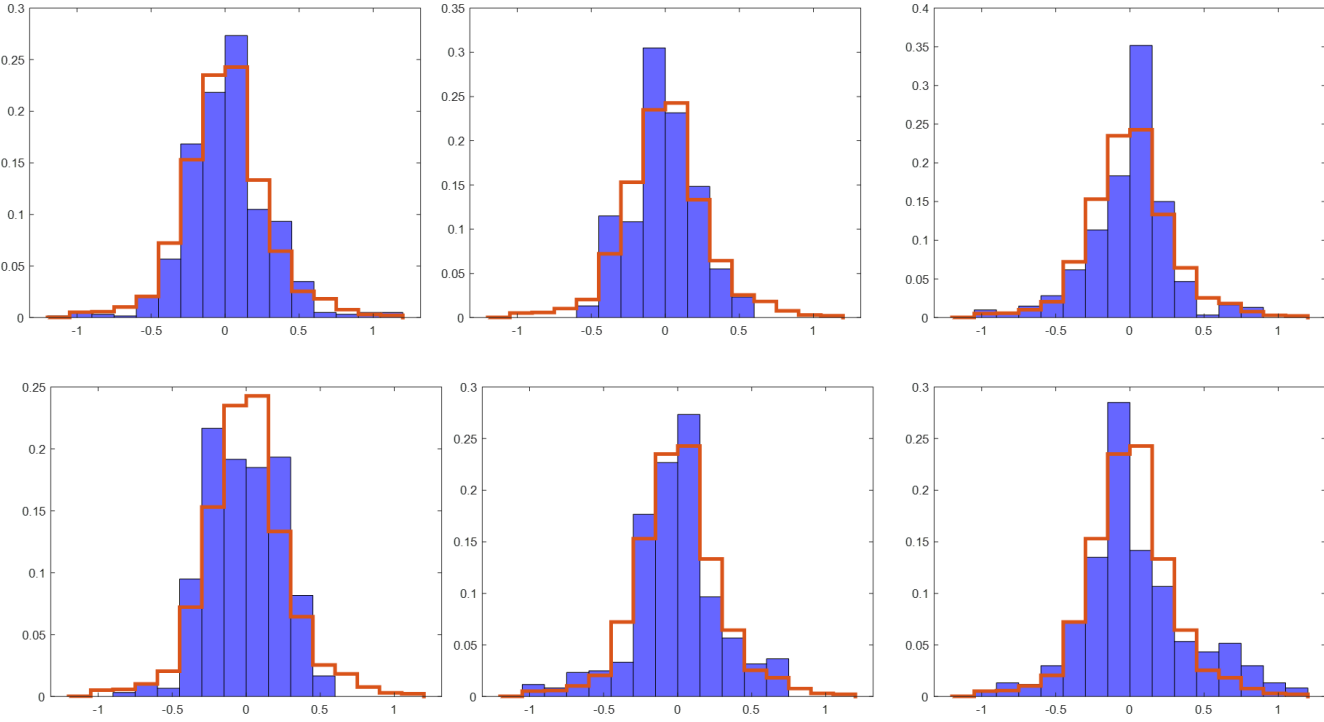


Fig. 5.7: Histogram plots for the normalized Z12 values for six different scatterer positions. These histograms are for the aperture-like sources for 2-5 GHz. Blue bars show the real parts of Z12 for a particular position. The red staircase graph shows the histogram for the real values for all six scatterer positions combined. This red graph is used to show if different scatterer positions are producing graphs that are different from the ensemble. From left to right on the top row scatterer position 1-3 are shown. From left to right on the bottom row scatterer position 4-6 are shown.

Drawing comparisons between Fig. 5.7 and 5.8, we can see that the co-axial cable histograms are always more similar to the ensemble. But the histograms for the aperture-like ports are not. However, these histogram comparisons do not show clearly that a particular scattering position can be very different from the ensemble for the aperture source case. So, to investigate even more directivity of the beam, we increased the excitation frequency and found much clearer answers.

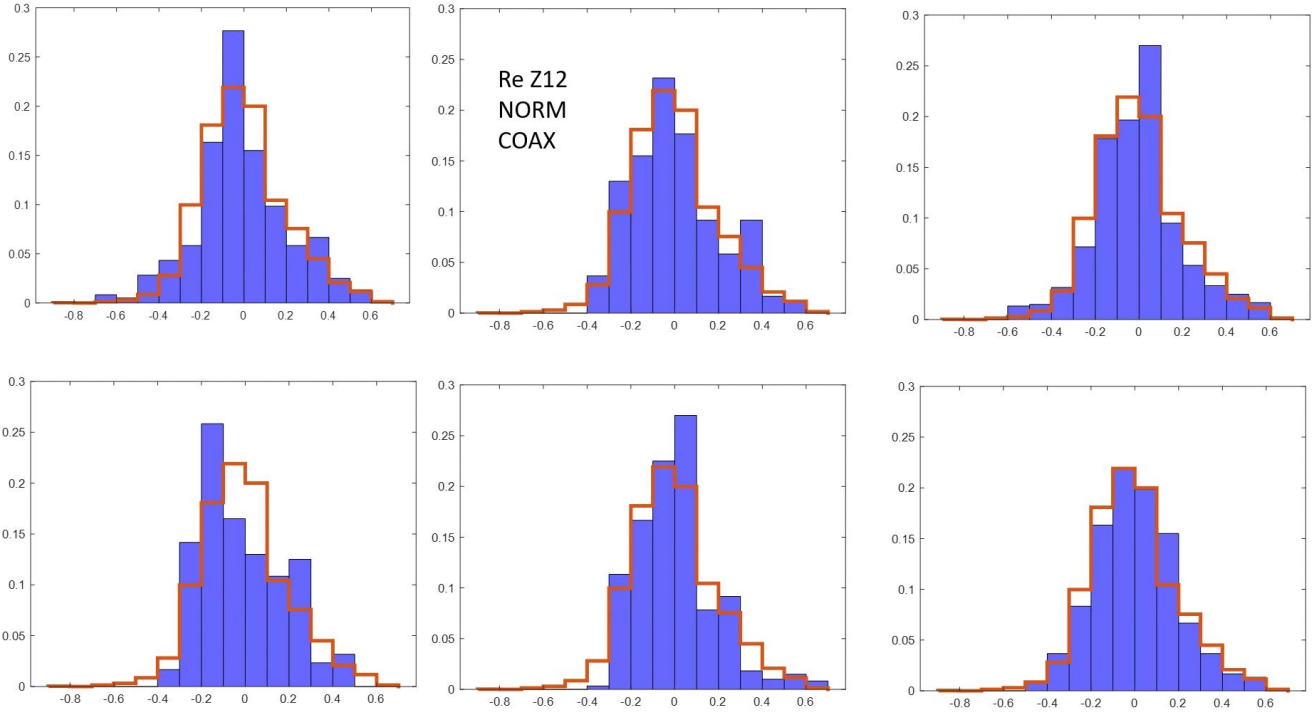


Fig. 5.8: Histogram plots for the normalized  $Z_{12}$  values for six different scatterer positions. These histograms are for the co-axial sources for 2-5 GHz. Blue bars show the real parts of  $Z_{12}$  for a particular position. The red staircase graph shows the histogram for the real values for all six scatterer positions combined. This red graph is used to show if different scatterer positions are producing graphs that are different from the ensemble. From left to right on the top row scatterer position 1-3 are shown. From left to right on the bottom row scatterer position 4-6 are shown.

We excited the source for 25 GHz and used both aperture-like and co-axial sources. This is shown in Fig. 5.9 where the E-field patterns suggest much more directivity of the source.

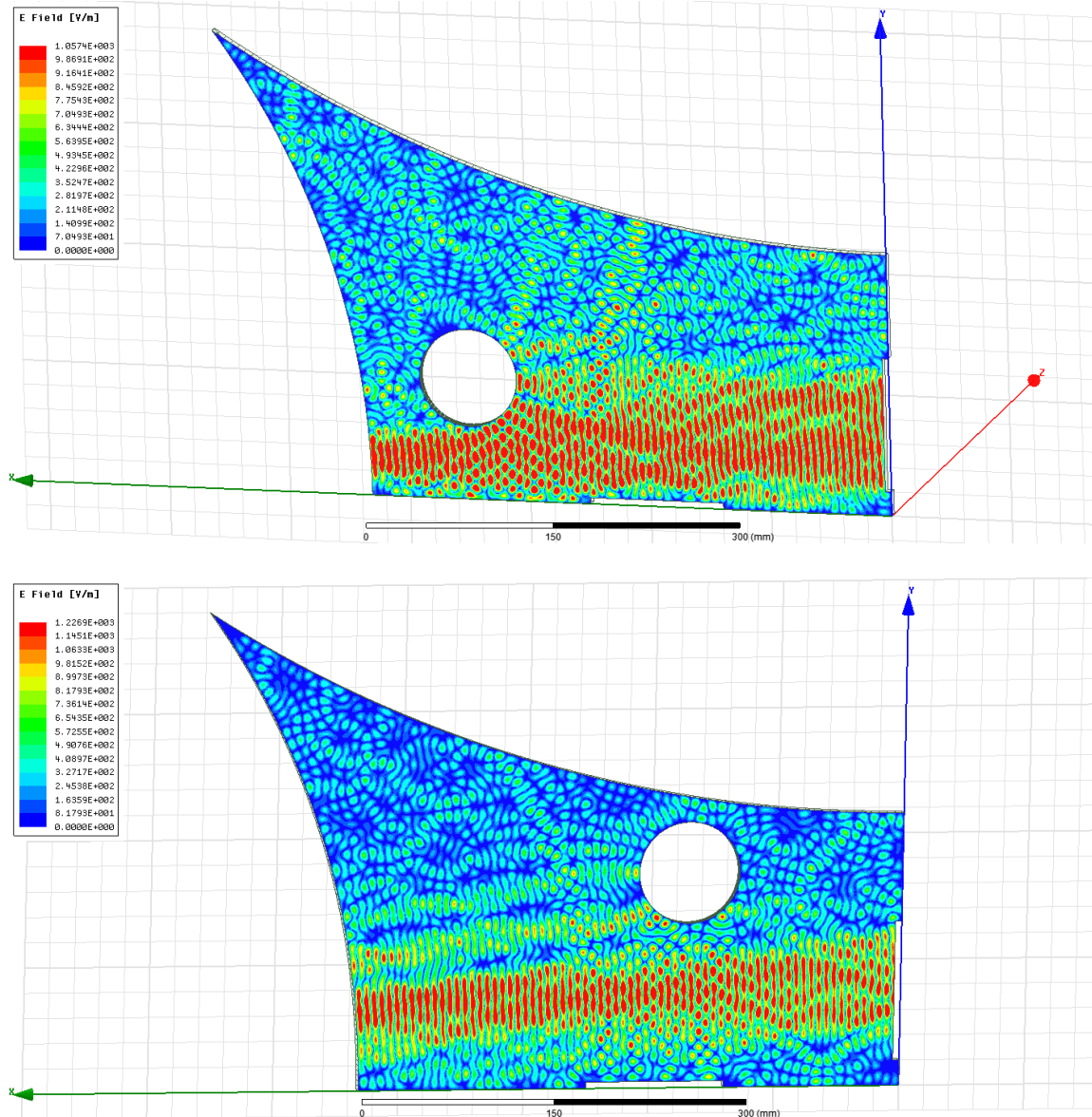


Fig. 5.9: View of the E-field in a quasi 2D bowtie cavity with a circular scatterer in different positions at 25 GHz for aperture-like ports. The walls had a loss of 80 Ohms while the scatterer is perfectly reflective. At this frequency, the beam is more directive than at 5 GHz and the short orbits are forming.

We also present the various Z components vs frequency plots for 24-26 GHz for the conditions of Fig. 5.9 in the next figure.

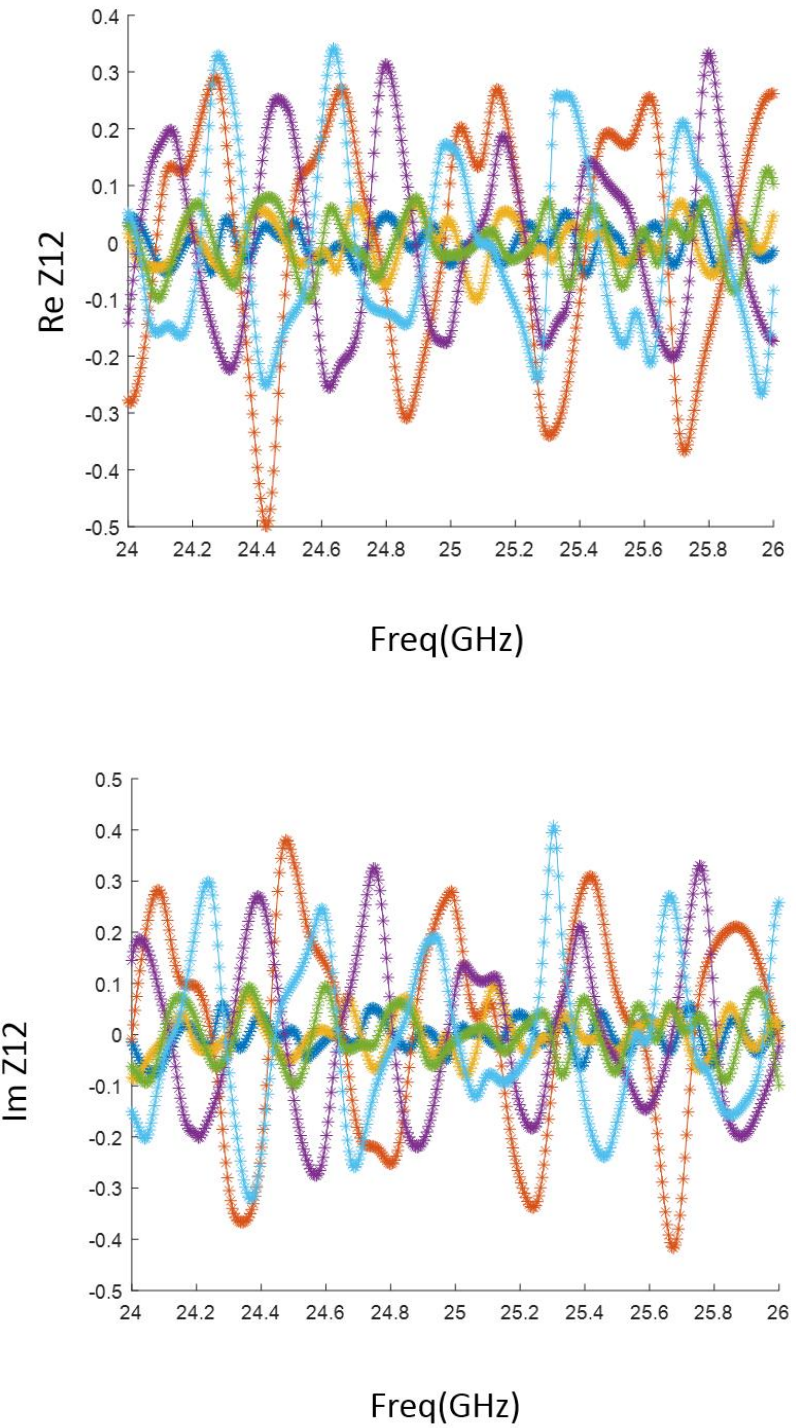


Fig. 5.10: Top and bottom: real and imaginary parts of various components of the Z matrix vs frequency for aperture-like ports. Different colors represent different scatterer positions as described in Table 5.1. These results are normalized.

In Fig. 5.10, it is even more evident that the scatterer position has a profound impact on the impedance values for the bowtie. We also present histogram plots of the  $\text{Re}(Z_{12})$  for various scatterer positions in Fig. 5.11. Here it is clearly shown that different scatterer positions show very different results. This was expected from the E-field plots where the beam was more directive than before.

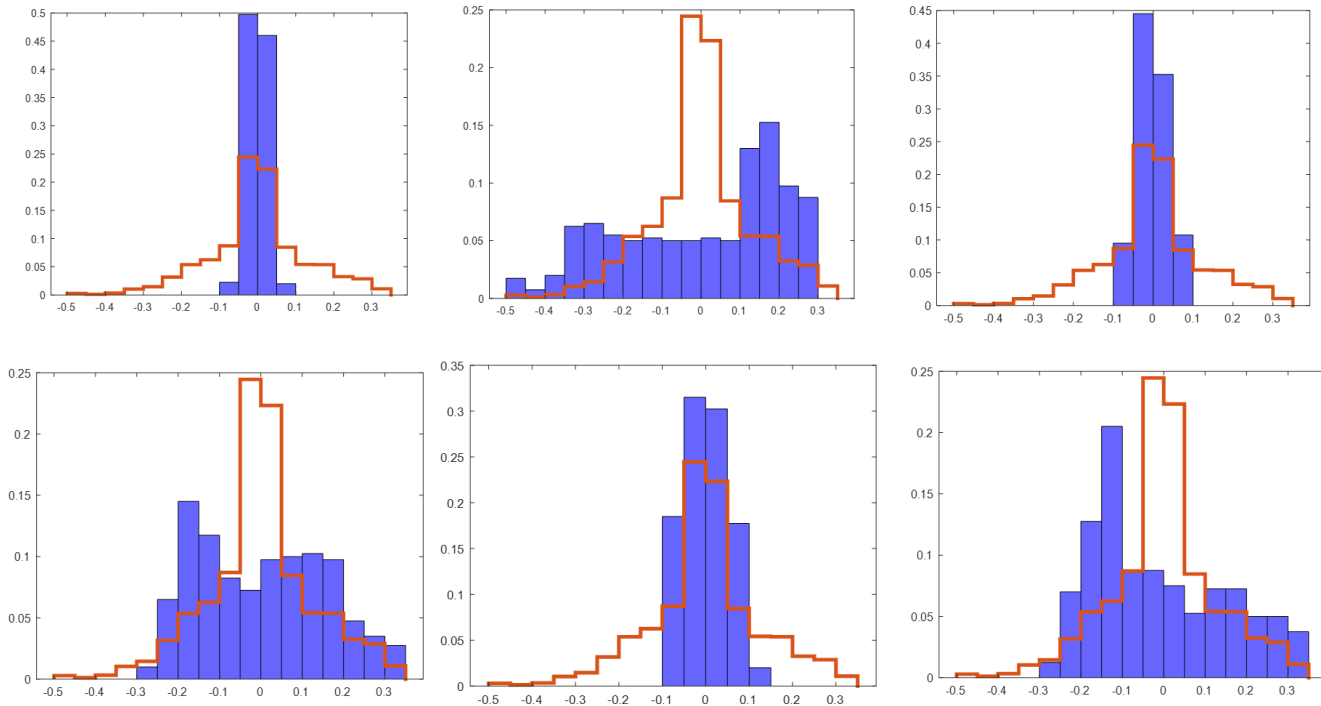


Fig. 5.11: Histogram plots for the normalized  $Z_{12}$  values for six different scatterer positions. These histograms are for the aperture-like sources for 24-26 GHz. Blue bars show the real parts of  $Z_{12}$  for a particular position. The red staircase graph shows the histogram for the real values for all six scatterer positions combined. This red graph is used to show if different scatterer positions are producing graphs that are different from the ensemble. From left to right on the top row scatterer position 1-3 are shown. From left to right on the bottom row scatterer position 4-6 are shown.

In contrast, we do the same experiments but with a co-axial cable at 25 GHz. These results are shown in Fig. 5.12-5.14.

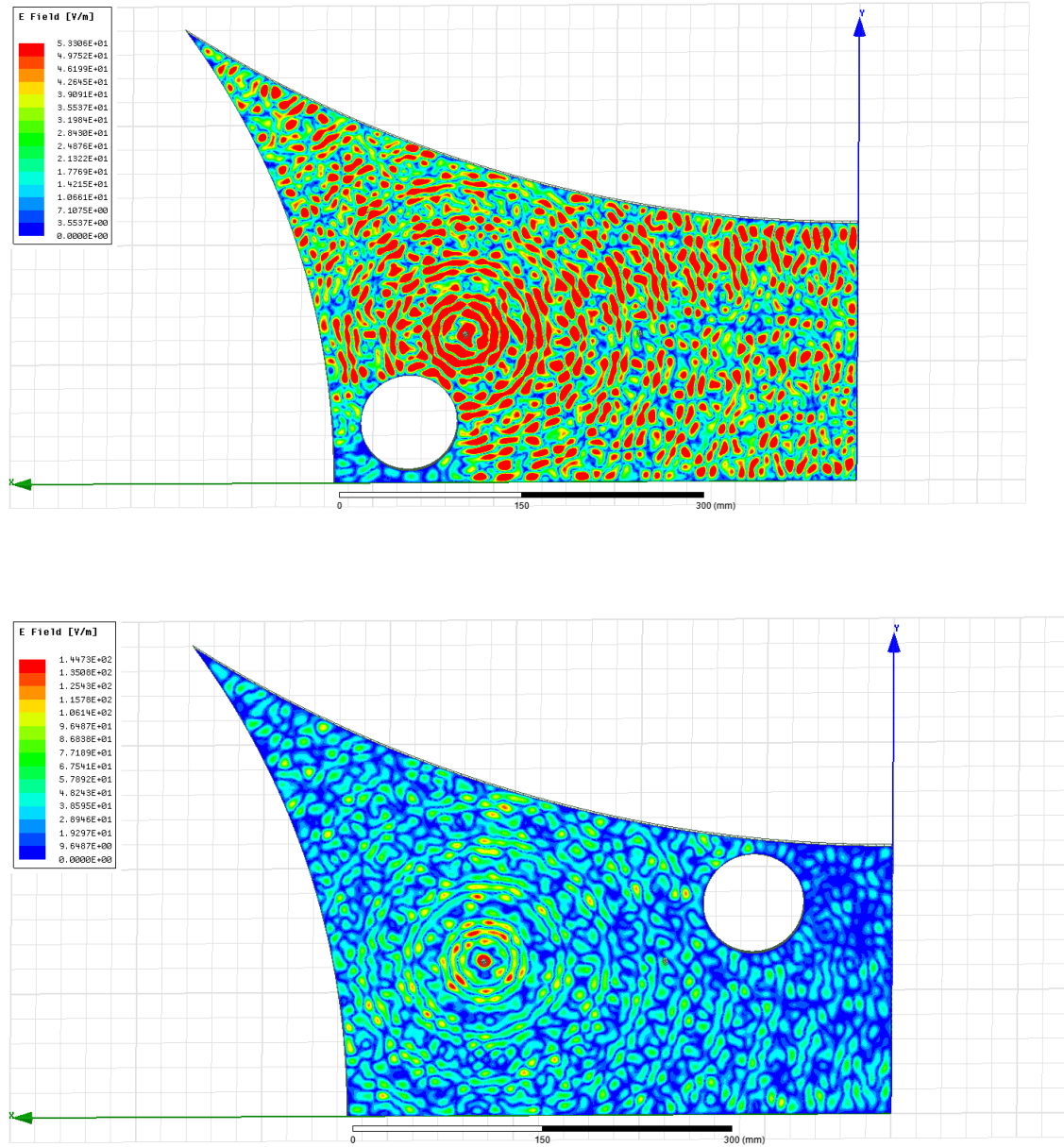


Fig. 5.12: View of the E-field in a quasi 2D bowtie cavity with a circular scatterer in different positions at 25 GHz for co-axial ports. The walls had a loss of 80 Ohms while the scatterer is perfectly reflective.

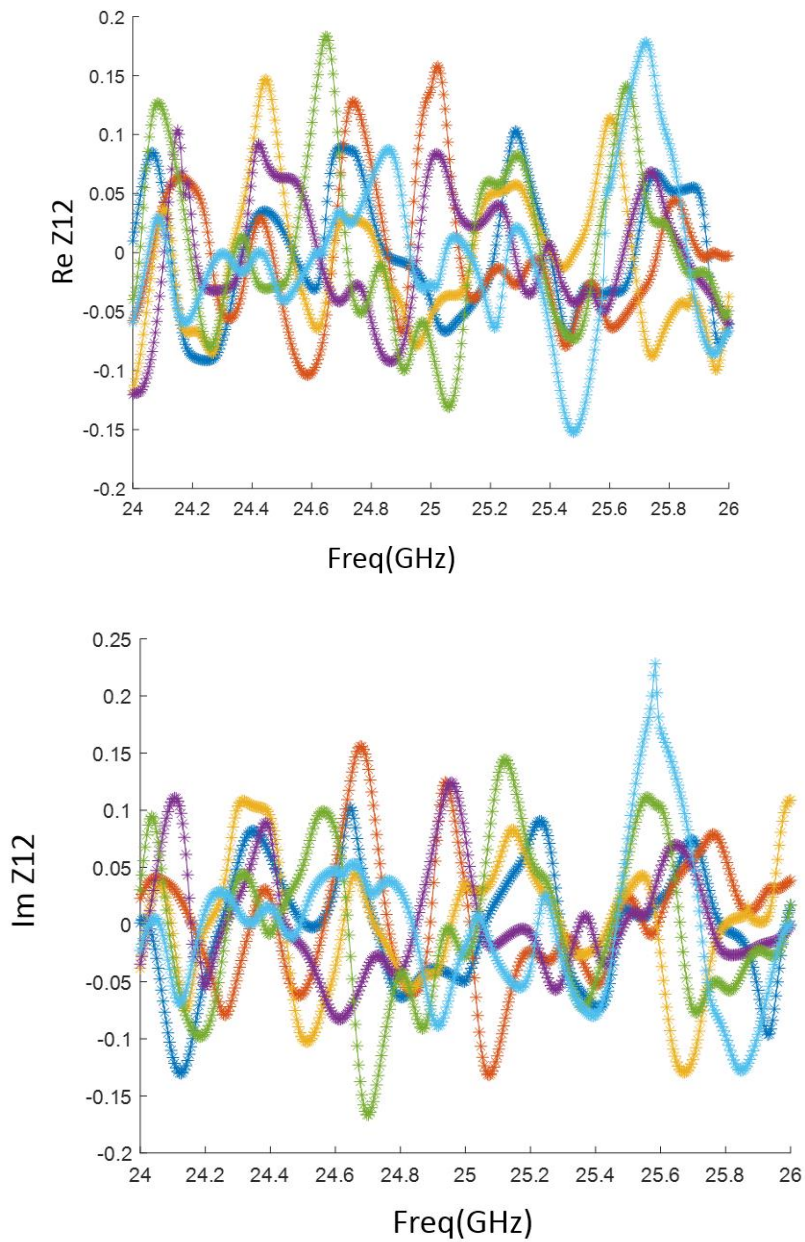


Fig. 5.13: Real and imaginary part of  $Z_{12}$  vs frequency for co-axial sources. Different colors show different scatterer positions.

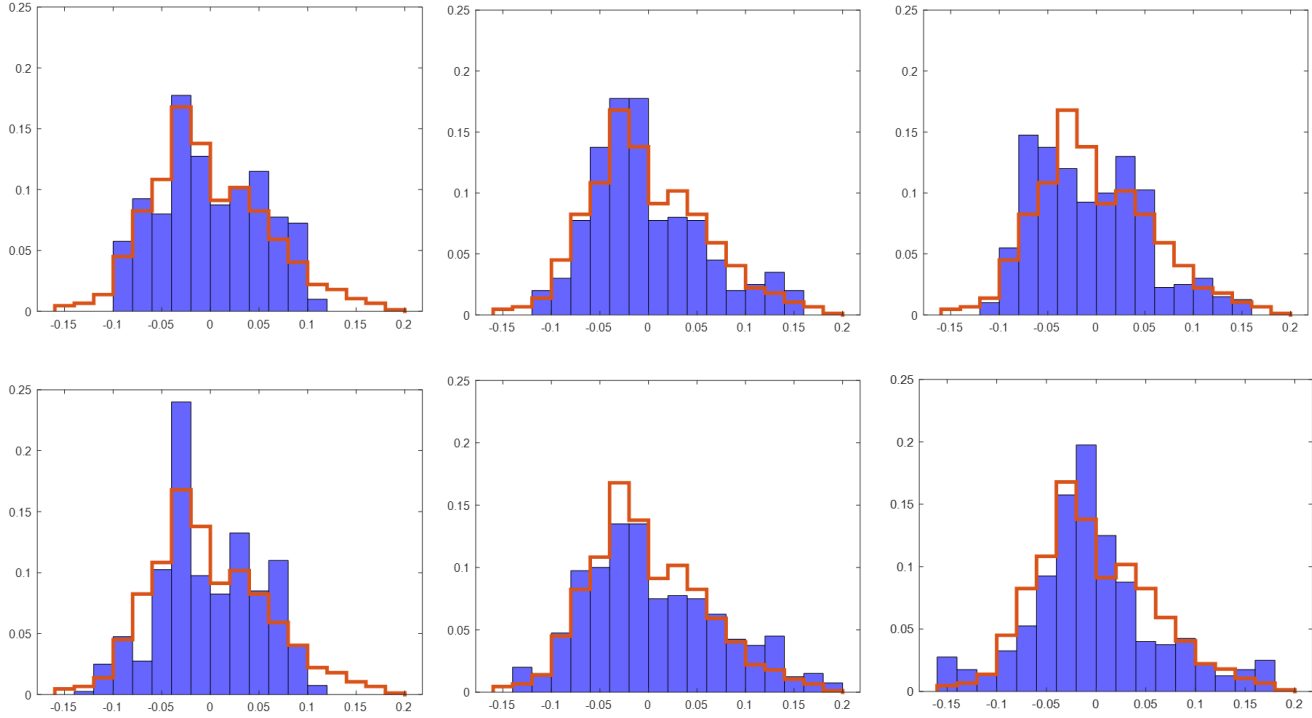


Fig. 5.14: Histogram plots for the normalized Z12 values for six different scatterer positions. These histograms are for the co-axial sources for 24-26 GHz. Blue bars show the real parts of Z12 for a particular position. The red staircase graph shows the histogram for the real values for all six scatterer positions combined. This red graph is used to show if different scatterer positions are producing graphs that are different from the ensemble. From left to right on the top row scatterer position 1-3 are shown. From left to right on the bottom row scatterer position 4-6 are shown.

We also investigated lower wall losses as opposed to only 80 Ohms. We did this because the E-field plots suggest at 25 GHz the loss might be too high and the waves might get absorbed quickly (i.e. within a few bounces) by the walls. So, we did the simulations at 40 Ohms and 10 Ohms losses in the walls. The scatterer was kept fully reflective. We present these results in Fig. 5.15-5.17.

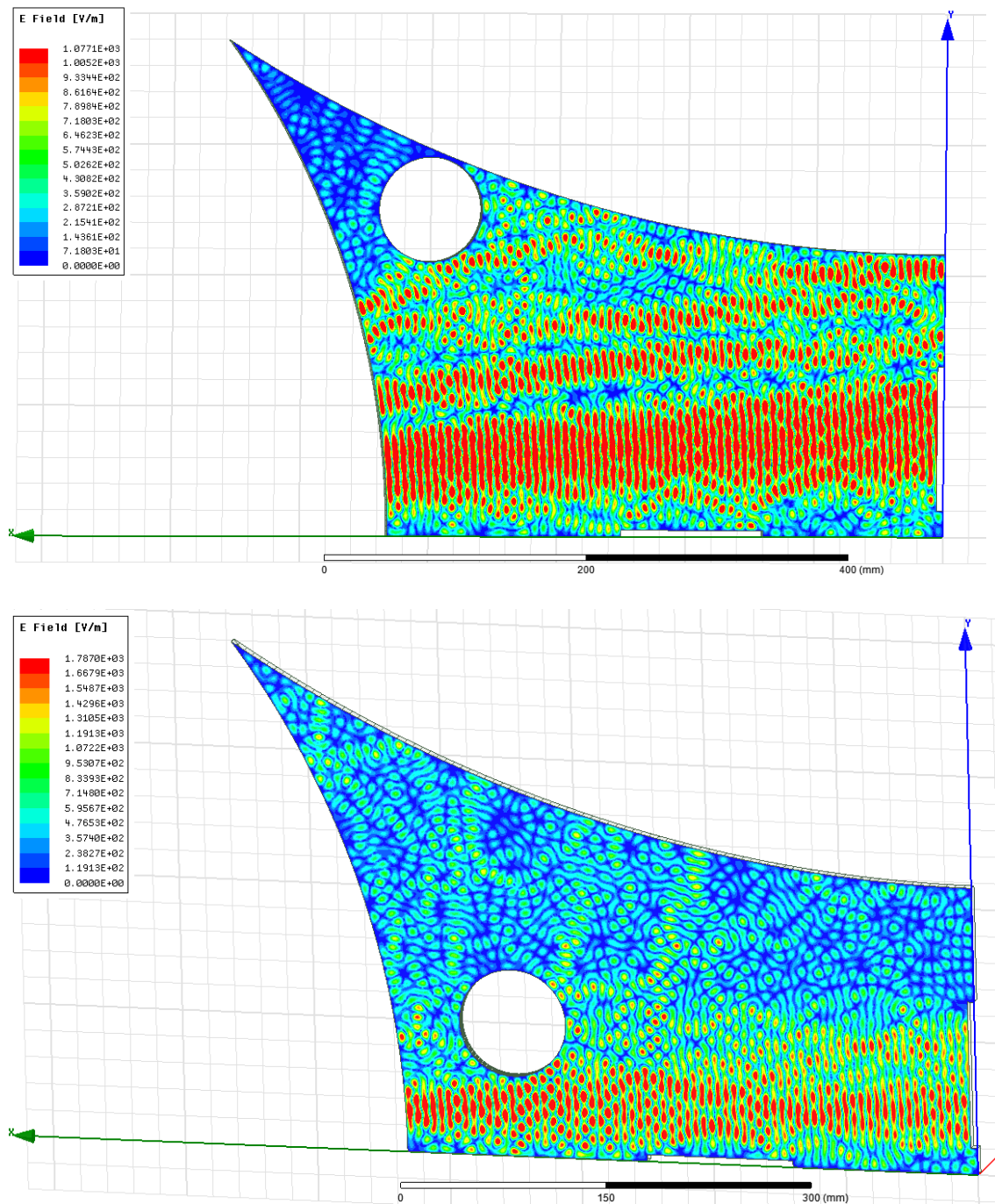


Fig. 5.15: View of the E-field in a quasi 2D bowtie cavity with a circular scatterer in different positions at 25 GHz for aperture-like ports. The walls had a loss of 40 Ohms while the scatterer is perfectly reflective.

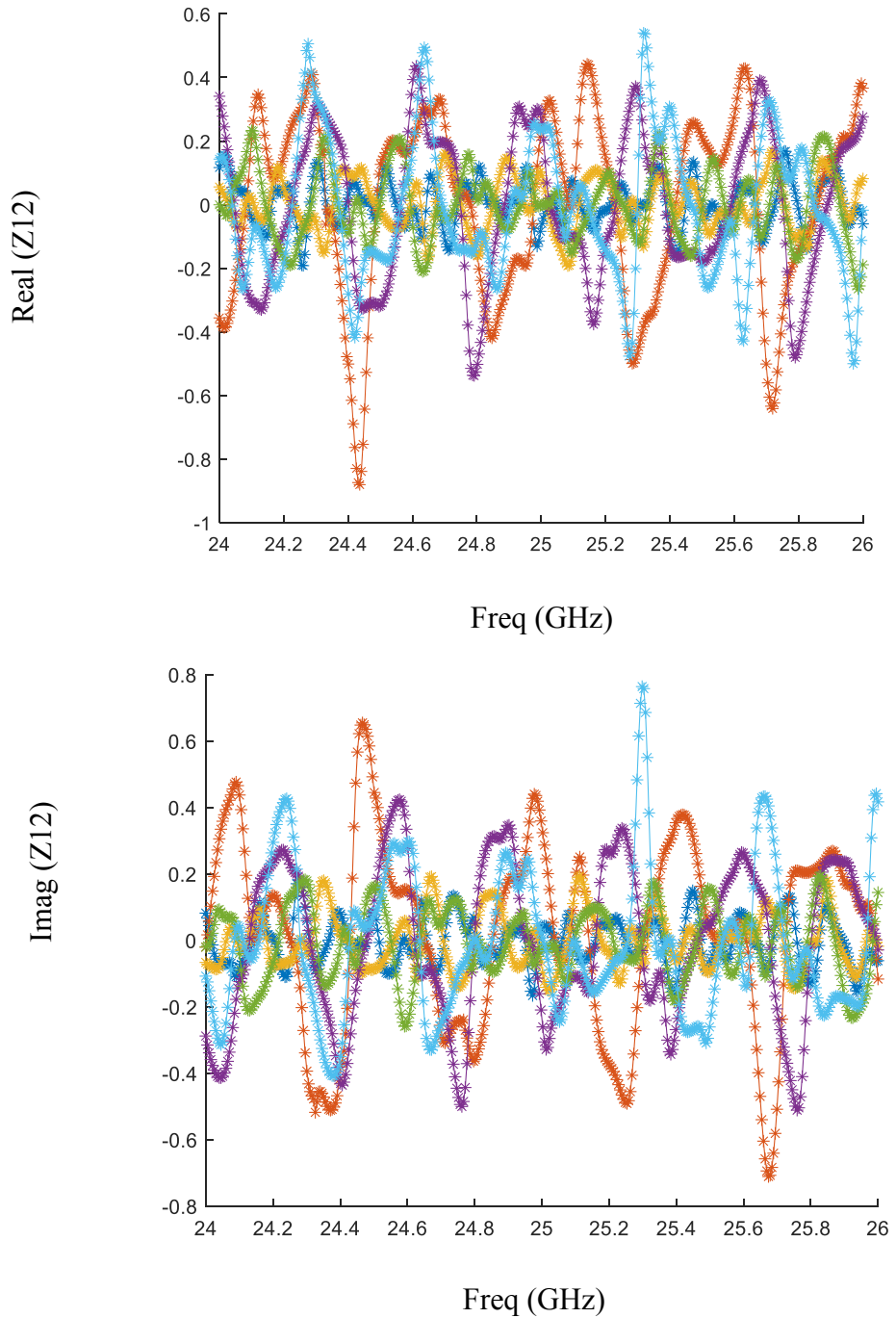


Fig. 5.16: Real and imaginary part of  $Z_{12}$  vs frequency for aperture-like sources. Different colors show different scatterer positions. These results are for 40 Ohms wall loss.

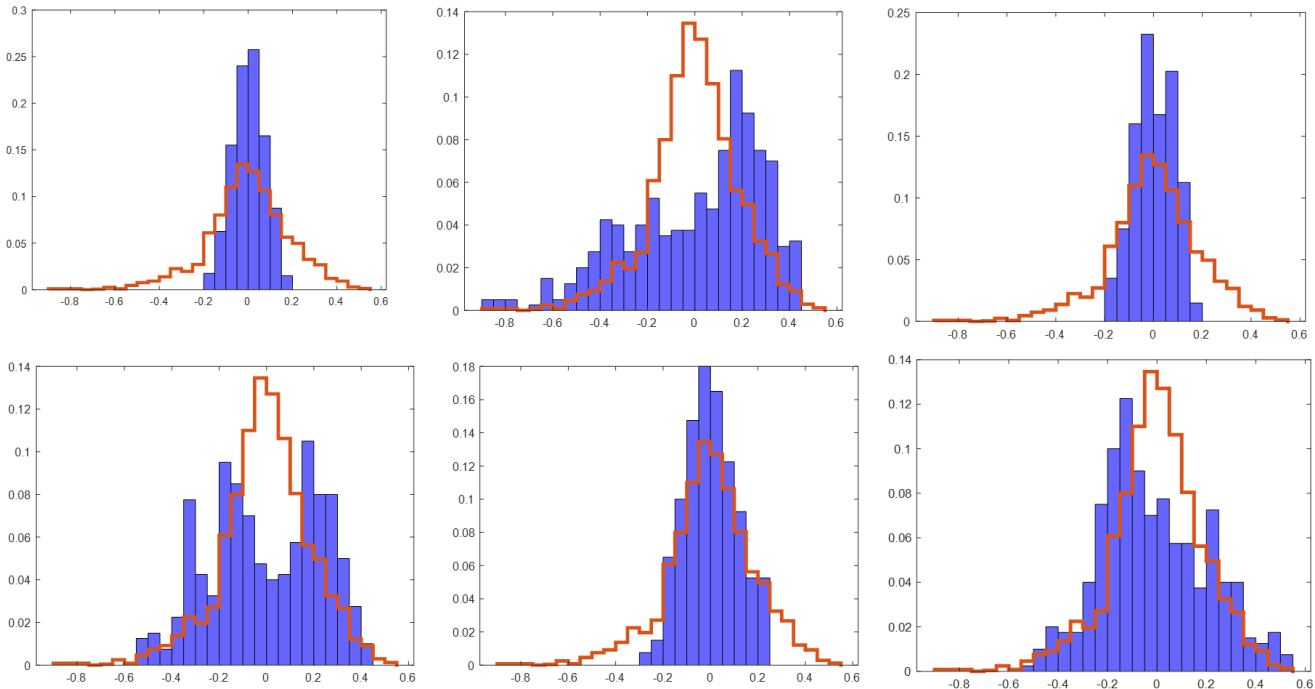


Fig. 5.17: Histogram plots for the normalized Z12 values for six different scatterer positions. These histograms are for the aperture-like sources for 24-26 GHz. Blue bars show the real parts of Z12 for a particular position. The red staircase graph shows the histogram for the real values for all six scatterer positions combined. This red graph is used to show if different scatterer positions are producing graphs that are different from the ensemble. From left to right on the top row scatterer position 1-3 are shown. From left to right on the bottom row scatterer position 4-6 are shown. These results are for 40 Ohms wall loss.

What can be seen by Figs. 5.15-5.17 is that the lower loss has made the Z plots much more noisy but the shapes for different colours are the same. In Figs. 5.18-5.20 we show the results for the 10 Ohms loss.

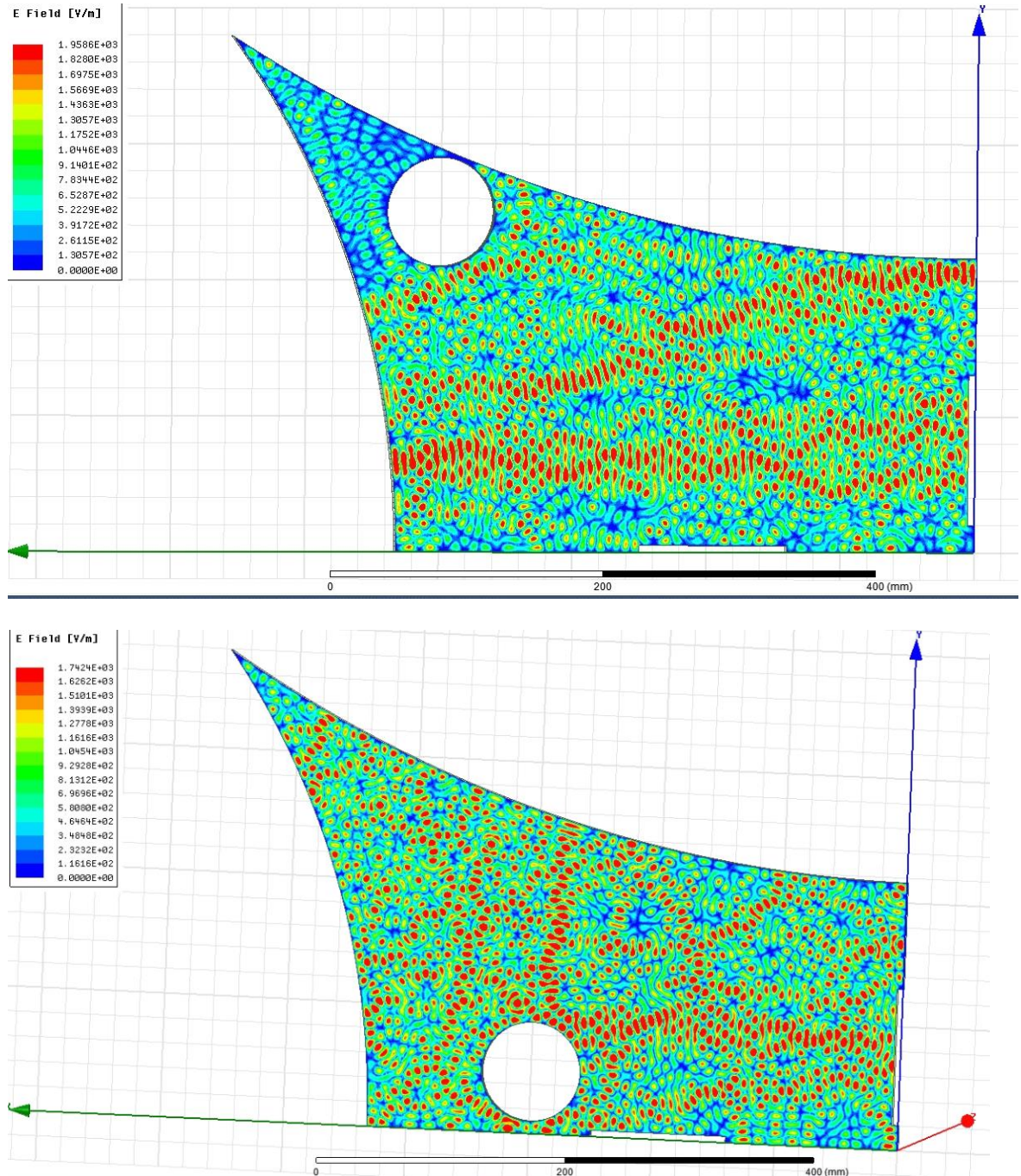


Fig. 5.18: View of the E-field in a quasi 2D bowtie cavity with a circular scatterer in different positions at 25 GHz for aperture-like ports. The walls had a loss of 10 Ohms while the scatterer is perfectly reflective.

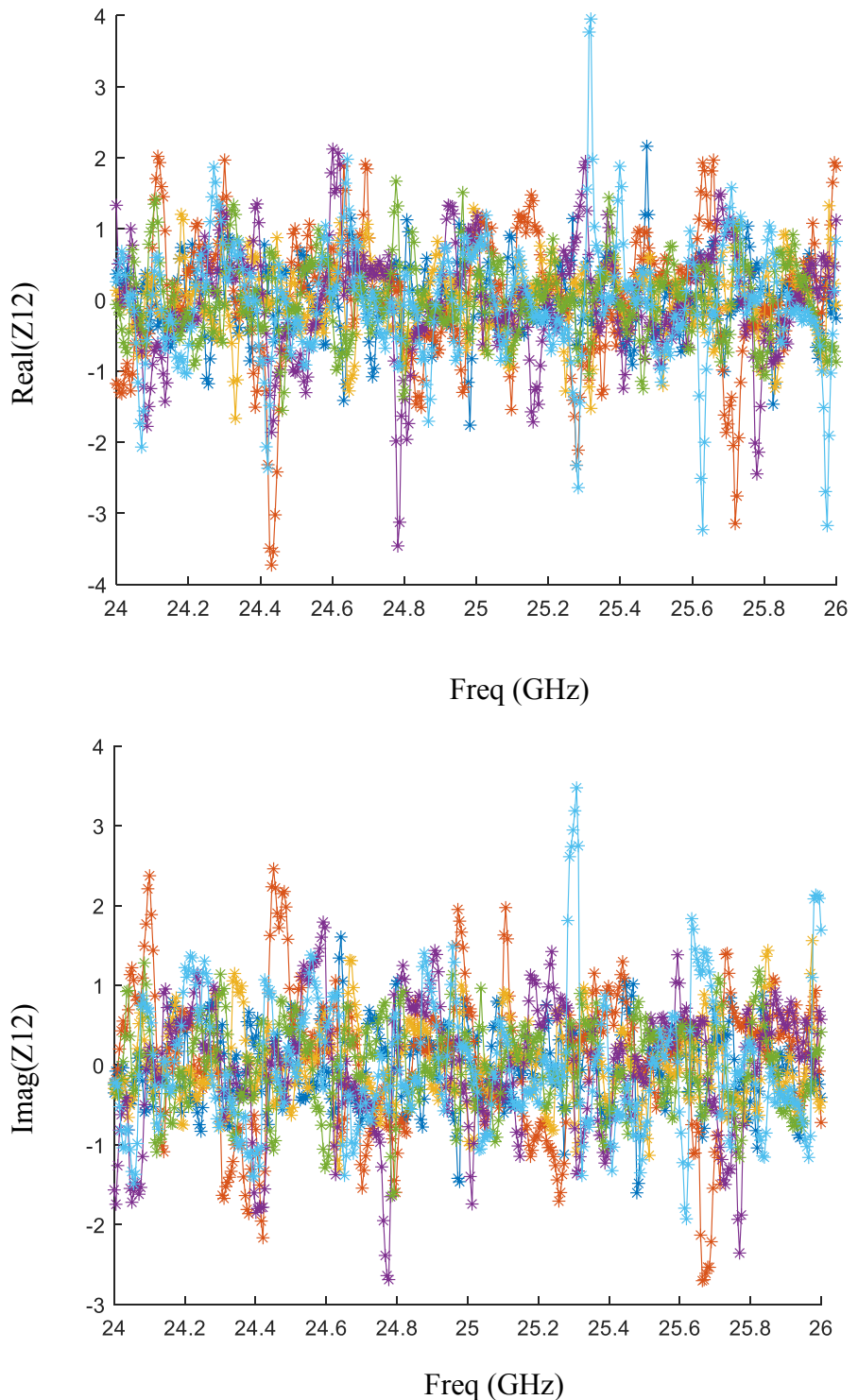


Fig. 5.19: Real and imaginary part of  $Z_{12}$  vs frequency for aperture-like sources. Different colors show different scatterer positions. These results are for 10 Ohms wall loss.

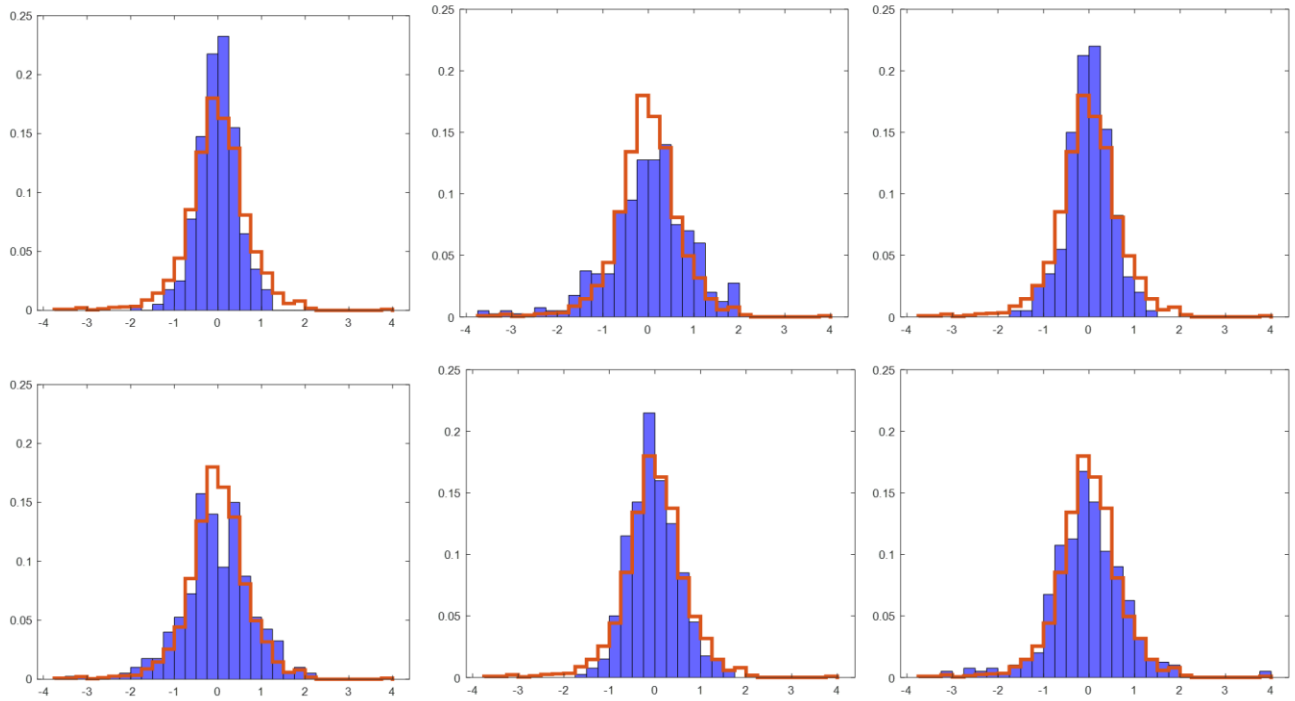
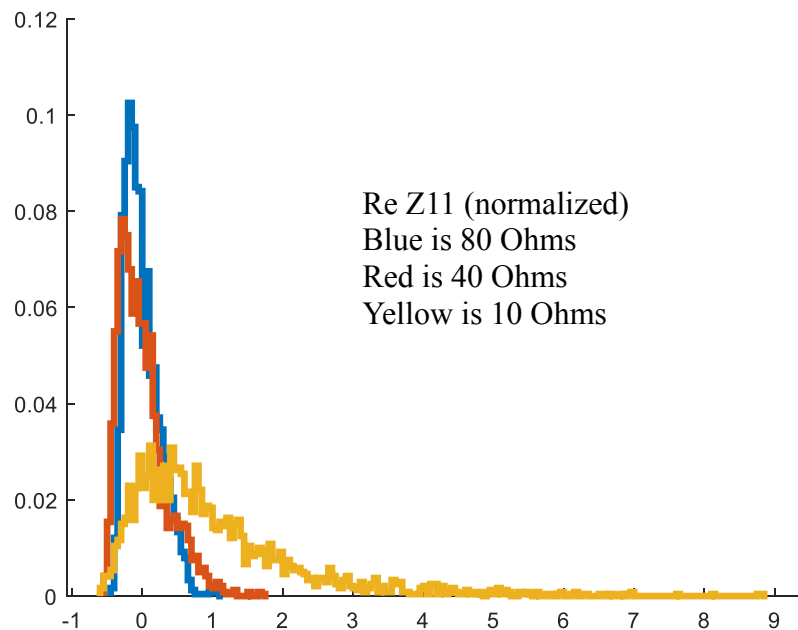
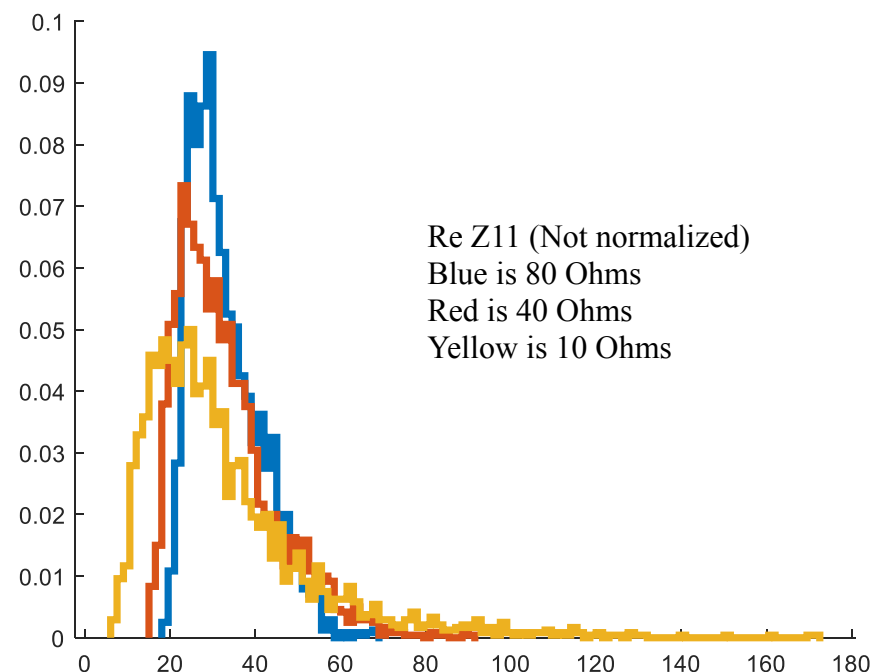


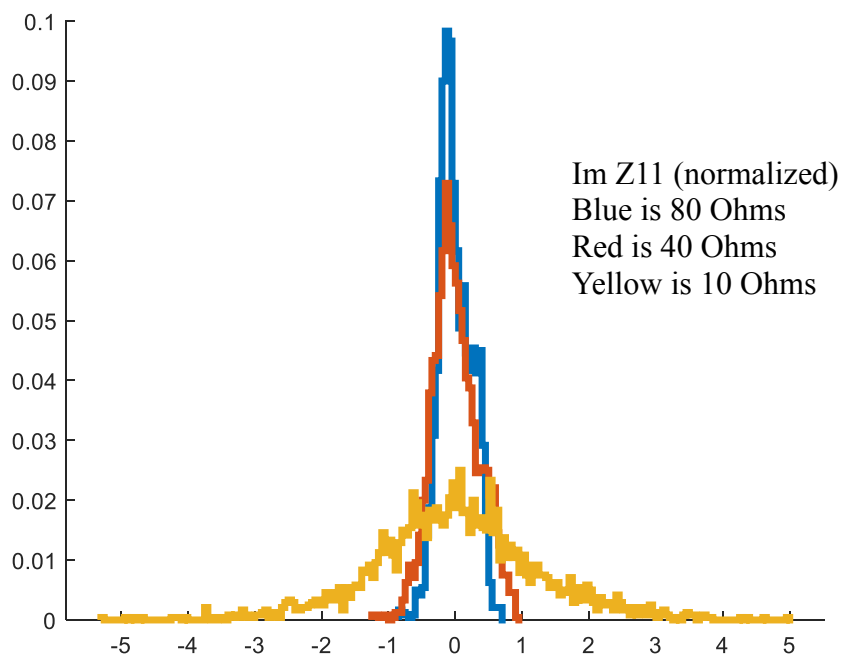
Fig. 5.20: Histogram plots for the normalized Z12 values for six different scatterer positions. These histograms are for the aperture-like sources for 24-26 GHz. Blue bars show the real parts of Z12 for a particular position. The red staircase graph shows the histogram for the real values for all six scatterer positions combined. This red graph is used to show if different scatterer positions are producing graphs that are different from the ensemble. From left to right on the top row scatterer position 1-3 are shown. From left to right on the bottom row scatterer position 4-6 are shown. These results are for 10 Ohms wall loss.

What can be observed by looking at the histograms in Fig. 5.20 is that at 10 Ohms wall loss, the blue bars are conforming much more to the ensemble as represented by the red staircase. This simply suggests that more ergodicity is achieved at lower losses and we have a situation where the RCM would be applicable. Furthermore, if we draw comparisons between the ensembles at 80, 40 and 10 Ohms loss for 24-26 GHz for the aperture-like ports, we get figures as shown in Fig. 5.21.

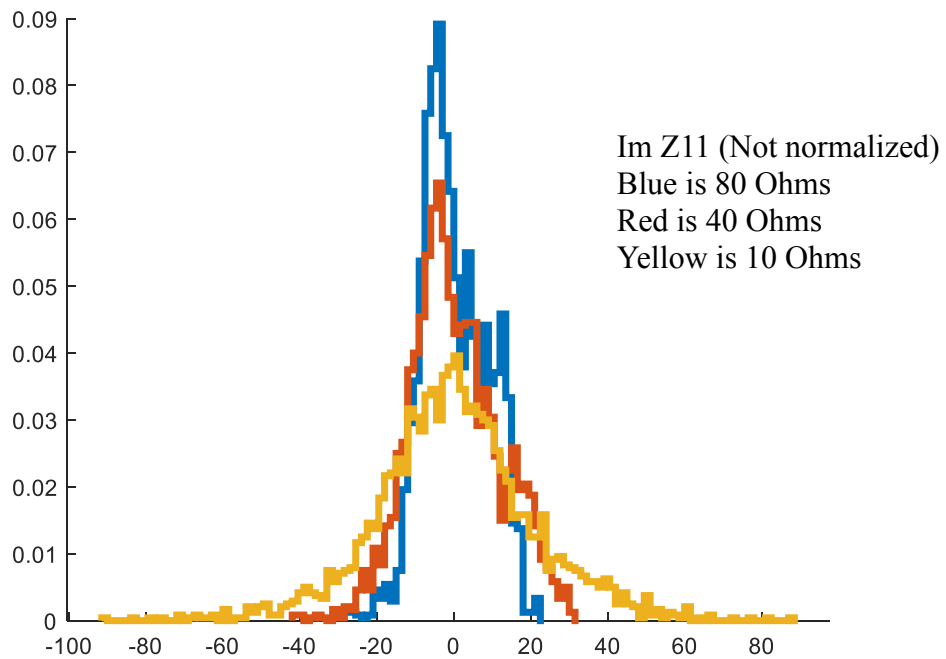


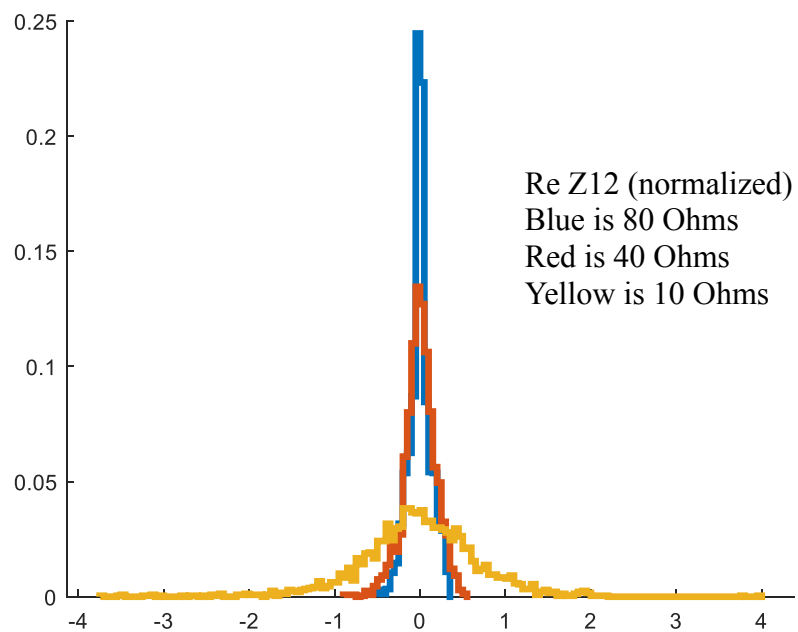
(a)



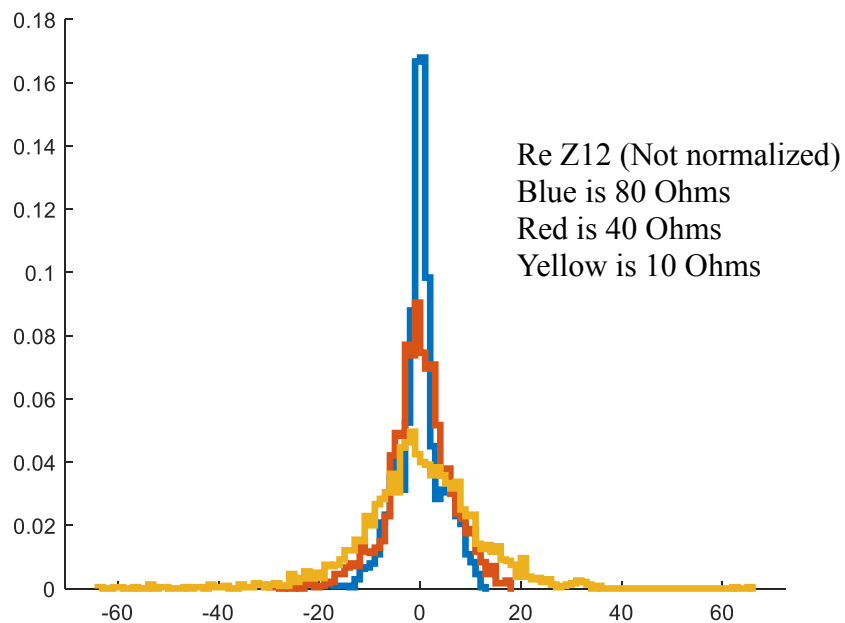


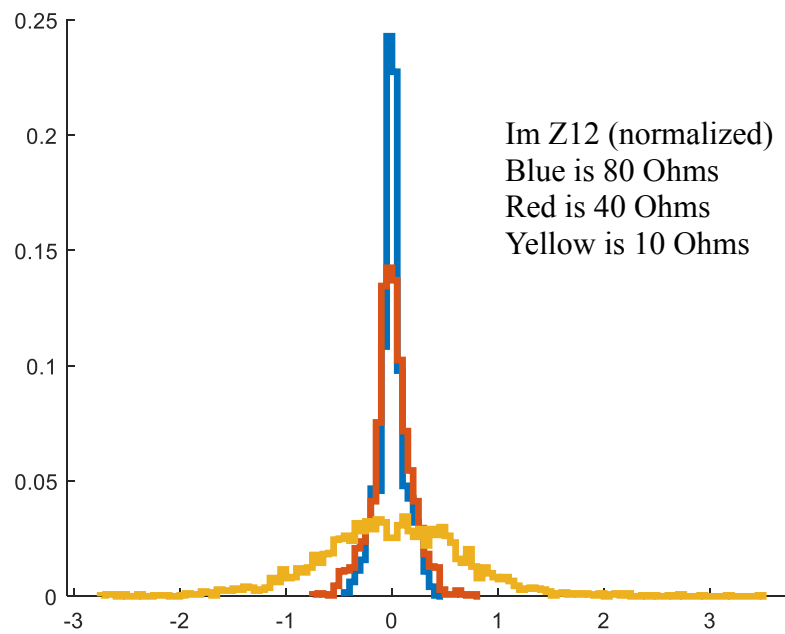
(b)





(c)





(d)

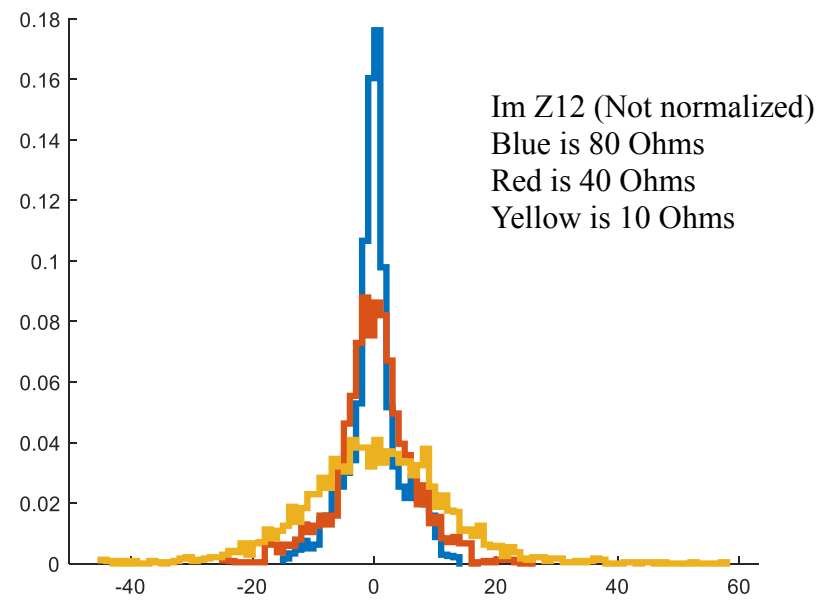


Fig. 5.21: Ensemble histograms of impedance for various losses for the aperture-like ports at 24-26 GHz.

These graphs shown in Fig. 5.21 is also expected. With higher losses the ensembles should have a narrower distribution.

In summary of this chapter, we have shown that with a directed beam, even in a purely chaotic cavity like the bowtie with a scatterer, we can have situations where the cavity is not truly ergodic and therefore the RCM predictions should not hold.

The observed impedance statistics depend in an involved way on a number of factors. These include the ratio of wavelength to cavity dimension, the amount of loss, and the directivity of the ports. Our studies compared two frequency ranges, two port types, and three loss values. In the 2 – 5 GHz frequency range the wavelength is roughly 10 cm. This is the size of the apertures, but significantly smaller than the size of the cavity. The directivity of the aperture ports is only moderate in this case. Here we observed marginal differences in the impedance statistics when comparing the coaxial ports with the aperture ports (Figs 5.7 and 5.8).

When the frequency is raised to 25 GHz more varied behavior was observed. At this frequency the aperture ports become significantly more directive. When the losses are high (80 Ohm surface resistance) large differences in the realization-to-realization distribution of impedance values are observed. In comparison, such differences are not observed with the coaxial ports. When losses are decreased the realization-to-realization differences seen with the directive ports go away. The interpretation is that with a directive port and high loss, the launched waves are absorbed before they sample

the entire phase space of the cavity. The sampling of phase space becomes more effective when either losses are decreased, or isotropic ports are used.

## Chapter 6: Conclusions and future work

### Conclusions

Wave scattering and coupling in a complicated geometry is a common challenge in many scientific fields because the complexity makes exact solutions impractical. On the other hand, wave chaos theories offer useful approaches to analyze the statistical properties of these complicated dynamical systems. In this thesis, we have studied two broad applications of wave chaos theories. Firstly, we have shown RT models that can successfully calculate the power delivery to an aperture of a 2D wave chaotic multi-cavity connected by an aperture. This method was also successfully compared with the DEA simulations conducted by the University of Nottingham group. Then the results generated by these two methods were compared with the established PWB method. From this comparison our broad conclusion is that both RT and DEA are equivalent and are alternate descriptions of one another- RT being the Lagrangian while DEA being the Eulerian description.

Secondly, we have conducted studies of short orbits which was introduced by previous researchers as a correction to the RCM. We have shown here using our RT code that the impedance calculations due to the SOF can be done by finding the short orbits directly after launching many rays from a point source. A single bowtie cavity was used for this study where two point sources were used to launch and receive rays and various boundary conditions were simulated. These results were then compared with full wave

solutions done on HFSS. What we find is that the SOF can give us similar results to the full wave solutions but there is a phase difference between the results of the two approaches. This phase difference we conclude is due to the RT code using a point source to model the port whereas the HFSS models the ports more accurately as two co-axial sources. This lack of port detail is what causes the two methods to produce results differing in phase.

Also, in continuation of the short orbit studies we conducted full wave solutions in HFSS of a bowtie cavity with a scatterer inside. But this time we used aperture-like ports launching EM energy in the cavity at 5 GHz. This was done to create a more directional beam which we expected to create deviations from the Random Plane Wave hypothesis- which is the basis of the RCM. We did find this to be true and we see various short orbits forming from the E-field graphs. Furthermore, with this directed beam we see that at higher frequencies (around 25 GHz) every scatterer position produces impedance vs frequency plots that are very different from other scatterer positions. This was further demonstrated using a histogram approach. This successfully shows that ergodicity is lost in this chaotic cavity due to the directive nature of this aperture-like port. But when we do the simulations for the co-axial (i.e. omnidirectional sources) we see that the position of the scatterer has little effect on the impedance vs frequency plots. This would lead to the random plane wave hypothesis being true and RCM would be applicable.

### Future Work

We have explored different wave chaotic systems in this thesis using various methods. It is interesting to ask what further comparisons can be made for our power delivery experiments.

First, we might compare the three approximate solutions to full wave solutions to find how the differences among the approximate solutions compare with the difference with the exact solution. Second, the current study is focused on 2D geometry. The issue of three dimensions and the added complication of field polarization should be addressed. Third, the comparisons between DEA and RT were limited to gross quantities. The DEA computes local wave energy density on a grid. Ray Tracing methods can also produce such a quantity. The most efficient way of doing this would be to adopt the particle in cell (PIC) methods of charged particle dynamics. This approach treats the motion of particles in the Lagrangian picture while accumulating on a grid the Eulerian change and current densities.

In the other part of the thesis for the short orbit studies, many different questions can be investigated. We can derive a more efficient model for the port that would allow us to remove the phase differences that were observed for the Z vs frequency plots. This can be done by taking into account the detailed port descriptions. We can also use the RT code and the SOF to study the time domain RCM. RCM so far has only been studied for the frequency domain calculations. But it would be very interesting to launch a

Gaussian pulse or a sine wave source in the point source of our RT code. That would lead to a description of RCM where a time varying response of the system excited at each time step can be accommodated.

The future generation of wave chaotic studies would investigate these questions in deeper detail.



## Bibliography

- [1] Xin Li, Cui Meng, Yinong Liu, Edl Schamiloglu, and Sameer D. Hemmady, Experimental verification of a stochastic topology approach for high-power microwave effects, *IEEE Trans. Electromagnetic Compatibility* **57**, 448 (2015).
- [2] Dario Fedeli, Gabriele Gradoni, Valter Mariani Primiani, and Franco Moglie, Accurate analysis of reverberation field penetration into an equipment-level enclosure, *IEEE Trans. Electromagnetic Compatibility* **51**, 170 (2009).
- [3] Kaya AÖ, Greenstein LJ, Trappe W. 2009 Characterizing indoor wireless channels via ray tracing combined with stochastic modeling. *IEEE Trans. Wireless Commun.* **8**, 4165–4175.
- [4] B. Dietz, T. Guhr, H. L. Harney, and A. Richter, *Strength Distributions and Symmetry Breaking in Coupled Microwave Billiards*, Phys. Rev. Lett. **96**, 254101 (2006).
- [5] JM Jin. *The finite element method in electromagnetics*. Hoboken, NJ: John Wiley & Sons, 2015.
- [6] A Taflove , SC Hagness. *Computational electrodynamics: the finite difference time-domain method*. Boston, MA: Artech House, 2005.
- [7] G Tanner , N Søndergaard. *Wave chaos in acoustics and elasticity*. J. Phys. A: Math. Theor. 40, R443–R509, 2007.
- [8] R Holland. *Statistical Electromagnetics*. CRC Press, 1st edition, 1999.
- [9] O Legrand, F Mortessagne. *Wave chaos for the Helmholtz equation*. Matthew Wright & Richard Weaver. New Directions in Linear Acoustics and Vibration, Cambridge University Press, pp. 24-41, 2010.
- [10] RH Lyon, RG DeJong. *Theory and application of statistical energy analysis*. 2nd edition, Boston, MA: Butterworth-Heinemann, 1995.
- [11] G Tanner. *Dynamical energy analysis—Determining wave energy distributions in vibro-acoustical structures in the high-frequency regime*. J. Sound Vib. **320**, 1023–1038, 2009.
- [12] AS Glasser. *An introduction to ray tracing*. New York, NY: Academic Press, 1989.
- [13] D Hill, M Ma, A Ondrejka, B Riddle, M Crawford, R Johnk. *Aperture excitation of electrically large, lossy cavities*. IEEE Trans. Electromagn. Compat. **36**, 169–178, 1994.

- [14] D Hill. *Plane wave integral representation for fields in reverberation chambers*. IEEE Trans. Electromagn. Compat. **40**, 209–217, 1998.
- [15] I Junqua, JP Parmantier, F Issac. *A network formulation of the power balance method for high-frequency coupling*. Electromagnetics **25**, 603–622, 2005.
- [16] Briggs G A 1992 *Acoustic Microscopy (Monographs on the Physics and Chemistry of Materials vol 47)* (New York: Oxford University Press)
- [17] Cervený V. 2001 *Seismic ray theory*. Cambridge, UK: Cambridge University Press.
- [18] McKown JW, Hamilton RL. 1991 *Ray tracing as a design tool for radio networks*. IEEE Netw. Mag. **5**, 27–30.
- [19] Bhaskar Chaudhury Shashank Chaturvedi. *Comparison of wave propagation studies in plasmas using three-dimensional finite difference time-domain and ray-tracing methods*. Physics of Plasmas. **13** (12): 123302
- [20] <https://www.ansys.com/products/electronics/ansys-hfss>
- [21] J Hart, T M Antonsen, E Ott, *Effect of short ray trajectories on the scattering statistics of wave chaotic systems*. Phys. Rev. E **80**, 041109, 2009.
- [22] J Yeh, J Hart, E Bradshaw, T M Antonsen, E Ott, S M Anlage. *Experimental examination of the effect of short ray trajectories in two-port wave-chaotic scattering systems*. Phys. Rev. E **82**, 041114, 2010.
- [23] X Zheng. *Statistics of impedance and scattering matrices in chaotic microwave cavities: The random coupling model*. PhD thesis, University of Maryland, College Park, 2005.
- [24] G Gradoni, J Yeh, B Xiao, T M Antonsen, S M Anlage, and E Ott. *Predicting the statistics of wave transport through chaotic cavities by the random coupling model: A review and recent progress*. Wave Motion, 51(4): 606-621, Innovations in Wave Modelling, 2014.
- [25] S Hemmady, T M Antonsen, E Ott, and S M Anlage. *Statistical prediction and measurement of induced voltages on components within complicated enclosures: A wave-chaotic approach*. IEEE Transactions on Electromagnetic Compatibility, 54(4): 758-771, 2012.
- [26] M L Mehta. *Random Matrices (Pure and applied mathematics, v. 142)*. Elsevier Science Limited, 2004.

- [27] Birkhoff, G.D. On the periodic motions of dynamical systems. *Acta Math.* **50**, 359–379 (1927).
- [28] Yun Z, Iskander MF. 2015 Ray tracing for radio propagation modeling: principles and applications. *IEEE Access* **3**, 1089–1100.
- [29] Hartmann T, Morita S, Tanner G, Chappell DJ. 2019 High-frequency structure-and air-borne sound transmission for a tractor model using dynamical energy analysis. *Wave Motion* **87**, 132–150. Innovations in Wave Modelling II.
- [30] Chappell DJ, Tanner G, Löchel D, Søndergaard N. 2013 Discrete flow mapping: transport of phase space densities on triangulated surfaces. *Proc. R. Soc. A* **469**, 20130153.
- [31] Bajars J, Chappell DJ, Søndergaard N, Tanner G. 2017 Transport of phase space densities through tetrahedral meshes using discrete flow mapping. *J. Comput. Phys.* **328**, 95–108.
- [32] Chappell DJ, Löchel D, Søndergaard N, Tanner G. 2014 Dynamical energy analysis on mesh grids - a new tool for describing the vibro-acoustic response of complex mechanical structures. *Wave Motion* **51**, 589–597.
- [33] Adnan F, Blakaj V, Phang S, Antonsen TM, Creagh SC, Gradoni G, Tanner G. 2021 Wireless power distributions in multi-cavity systems at high frequencies. *Proc. R. Soc. A* **477**: 20200228.
- [34] D. A. Hill, “Electromagnetic Fields in Cavities. Deterministic and Statistical Theories” John Wiley & Sons, Hoboken, New Jersey 2009
- [35] Paul G. Bremner; Gabriel Vazquez; Dawn H. Trout; Daniel J. Christiano. Canonical Statistical Model for Maximum Expected Immission of Wire Conductor in an Aperture Enclosure. 2016 IEEE International Symposium on Electromagnetic Compatibility (EMC)
- [36] Eugene P Wigner. On a class of analytic functions from the quantum theory of collisions. In The Collected Works of Eugene Paul Wigner, pages 409-440. Springer, 1993.
- [37] S Deus, P M Koch, and L Sirko. *Statistical properties of the eigenfrequency distribution of three-dimensional microwave cavities*. Phys. Rev. E, 52:1146-1155, Jul 1995.
- [38] E Ott. *Chaos in dynamical systems*. Cambridge university press, 2002.
- [39] Weyl, H. Über die Gleichverteilung von Zahlen mod. Eins. *Math. Ann.* **77**, 313–352 (1916).

- [40] S Hemmady. *A wave chaotic approach predicting and measuring electromagnetic field quantities of complicated enclosures*. PhD thesis, University of Maryland, College Park, 2006.
- [41] <https://www.mathworks.com/products/matlab.html>
- [42] J Yeh. *Wave chaotic experiments and models for complicated wave scattering systems*. PhD thesis, University of Maryland, College Park, 2013.
- [43] Gutzwiller M.C. (1990) Chaos in Classical and Quantum Mechanics. Interdisciplinary Applied Mathematics, vol 1. Springer, New York, NY
- [44] Stockmann, *Quantum Chaos*, Cambridge University Press, 1999.
- [45] K. Richter and M. Sieber, 'Semiclassical theory of chaotic quantum transport,' *Phys. Rev. Lett.*, vol. 89, pp. 206801, 2002.
- [46] X. Zheng, T. M. Antonsen, and E. Ott, "Statistics of impedance and scattering matrices in chaotic microwave cavities: Single channel case," *Electromagnetics*, vol. 26, pp. 3, 2006.
- [47] X. Zheng, T. M. Antonsen, and E. Ott, "Statistics of impedance and scattering matrices of chaotic microwave cavities with multiple ports," *Electromagnetics*, vol. 26, pp. 37, 2006.
- [48] X. Zheng, S. Hemmady, T. M. Antonsen, S. M. Anlage, and E. Ott, "Characterization of fluctuations of impedance and scattering matrices in wave chaotic scattering," *Phys. Rev. E*, vol. 73, pp. 046208, 2006.
- [49] S. Muller, S. Heusler, P. Braun, and F. Haake, 'Semiclassical approach to chaotic quantum transport,' *New J. Phys.*, vol. 9, pp. 12, 2007.
- [50] T. Kottos and U. Smilansky, 'Quantum graphs: a simple model for chaotic scattering,' *J. Phys. A: Math. Gen.*, vol. 36, pp. 3501, 2003.
- [51] E. Ott, 'Instability condition for confined waves with ergodic ray trajectories' *Phys. Fluids* 22, 2246 (1979).
- [52] M. V. Berry, 'Chaotic Behavior of Deterministic Systems'. Les Houches Summer School 1981 (North-Holland, 1983).
- [53] S.W. McDonald and A. N. Kaufman, "Spectrum and eigenfunctions for a hamiltonian with stochastic trajectories," *Phys. Rev. Lett.*, vol. 42, no. 18, pp. 1189–1191, Apr. 1979



